Fabrication of nanostructured free-standing Fresnel zone plate for neutral matter-waves microscopy

Kanthee Kosolyuthasarn

Master Thesis in Physics:
Measurement Technology and Nanophysics

Department of Physics and Technology

University of Bergen

June 2022

Abstract

Nanofabrication contributes to almost every field of science, and its essentialness in technology can hardly be overstated. Electron beam lithography (EBL) is one of the most important and widespread methods for achieving high-density and high-resolution structures. However, the resolution, density, and aspect ratio of the fabricated nanostructure are often limited by the lithography method, and the pattern transfer to the underlying substrate.

The nanophysics group at the University of Bergen (UiB) has a long experience with EBL and fabrication of free-standing structures on thin membranes. However, it has been a longstanding challenge to determine the optimal patterning conditions for the complex free-standing Fresnel zone plate, a circular diffraction grating focusing element consisting of zones with decreasing widths for increasing radii, the optical element for focusing neutral helium atoms.

This thesis presents the optimized fabrication method, using a 30 kV EBL-system, to obtain a high-quality free-standing zone plate structure in a Si_3N_4 membrane. The fabrication is a two-step procedure based on the exposure of support bar structure for holding the zones of the zone plate in place, followed by the exposure of the zone plate pattern using an advanced multilayer etch mask. To achieve the best possible fabrication results, a significant amount of work has been to optimize the parameters for EBL and the pattern transfer, in addition to pattern design of the zone plate with a particular focus on the EBL exposure dose profile.

Several free-standing Fresnel zone plates were fabricated using the optimized fabrication parameters in this thesis work, with design parameters fitting for a liquid nitrogen cooled helium beam in the neutral helium microscope NEMI ($\lambda = 0.0978$ nm). The zone plates had an outermost zone width of 92 nm and an overall diameter of 192 um. The processes demonstrate fully etched open zones with fabricated dimensions very close to the designed dimensions. From experience in the UiB Nanophysics research group, based on the SEM investigations of the fabricated zone plates, it is expected that the fabricated zone plates will perform as predicted. This thesis work opens doors for the more routinely fabrication of Fresnel zone plates for the neutral helium atomic beam microscope and also nanofabrication of other dense free-standing structures.

Acknowledgements

I would like first to thank everyone who has helped and contributed to this thesis becoming a reality.

First and most importantly, I would like to express my gratitude to my supervisor, Dr. Martin Møller Greve. Thank you for all guidance, constructive feedback, and last but not least, all the hours of fixing the instrument issues at the lab. Thank you for all the discussions and motivation.

A special thanks go to Prof. Bodil Holst, Dr. Ranveig Flatabø, and Espen Werdal Selfors (Ph.D. candidate at the UiB nanophysics group) for all the discussions, guidance, feedback, and help I received when I faced the problems.

My master's students fellows deserve a special acknowledgment for being such good friends. Thank you for the good times and many interesting conversations at the IFT cafeteria.

Thank you to Ida Pernille Løvås, my love, best friend, and great office partner. Thank you for all the motivation you gave me and for being so supportive in every possible moment. Last but not least, I want to thank my family, especially my sister, mother, and grandmothers. Thank you for all the dinners, support, and the love you have given me.

Contents

List of Figures

List of Tables

Chapter 1

Introduction

This chapter gives an introduction to matter-wave optics and nanofabrication, followed by the motivation and the objectives of the thesis. The chapter ends with a section outlining the contents of the rest of this thesis.

1.1 Matter-wave optics

The wave-particle duality work of Louis de Broglie in 1924 is considered to be one of the most groundbreaking works within the field of physics. De Broglie stated that every quantum entity or particle can behave as a wave [1]. The discovery is essential for the works in the field of matter-wave optics, and the last decade has witnessed many spectacular scientific and technological advances [2, 3, 4, 5].

The importance of microscopy in the modern world is difficult to be overstated. Today, matter-wave microscopy is a multifaceted, interdisciplinary field that enables scientists to image, investigate and manipulate particles at nano-scale [6, 7, 8, 9]. The technology of using massive particles such as helium (He) ions as the imaging probe has developed rapidly over the last decade [6, 10]. The matter-wave microscope: NEutral Helium Atom MIcroscopy (NEMI) is one of the main ongoing projects of the University of Bergen (UiB) nanophysics group [11, 12, 13, 14, 15]. Using ground state neutral helium atom as the imaging probe has its advantages as the He atom has low energy (< 0.1 eV) and is neutral [11]. Consequently, NEMI is particularly suited for microscopy of fragile and insulating samples.

One of the main challenges with an atom microscope is the focusing element. NEMI uses neutral helium with very low energy ($<$0.1 eV compared to $>$1 keV for an electron microscope), so the beam cannot penetrate any solid material. Ground state helium is furthermore inert, has low polarizability, and has no permanent magnetic moment, so it cannot be manipulated by an electromagnetic field [16]. That being said, the

helium beam can be focused in a number of ways. Previously, an aperture has been used for collimating neutral molecules [17], but was limited by the achievable intensity and resolution of the focused beam. Alternatively, mirror focusing has been studied and applied [18, 19, 20, 21]. One advantage of mirror focusing is the possibility of large numerical aperture, thus, high intensity beams. Secondly, the absence of the chromatic aberration, which is an important consideration due to the difficulty of achieving a monochromatic helium beam [22]. However, the achievable focus resolution is essentially limited by spherical aberration, and up till now, it has been challenging to control the curvature of the mirror with high enough precision to get a highly focused beam [21].

Another approach is to use a nanostructured optical element that utilizes diffraction to manipulate and focus the neutral helium beam. A Fresnel zone plate consists of circular rings that alternate between being transparent and opaque, and the width of the rings decreases with the distance from the center. The UiB nanophysics group has the only microscope worldwide that uses a Fresnel zone plate to focus the helium beam and has, over the years, published a significant amount of work on atom focusing see e.g., [11, 15, 23, 24]. So far, a Fresnel zone plate is considered to be the most promising option to manipulate neutral helium beam as the group has managed to focus the helium beam under 1 μm [11] and the fact that a Fresnel zone plate can be inserted directly into the beam line [23]. The problem with zone plates is that they suffer from chromatic aberration, and only one diffraction order, usually the first order, is used for imaging, limiting the beam's intensity. Thirdly, the limiting resolution of a zone plate is defined by the width of the outermost zone. Currently, NEMI uses a zone plate with an outermost zone width of 48 nm [25].

1.2 Nanolithography

In nanolithography, a pattern is written in a serial fashion on a substrate or transferred through a mask on a substrate. For structures with dimensions down to 500 nm, typically standard photolithography techniques are often used [26]. To achieve high resolution and complex structure like, for instance, a zone plate, electron beam lithography (EBL) is often used as a tool for structure exposure and followed by a series of patterning transferring steps. However, the dimension of the structure and high-quality patterning results are usually limited by, e.g., electron beam energy, substrate materials, and subsequent processes. To realize nanostructure using EBL, an electron sensitive resist such poly-methyl-meth-acrylate (PMMA), Hydrogen silsesquioxane (HSQ), and ZEP 520A is used as the pattern transferring agents. The previous EBL work in the UiB nanophysics group has successfully achieved complex

free-standing structures like zone plate [24], Atomic sieve [27] and photonic crystals [28].

1.3 Thesis objectives

At present, the UiB nanophysics group is part of a large lithography project, *NanoLace* (more information, see [29]), which one of the main motivations behind the work in this thesis namely to demonstrate nanofabrication of free-standing nanoscale structures.

The objectives have been to fabricate a free-standing Fresnel zone plate, ensure that the fabrication steps are reproducible, and establish the fabrication procedure. This include:

- To design the Fresnel zone plate and support bar structure suitable for NEMI's characterization parameters.
- To establish methods as well as investigate and optimize the working parameters for free-standing Fresnel zone plate fabrication based on [24]
- To fabricate a free-standing Fresnel zone plate for NEMI with the optimized parameters.

1.4 Thesis outline

Chapter 2 introduces the classical theory behind diffraction, Fresnel zone plate construction, and equations. Chapter 3 presents the main equipment used extensively for the works in this thesis, while chapter 4 explains the characterization and investigation techniques. Chapter 5 outlines the methods and critical approaches for the free-standing Fresnel zone plate fabrication. The results of the investigation of the parameters, as well as the free-standing Fresnel zone plate fabrication, are presented in chapter 6. The thesis finishes with a conclusion and suggestions for future work in chapter 7.

Chapter 2

Theory

As mentioned in section (1.1), the Fresnel zone plate is quite popular when it comes to focusing of neutral helium beam, and it is the technique of choice that this thesis is established on. This chapter explains the principle of Huygens-Fresnel, which is the starting point for diffraction. Finally, the chapter introduces the theory behind Fresnel zone plate design in addition to its properties.

2.1 Diffraction theory

The term diffraction is essential in microscopy and optics. Diffraction explains the variation in the propagation path of waves when they encounter an aperture or an obstacle.

2.1.1 Huygens-Fresnel principle

The *Huygens-Fresnel* principle can be used to describe the concept of diffraction. According to Huygens's construction, all points on an unobstructed part of a wavefront can be considered as a center of a secondary source of spherical wavelets. Fresnel was able to account for diffraction by supplementing Huygens's construction with the superposition of the secondary wavelets. A disturbance will occur from the interference of the individual constituent waves, resulting further in the characteristic bending pattern. This combination formed the so-called Huygens-Fresnel principle, and it can be visualized in fig. (2.1). [30]

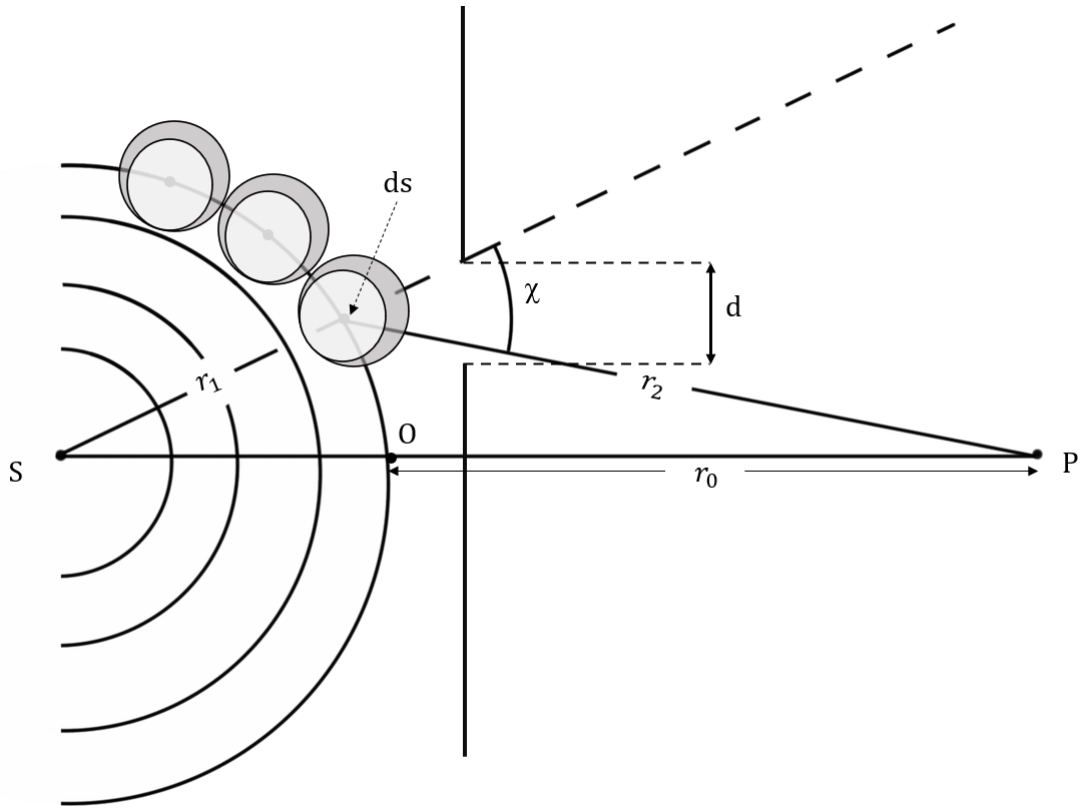

Figure 2.1: Illustration of geometric arrangement for Fresnel calculation. S is a point source producing the primary spherical wave while dS is the element of the primary wavefront. Figure also illustrates that every point on the wavefront can be considered as a source of spherical wavelets, but the amplitude of the secondary wavelets drops as the angle of deviation from the direction of the primary wavelets (indicating with grey area in figure). The part of the wave that is not obstructed by the aperture d contributes to the disturbance at point P. The figure is taken inspiration from [31].

The disturbance at a point on a spherical wavefront can be represented using wave equation $Ae^{\frac{ikr_1}{r_1}}$ where k is the wave vector. A describes the amplitude of the spherical wavelet at point S. Refer to the Huygens-Fresnel principle, the disturbance contribution $dU(P)$ due to the element dS at a point P is expressed by [24, 30]:

$$dU(P) = K(\chi) \cdot \frac{Ae^{ikr_1}}{r_1} \frac{e^{ikr_2}}{r_2} dS \tag{2.1}$$

where r_1 is the distance from the source point S to the wavefront, and r_2 is the distance from that wavefront to the observation point P, see fig. (2.1). $K(\chi)$ is an inclination factor describing that the amplitude of the secondary wave depends on its propagation direction. In this case, the variable χ is the angle between the normal of the primary wavefront and the normal of the secondary wavefront, as illustrated in

fig. (2.1). Kirchhoff was able to provide an actual expression for $K(\chi)$, which turns out to be [31]:

$$K(\chi) = \frac{1}{2\lambda}(1 + cos(\chi)) \tag{2.2}$$

From eq. (2.2), $K(\chi)$ has maximum value in the original propagation direction ($\chi = 0$), and it decreases rapidly when χ is increasing toward $\frac{\pi}{2}$. It represents the fact that the secondary spherical wavelets do not propagate in the reverse direction.

Moreover, Fresnel assumed that only the part of dS that is not obstructed by obstacles contributes to the disturbance at point P. Hence the total disturbance at point P can be determined by integrating over the surface area of S, resulting to eq. (2.3) known as Fresnel diffraction integral. [30]

$$U(P) = \frac{Ae^{ik_1}}{r_1} \iint_S \frac{e^{ikr_2}}{r_2} K(\chi) dS \tag{2.3}$$

2.2 Fresnel zone plate

2.2.1 The structure of Fresnel zone plate

For the construction of Fresnel zone, consider a system similar to the one in fig. (2.1), dividing the spherical wavefront from point S into annular regions with a period of $\frac{\lambda}{2}$ where λ is the wavelength of wavefront, see fig. (2.2). Using this as the starting point, *Fresnel* or *half-period* zones can be defined. The Fresnel zones alternately contribute to constructive or destructive interference at point P. By blocking the zones alternately, maximum constructive interference can be achieved. This will be explained in more detail in the following sections. [30]

The area of the wavefront between r_0 and $r_0 + \frac{\lambda}{2}$ from the focal point P is defined as the first zone to P. The second zone, will be between $r_0 + \frac{\lambda}{2}$ and $r_0 + \lambda$ and so on. By continuing in this manner, the mathematical description of the m^{th} zone becomes: [31]

$$r_0 + \frac{(m-1)\lambda}{2} < m^{th}\text{Fresnel zone} < r_0 + \frac{m\lambda}{2} \tag{2.4}$$

In this case, m is a positive integer from 1 to M, where M is the total number of zones.

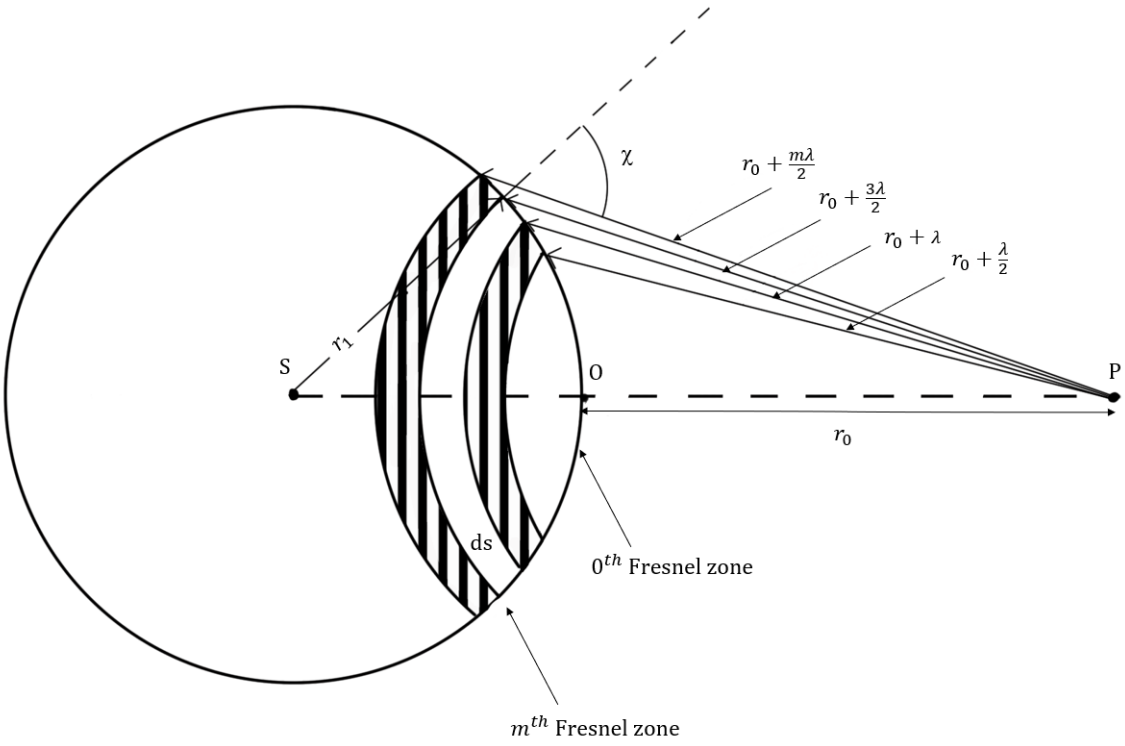

Figure 2.2: Propagation of a spherical wavefront. The wavefront is divided into section with a period of $\frac{\lambda}{2}$, referring to as Fresnel zone. The stripped Fresnel zones are corresponding to odd-numbered zones, and the opposite are even-numbered. The figure is taken inspiration from [31].

The disturbance contribution of the m^{th} zone to *U(P)* can be formulated by integrating eq. (2.1) over a Fresnel zone and using the expression of area element *dS*, which is given by [30]:

$$dS = r_1^2 sin(\theta) d\theta d\phi = \frac{r_1}{r_1 + r_0} r_2 dr_2 d\phi \tag{2.5}$$

where r_0 and r_1 are the distances showed in fig. (2.2). r_2 is the propagation path of the wave from m^{th} zone to point *P*. θ and ϕ in this case are referring to angles in spherical coordinate system i.e. polar angle and azimuthal angle, respectively, see fig. (2.3).

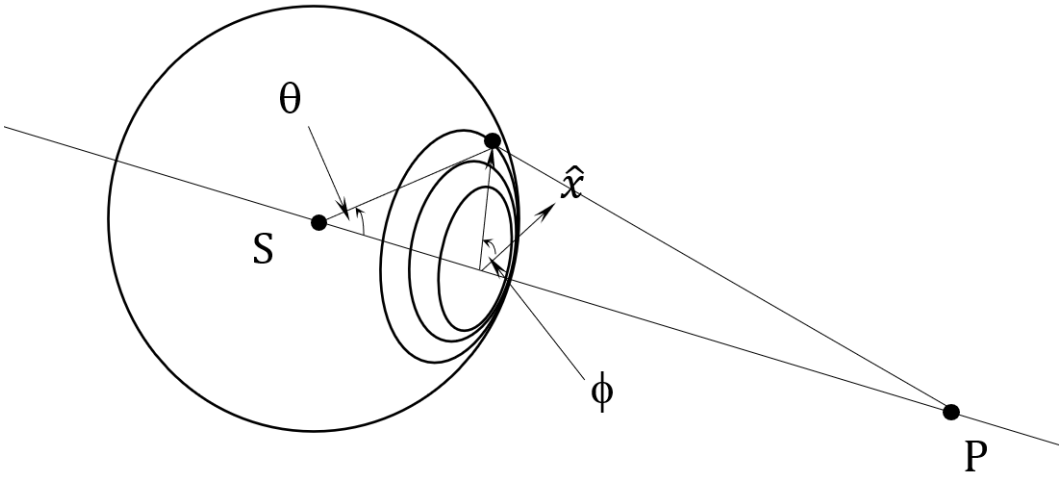

Figure 2.3: Figure illustrates the angles in eq. (2.5).

The disturbance contribution of the m^{th} zone, $U_m(P)$, is then given by [30]:

$$U_m(P) = 2i\lambda(-1)^{m+1}K_m\frac{Ae^{ik(r_1+r_0)}}{r_1+r_0} \tag{2.6}$$

where K_m is the inclination factor of the $m^{th}zone$. From eq. (2.6), whether the disturbance at point P is contributed positively or negatively depends on whether the zone is numbered even or odd. For the odd-numbered zone, the disturbance will contribute with constructive inference at point P, and the opposite for even-numbered zones. The total disturbance at P for a Fresnel zone with M zones is obtained by summing all the contributions:

$$U(P) = 2i\lambda\frac{Ae^{ik(r_1+r_0)}}{r_1+r_0}\sum_{m=1}^{M}(-1)^{m+1}K_m \tag{2.7}$$

In principle, due to the inclination factor K_m, the successive contributions do not completely cancel each other since K_m decrease with increasing m. However, the value of inclination factor is varied from 0 to 1, and over a great many zones, the variation of the contribution between adjacent zones can be neglected [31]. As a result, the total disturbance at point P from all m zones depending on whether $m = odd$ or $m = even$ can be approximated as shown in eq. (2.8) and (2.9) [31].

$$U(P) \approx \frac{U_1(P)}{2} + \frac{U_m(P)}{2} \qquad \text{for m = odd} \tag{2.8}$$

$$U(P) \approx \frac{U_1(P)}{2} - \frac{U_m(P)}{2} \qquad \text{for m = even} \tag{2.9}$$

where $U_1(P)$ is the disturbance contribution from the first zone. Moreover, the spherical wave illustrated in fig. (2.2) is divided into a finite number of zone. The last or the m^{th} zone will be located at $\chi = \pi$, consequently, $U_m(P)$ is equal to zero. The result gives the total disturbance at point P to be approximately:

$$U(P) \approx \frac{U_1(P)}{2} \tag{2.10}$$

As can be seen in eq. (2.10), the disturbance generated by the entire unobstructed wavefront is approximately equal to one-half of the contribution from the first zone.

A way to visualize the disturbance contribution from each zone is by using a so-called vibration curve (fig. (2.4)), a graphic method for qualitatively analyzing the contribution that arises predominantly from circularly symmetric configurations. As illustrated in fig. (2.4 a), a Fresnel zone can be divided into N subzones by intersection of spheres. The phase difference of the first zone is equal to π rad (corresponding to $\frac{\lambda}{2}$), hence, each subzone has a phase shift of $\frac{\pi}{N}$ rad. The vectors in fig. (2.4 a) represent the amplitude of the contribution and the phase of each subzone, known as *phasor*. The phasors correspond to the solution of eq. (2.3), hence the disturbance of the first Fresnel zone at observation point P is the sum of the phasors, which is not surprising, just U_1. [31]

Consider more than one Fresnel zone where each zone is divided into an infinite number of subzones. Integrating over the subzones results in a smooth vibration curve, as shown in fig. (2.4 b). The figure shows the contribution of disturbance from every Fresnel zones. The even-numbered zones are specified with strip lines, and it can be seen that contributions from these zones are negative. As a consequence, the reduction of the disturbance at point P occurs. The total disturbance at point P is given by the phasor from the starting point to the center of the vibration curve, equal to $U_1/2$ as shown in eq. (2.10). In order to obtain the highest possible amplitude of the disturbance at point P, the destructively interfering zones are blocked. The total disturbance for the first three transparent zones can be visualized as shown in fig. (2.4 c).

Note that the amplitude of the disturbance from each Fresnel zone gradually decreases, and hence the vibration curve has a spiral form. This is a result of the inclination factor K_m in eq. (2.7).

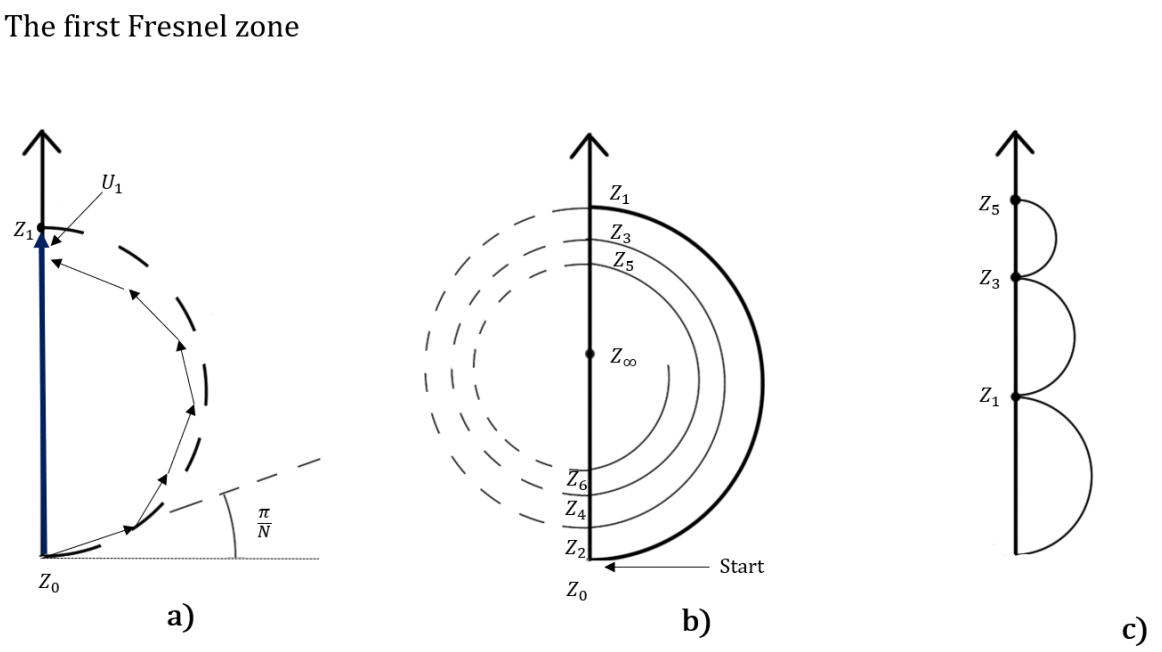

Figure 2.4: Vibration curves: a graphic representation of the disturbance contribution at an observation point. a) the first Fresnel zone is divided into N subzones with a phase shift of $\frac{\pi}{N}$. The phasors represent the amplitude of the disturbance contribution at an observation point. Note that the phasor chain deviates slightly from the circle due to the inclination factor. b) shows a smooth vibration curve of Fresnel zones as a result of integrating the subzones. Each zone is separated by a half-turn, and even-numbered zones are indicated with strip lines, representing destructive disturbance contribution. The contribution from each zone is decreasing due to the inclination factor. c) represents a scenario when the even zones are blocked. The vertical axis represents the amount of the disturbance contribution at the observation point.

2.2.2 Construction of a Fresnel zone plate

In order to achieve the highest possible disturbance at point P, a Fresnel zone plate that allows transmission only for positive interference is needed. This means that the even-numbered zones are blocked. The total disturbance at point P is then the sum of odd-numbered zones contribution as described earlier in fig. (2.4 c). Fig. (2.5) shows a possible way a Fresnel zone plate could look. r_M is the radius of the zone plate, while r_m is the radius to the m^{th} zone. Consider a wave from the source point S that travels through the zone plate. The direct beam will have a path S-O-P which corresponding to distance $a_0 + b_0$, where a_0 and b_0 are the distance from S to zone plate center O and the distance from O to a point P respectively.

A wave from point S will also travel through the zones that allow for transmission and have a path S-C_m-P, where C_m is the point within the m^{th} zone. The travelling distance will be equal to $a_m + b_m$, where a_m is distance the path S-C_m while b_m is from C_m to P. The difference in phase from between S-O-P and S-C_m-P will be equal to $\frac{m\lambda}{2}$ when arriving at point P due to the way the zone plate is constructed.

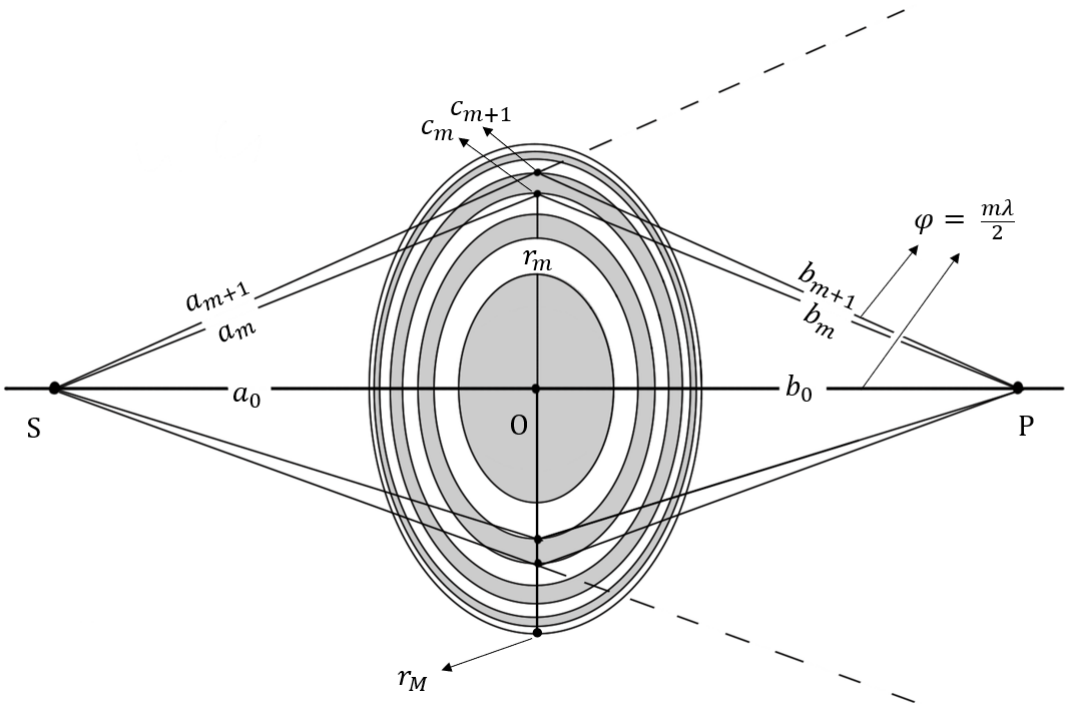

Figure 2.5: Shows a possibly zone plate geometry. The 0^{th} and the even-numbered zones are opaque representing with grey zones. The odd-numbered zones are transparent shown as the white zones.

2.2.3 Fresnel zone plate calculation

By using the knowledge of the value of phase difference and simple geometric interpretation, it is possible to derive the equation for the outermost radius of the Fresnel zone plate r_M. For the case of pathlength S-O-P and S-C_m-P, the phase difference can be formulated as:

$$(a_m + b_m) - (a_0 + b_0) = \frac{m\lambda}{2} \tag{2.11}$$

Using direct beam path and Pythagoras theorem, the distance $a_m + b_m$ can be reformulated in term of the outer radius of the mth Fresnel zone r_m^2:

$$a_m + b_m = \sqrt{a_0^2 + r_m^2} + \sqrt{b_0^2 + r_m^2} \tag{2.12}$$

Applying binomial series theorem to eq. (2.12) in addition to the assumption that r_n is considerable smaller than a_0 and b_0. The equation become:

$$a_m + b_m = a_0 + b_0 + \frac{r_m^2}{2b_0} + \frac{r_m^2}{2a_0} \tag{2.13}$$

Substituting eq. (2.13) into eq. (2.11) and solve for the outer radius of the mth Fresnel zone r_m^2:

$$r_m^2 = \frac{m\lambda a_0 b_0}{(a_0 + b_0)} \tag{2.14}$$

For a zone plate with M total zones, the equation for the outermost radius of the Fresnel zone plate r_M becomes:

$$r_M^2 = \frac{M\lambda a_0 b_0}{(a_0 + b_0)} \tag{2.15}$$

The equation shows the implicit relationship between the structure and the focal plane of the Fresnel zone plate and the frequency of the wave. The only variable in eq. (2.15) is the total number of zones M, which has important implications on the zone plate focusing properties, including efficiency and resolution, more detail will be provided in the next sections.

Additionally, it is possible to calculate the width of the m^{th} zone, dr_m of a zone plate by assuming that the width for transparent and the adjacent opaque zone is approximately equal. Differentiating eq. (2.14) with respect to m, dr_m can be calculated as following: [32]

$$\frac{dr_m}{dm} = \frac{d}{dm}\left(\sqrt{\frac{m\lambda a_0 b_0}{(a_0 + b_0)}}\right) = \frac{\lambda\frac{a_0 b_0}{(a_0+b_0)}}{2\sqrt{\frac{m\lambda a_0 b_0}{(a_0+b_0)}}} \tag{2.16}$$

Using that $\lambda\frac{a_0 b_0}{(a_0+b_0)} = \frac{r_m^2}{n}$ and $r_m = \sqrt{\frac{m\lambda a_0 b_0}{(a_0+b_0)}}$, eq. (2.16) can be reformulated as:

$$dr_m = \frac{\lambda a_0 b_0}{2r_m(a_0 + b_0)} \tag{2.17}$$

Thus, the width if the outermost zone dr_M is:

$$dr_M = \frac{\lambda a_0 b_0}{2r_M(a_0 + b_0)} \tag{2.18}$$

2.2.4 Focusing properties of Fresnel zone plate

For a Fresnel zone plate with total number of zones M, and if M larger than 100 [33], the zone plate focus properties can be described in analogy to that of a thin lens [34]. The thin lens theorem together with eq. (2.14), the focal length of the zone plate f is then given by:

$$\frac{1}{f} = \frac{1}{a_0} + \frac{1}{b_0} = \frac{m\lambda}{r_m^2} \tag{2.19}$$

a_0 and b_0 are the distance from source point S to the observation point P through the zone plate center O, see fig. (2.5). Solve explicitly for the focal length f, eq. (2.19) gives:

$$f = \frac{r_m^2}{m\lambda} \tag{2.20}$$

For zone plate with total zones number M, the equation becomes:

$$f = \frac{r_M^2}{M\lambda} \tag{2.21}$$

It can be seen that the equation of the focal length strongly depends on the wavelength of the inbound wave. Consequently, the focus properties of the Fresnel zone plate will be afflicted by chromatic aberration. This aberration arises due to different wavelengths having slightly different focal lengths.

Moreover, the factor that describes how the image's dimension has changed compared to the object can be determined. This is a so-called magnification factor of the zone plate which is given by: [35]

$$\text{Magnification} = \frac{b_0}{a_0} \tag{2.22}$$

2.2.5 Diffraction order

Similar to other linear diffraction gratings, a Fresnel zone plate produces many focal spots in addition to the first order. According to [24] the formulation of the n^{th} diffraction order focal length f_n is giving by:

$$f_n = \frac{nr_M^2}{M\lambda} \tag{2.23}$$

where n is the diffraction order and can either be positive or negative. Positive diffraction orders correspond to real focal points, while the negative orders will have virtual focal points [31]. This is illustrates in fig. (2.6). Note that when n is an even number, the diffracted beam paths in the figure are presented as strip lines. This indicates that the beams are destructive interference, and thus no disturbance will be observed. For $n = 0$ is a special case when the incoming beam passes through the zone plate without any interaction. The 0^{th} order provides substantially more intensity than other diffraction orders and will thus have a negative effect on the image through reducing image contrast [15, 24].

For this reason zone plates are often constructed so that the inner-most zones are opaque. This method will improve the contrast in the system since the contribution 0^{th} order is blocked. In addition, a so-called order sorting aperture (OSA) can be used behind the zone plate beam path to completely exclude the contribution from 0^{th} order and negative diffraction orders. However, suppose the size of the blocked central zone is too large. In that case, it will reduce the zone plate diffraction efficiency and, in addition, increases chromatic aberration. [24] The mentioned system is also included in the helium microscope (NEMI) that this thesis is attempting to fabricate a zone plate for.

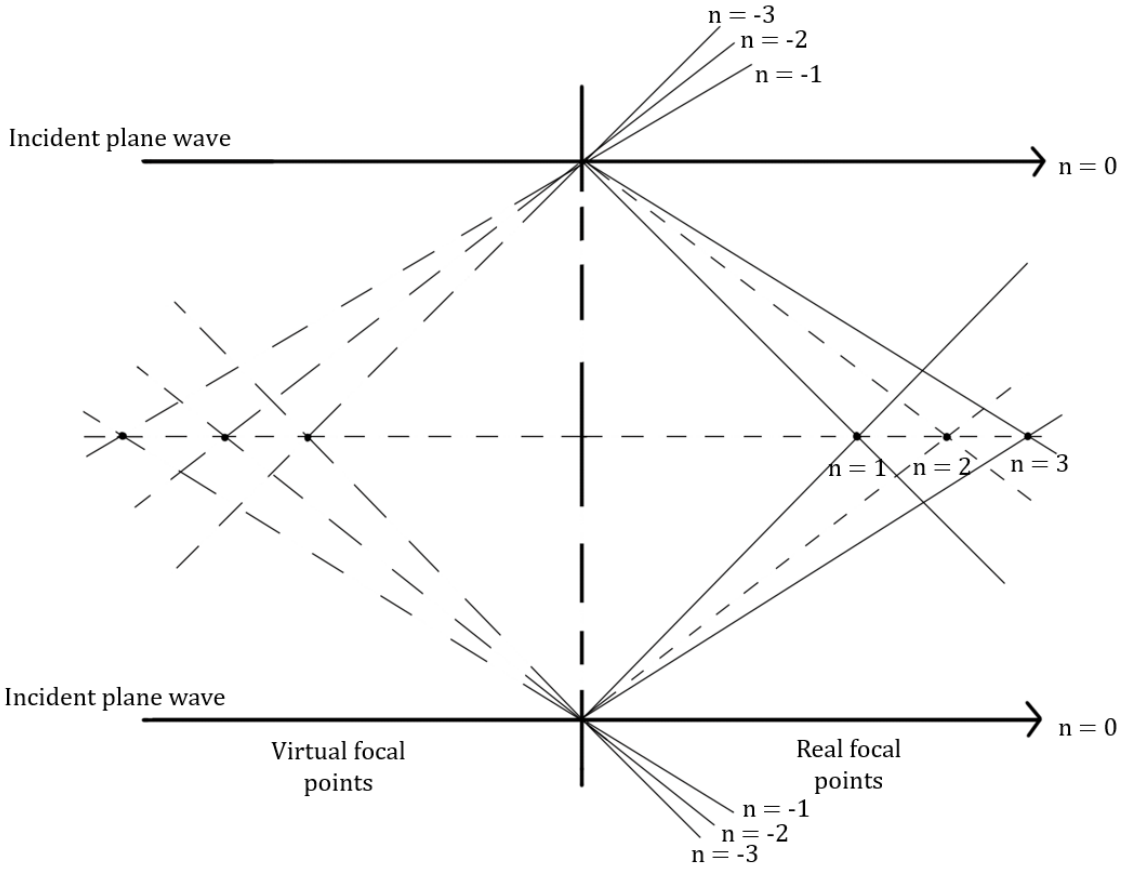

Figure 2.6: The figure illustrates many diffraction orders producing by a zone plate. The even number diffraction are presented as strip line indicating destructively inference. The 0^{th} order is indicated with a straight line as the beam is passing through the zone plate without any interaction.

Eq. (2.24) shows the differentiated formulation of the eq. (2.23). It can be seen that higher diffraction orders suffer less from chromatic aberration since the change in focal length decrease with an increasing n. However, the higher diffraction orders provide less intensity and therefore are not suited for use as an imaging focus. This is discussed in more details in section (2.2.7).

$$\frac{\delta f_n}{\delta \lambda} = -\frac{r_M^2}{nM\lambda^2} \tag{2.24}$$

2.2.6 Resolution of Fresnel zone plate

In accordance with the theory, the minimal achievable focus width, w, of an atomic beam using a Fresnel zone plate is defined by de Broglie wavelength of the atomic beam λ. The term focus width describes the dimension of the focus spot size. This corresponds to the term *spatial resolution* which is the smallest resolvable distance between two objects. By definition, it describes the ability of an image-forming device

to distinguish the minor details of the imaged object. One of the most standard methods to estimate the spatial resolution δ is by using the Rayleigh criterion, which for a zone plate is given by: [30, 32]

$$\delta = \frac{0.61\lambda}{NA} \tag{2.25}$$

where NA is numerical aperture. In this case, NA is a dimensionless number that describes the maximum angle of the wave entering or leaving the zone plate, and given by:

$$NA = sin(\theta) = \frac{D/2}{f} \tag{2.26}$$

θ is the angle of the incoming (or exiting) wave relative to the optical axis. f is the zone plate focal length, and D corresponds to the zone plate diameter (i.e., given by $D = 2r_M$). Thus, eq. (2.25) can be reformulated as:

$$\delta = 1.22\frac{\lambda f}{2r_M} \tag{2.27}$$

For a given focal length f and wavelength λ, to obtain the best possible resolution meaning to increase the zone plate diameter D, and thus, increasing the number of zones for the zone plate. It is useful to relate the resolution of the zone plate δ_{ZP} to the number of zones M and the width of the outermost zone dr_M. Rewrite eq. (2.18) with thin-lens formula and insert it in eq. (2.27), the smallest resolvable distance of a Fresnel zone plate (δ_{ZP}) is proportional to the width of the outermost zone dr_M as shown in eq. (2.28).

$$\delta_{ZP} = 1.22dr_M \tag{2.28}$$

The limitation of the theoretical resolution value depends on the Fresnel zone plate fabrication, which is how narrow the outermost zones can be fabricated. The smallest zone width is the M^{th} zone, and it tends to be the most challenging zone to fabricate using lithography [12].

However, the Rayleigh limit mentioned above might not be a realistic assessment of the practical resolution. In practice, several factors set a limit to what the smallest focus width can be achieved. There is a velocity distribution of the atom in the atomic beam, which also results in wavelength distribution. Fig. (2.7) illustrates the *point*

spread function (PSF) due to chromatic aberration for a Fresnel zone plate. The point spread function generally describes the normalized intensity distribution of the point-source image. w in figure (2.7) referring to the smallest achievable focus spot size (limited by PSF) and can be determined from the figure by using geometry identities. As a result, w is given by: [23]

$$w = \frac{r_M}{\frac{\lambda}{\Delta\lambda}} \tag{2.29}$$

where $\frac{\lambda}{\Delta\lambda}$ is the ratio between the wavelength and the full-width at half-maximum (FWHM) of the wavelength distribution.

As mentioned, the spread of the beam velocity can arise from the fact that the atomic beams do not have exactly the same energy. The value of the velocity spread can be measured in terms of *speed ratio* S and is given by:

$$S = 2 \cdot \sqrt{ln(2)} \cdot \frac{v}{\Delta v} \simeq 2 \cdot \sqrt{ln(2)} \cdot \frac{\lambda}{\Delta\lambda} \tag{2.30}$$

Here, v and Δv are mean velocity and the FWHM of the velocity distribution. The approximately equal term in eq. (2.30) arises from the fact that the relation between wavelength λ and velocity v is linear. Eq. (2.29) together with (2.30) forms the following formulation of focus spot size:

$$w = 2 \cdot \sqrt{ln(2)} \cdot \frac{r_M}{S} \tag{2.31}$$

It can be seen from eq. (2.31) that in practice, the achievable focus spot size depends on the velocity distribution of the beam and, again, the geometry of the zone plate. One possible method to obtain a narrow focus spot size is to decrease r_M, which can be done by fabricating a smaller zone plate. Distinctly the other factor is to increase the speed ratio S. This can be achieved by cooling the beam source nozzle, increasing source pressure, or selecting velocity. Unfortunately, all the methods mentioned above can naturally also entail a counterproductive reduction in the intensity of the diffraction point. [15, 23]

It is also worth to mention the relation ship between the number of zones M and the focus spot size w. Solve eq. (2.31) for the outermost radius r_M and insert it in the eq. (2.21). The relationship between these two variables can be obtained:

$$r_M = \frac{w \cdot S}{2\sqrt{ln(2)}} \tag{2.32}$$

This relation shows that the number of zones M is directly proportional to the zone plate resolution. Thus, doubling the zone plate resolution while preserving the system's speed ratio S requires doubling the number of zones.

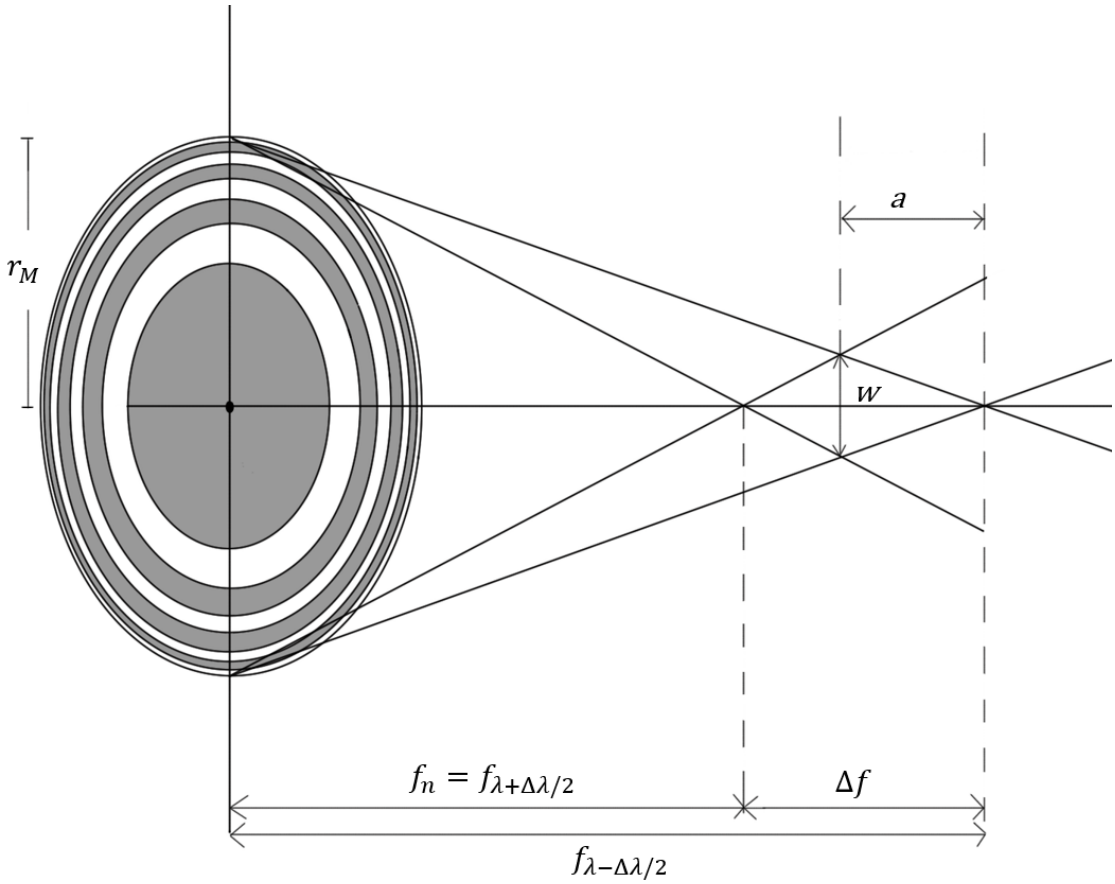

Figure 2.7: Figure illustrate point spread function due to chromatic aberration for a Fresnel zone plate. Figure is taken and modified from [23].

2.2.7 Focusing efficiency

How well a Fresnel zone plate is able to focus the incident atomic beam can be described by the term *focusing efficiency*, η. By definition, the focusing efficiency for the n^{th} diffraction order is defined as the fraction of the incident beam that is focused by the lens in the order of interest [15, 36]. According to [24], the mathematical formulation of the zone plate efficiency for the n^{th} order η_n is given by:

$$\eta_n = \left(\frac{sin([\frac{a}{d}]n\pi)}{n\pi} \right)^2 \tag{2.33}$$

where n is, as mentioned, the order of diffraction which can be either positive or negative value. a and d are the width of a transparent zone, and the width of a zone pair respectively. The ratio $\frac{a}{d}$ is often referred to as the *open-ratio* of the zone plate. From eq. (2.33), the focusing efficiency is maximized when the value of the open-ratio is equal to 0.5. This is for the case when the zone plate is designed for use with the first diffraction order. Applying L-Hopitals theorem on eq. (2.33), the focusing efficiency of the 0^{th} order can be estimated as follows:

$$\lim_{n\to 0} \eta_n = \left(\frac{sin([\frac{1}{2}]n\pi)}{n\pi} \right)^2 \tag{2.34}$$

L-Hopitals theorem:

$$\lim_{n\to 0} \eta_{n=0} = \left(\frac{\frac{d}{dn}[sin([\frac{1}{2}]n\pi)]}{\frac{d}{dn}[n\pi]} \right)^2 \tag{2.35}$$

$$= \lim_{n\to 0} \eta_{n=0} = \left(\frac{\frac{\pi}{2} \cdot cos(\frac{\pi}{2}n)}{\pi} \right)^2 \tag{2.36}$$

Investigate when n approaching 0:

$$\lim_{n\to 0} \eta_{n=0} = \left(\frac{1}{2} \right)^2 \tag{2.37}$$

For the case of open-ratio equal to 0.5, the focusing efficiency of the beam passing through the zone plate without any deflection (0^{th} order) has a value of $\eta_0 = 0.25$. The efficiency of the 1^{st} order is $\eta_{\pm 1} = 0.101$, while for the 3^{rd} is only $\eta_{\pm 3} = 0.011$ [24]. It can be seen that the efficiency is reducing drastically with a higher order of diffraction. Note that there is no intensity transmitted into the even diffraction orders. Hence these orders have a destructive interference contribution.

In theory, the zone plate efficiency can be improved further by shifting the phase of the waves that have a negative contribution instead of blocking it completely. Shifting a phase by π results in constructive interference, increasing focusing efficiency [32, 37]. However, this is based on the assumption of perfectly phase shifting, which is very challenging to achieve in general, and at present there is no method available can introduce a controlled wave-shift in a neutral helium atom, the way light can be phase shifted.

Chapter 3

Instruments and equipment

The fabrication process of a zone plate requires highly advanced instruments and equipment. This chapter presents and explains the instruments that are used to fabricate the zone plates, namely electron beam lithography (EBL), electron beam evaporation (EBE), and pattern transferring by reactive ion etching (RIE). Additionally, the instrument thin film analyzer used for thin film thickness measurement is explained.

3.1 Introduction to the Raith E-Line

The Raith e-Line is, in principle, a scanning electron microscope (SEM). However, by including extra equipment, it can be used for a low-energy ($\leq$ 30 kV) *electron beam lithography* (EBL). EBL operation utilizes an electron beam (e-beam) to expose an arbitrary pattern on a surface coated with an electron-sensitive material, often referred to as *resist* (section (5.3.1) for more detail about e-beam resist). The e-beam modifies the resist solubility, enabling the selective removal process either on exposed or non-exposed areas by solvent immersion, known as *development*. The Raith e-Line used in this thesis is situated in the Bergen NanoStructures Laboratory (BNSL).

To be able to perform high-quality EBL with Raith e-Line, which is essential for the zone plate fabrication in this thesis, the system is equipped with a Faraday cup, a laser interferometer stage controller, a high-precision sample stage with piezo movement, an electrostatic deflector beam blanker in addition to a pattern generator [27]. The first two components ensure accurate beam-current measurement and high positioning resolution. The pattern generator has an essential role in converting the computer-aided-design (CAD) -file into a deflection signal, which controls the beam blanker, enabling the system to turn the e-beam on and off rapidly. The schematic diagram in fig. (3.1) shows a typical EBL-system's main components.

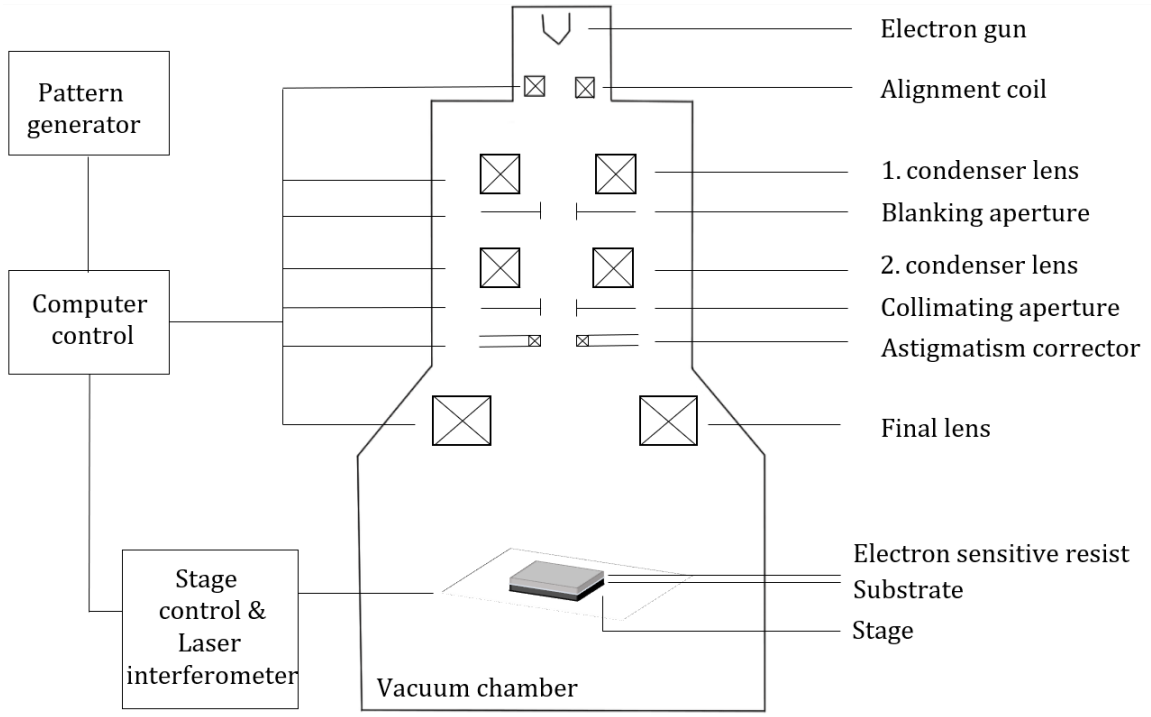

Figure 3.1: Block diagram showing the main components of a typical EBL-system. The image taken and modified from [38].

The software for the Raith e-Line used in this thesis can read pattern files in the format of .CSF, .GDS, .ASC, .ELM, .DXF and .CIF. The pattern is written on an electron-sensitive resist (more detail in section (5.3.1)) by scanning the focus e-beam across the sample surface. In principle, the structures in a design can be categorized into three elements: an area, a line, and a dot element. This is illustrated in fig. (3.2). The maximum area that is covered by e-beam deflection without moving the stage is referred to as a *write-field*. The write-field size in EBL often ranges from a few tens of microns to a couple of hundred microns. It is one of the important EBL setting parameters as it affects the system writing time (the required time in order to expose an area or length completely) and the minimum pixel size, which can be estimated using eq. (3.1)). The Raith e-Line at BNSL is a 16-bit system, resulting in the minimum pixel size (also referred to as *step size*) for a 100 μm × 100 μm write-field is 1.6 nm [38].

$$\text{minimum pixel size} = \frac{\text{write-field size}}{2^{\text{number of bit system}}} \tag{3.1}$$

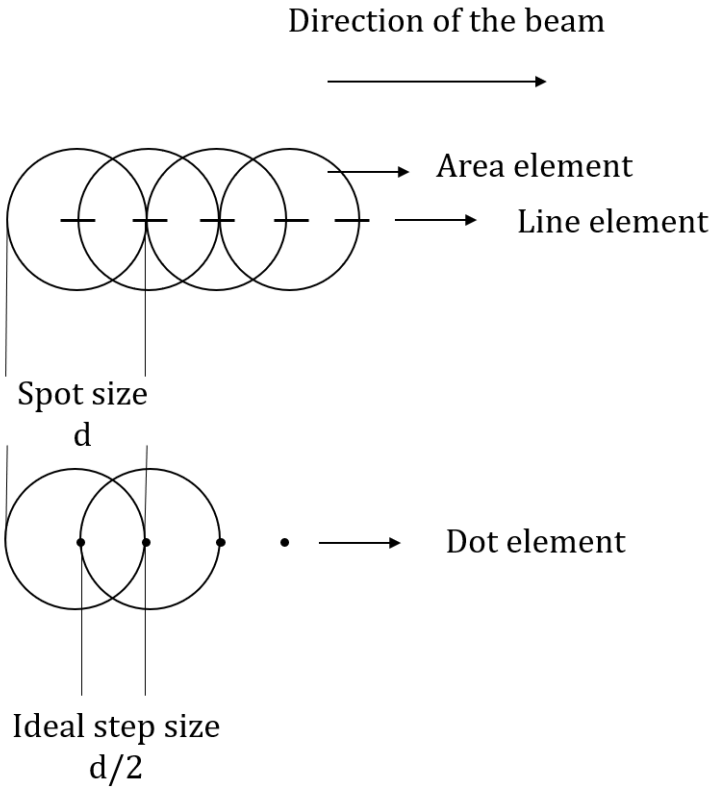

Figure 3.2: The figure illustrates three different element types of the pattern structure in the Raith-software. The diameter of the circles, d, represents the dimension of the e-beam spot size. The step size is the distance between the center of two spot sizes.

The minimum write time at each pixel is referred to as *Dwell time*. The dwell time is also proportional to the *exposure dose*, a variable that describes the amount of the e-beam current at each pixel. More specifically, it can be explained as the amount of electrons per unit area (for an area element) or per unit length (for a single pass) that is required to achieve the desired chemical response in the resist [39]. The relationship between the e-beam and pixel size is illustrated in fig. (3.3).

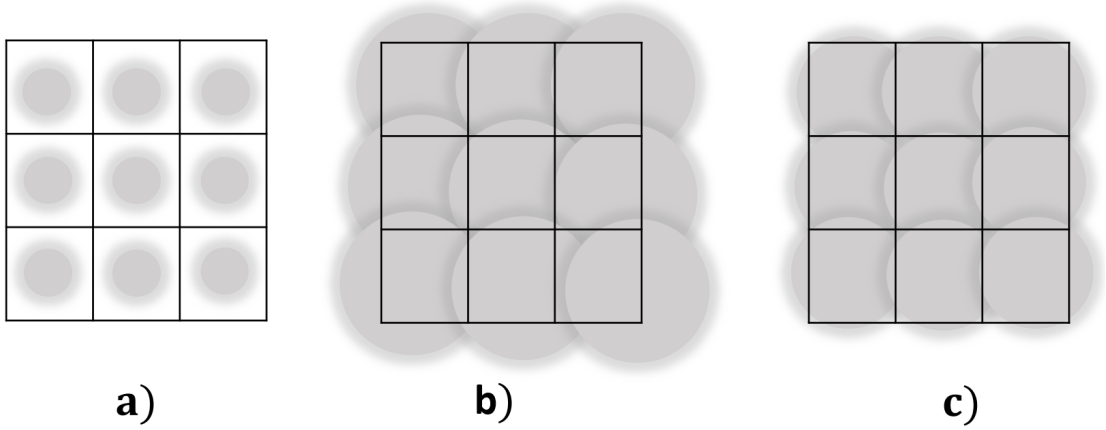

Figure 3.3: The square in the figure represents a pattern pixel. When the beam passes over a pixel, the pixel is exposed to the e-beam. a) is a scenario when the beam size is too small, resulting in the pattern not being completely exposed. In the case of b), the beam size is too large, resulting in an overlapping of the exposed pattern. c) shows a good ratio between pixel and beam size. The inspiration for the figure is taken from [40].

During the exposure process, the parameters, step size, and exposure dose must be determined carefully to achieve optimal results (more detail about the determining of step size and exposure dose parameters, see section (5.5)). As illustrated in fig. (3.2), step size corresponds to the distance between the center of the e-beam spot sizes. Based on [39], the step size value should be approximately half of the beam spot size. Increasing the step size to the value of the beam spot size or beyond will lead to line edge roughness and possibly discontinuity of the pattern [41].

The exposure dose is considered to be one of the most critical parameters in the EBL process. Too high exposure dose (*overexposure*) often results in a pattern damaged by excessive resist clearance. In other words, overexposure effectively enlarges and, in some cases, bridges the exposed features. On the other hand, too low exposure dose (*underexposure*) is often responsible for the exposed area not being completely dissolved after the development.

The optimum value of the exposure dose is limited by several factors, e.g., the resist characteristic properties (detailed explained in section (5.3.1)), the size of the smallest feature in the pattern (pattern resolution), and the pattern density. In the case of high-resolution patterns, the concern of *shot noise* limit must often be considered. In order to obtain the optimum patterning result, the exposure dose needs to be high enough to stay away from the shot noise limit. Shot noise is the statistical variation in the number of electrons in the beam, which is proportional to the signal-to-noise ratio,

S/N. signal-to-noise ratio describes the ratio between the useful signal and background signal and, in this case, can be expressed as: [42]

$$\frac{S}{N} = \left(\frac{\text{exposure dose} \cdot d}{e}\right)^{\frac{1}{2}} \tag{3.2}$$

where d corresponds to the size of the beam spot and e is the elementary charge. In order to achieve a high-resolution EBL, a small beam spot size is required. Thus, the exposure dose must increase to compensate for the smaller d to mitigate the statistical effects of the electron beam (shot noise). In other words, a higher exposure dose is required for a higher resolution pattern in comparison to a lower resolution pattern.

Moreover, the pattern density also significantly affects the optimum value of the exposure dose because of the concern of the proximity effect. The proximity effect here refers to the low background intensity around the e-beam focus. This results in partially exposing the resist surrounding the e-beam focus, which can effectively enlarge the exposed pattern. The proximity effect is of particular concern in the case of high pattern density. One approach to the issue, in this case, is by lowering the exposure dose, which can reduce the issue of the proximity effect.

The step size for each element type is usually chosen to be equal during the exposure process. Hence, the dwell time of an area, a line, and a dot element can be mathematically described as [27, 38]:

$$\text{Area Dwell Time [ms]} = \frac{\text{Area Step Size}^2\,[\text{m}^2] \cdot \text{Area Dose}\,[\mu\text{C/cm}^2]}{\text{Beam-current}\,[\text{nA}]} \tag{3.3}$$

$$\text{Line Dwell Time [ms]} = \frac{\text{Line Step size}\,[\text{m}] \cdot \text{Line dose}\,[\text{pC/cm}]}{\text{Beam-current}\,[\text{nA}]} \tag{3.4}$$

$$\text{Dot Dwell Time [ms]} = \frac{\text{Dot dose}\,[\text{pC}]}{\text{Beam-current}\,[\text{nA}]} \tag{3.5}$$

The beam-current is determined by the system acceleration voltage and can be limited by the system collimating aperture. It is often desirable to minimize writing time in the EBL process. The typical reason is that it is normally more suitable for writing large-scale structures and higher productivity of the process, and for a structure of dimension less than 100 nm due to the ambition of achieving the best possible patterning results.

Lower writing time can increase the beam stability (reducing the beam-current drift and position drift over time) and can reduce a so-called *stitching-error*, the deviation from perfect alignment between adjacent write-fields, as illustrated in fig. (3.4). The total writing time, $t_{writing}$, can be estimated using eq. (3.3) or (3.4), and using the area or length that is illuminated by the beam instead of step size. From eq. (3.3) and (3.4), it can be seen that for a given resist with specific sensitivity and step size, the total writing time is dependent on the beam-current. Hence, using high acceleration voltage and a large aperture will decrease the total writing time. The downside is a less efficient energy transfer of the energetic electrons, resulting in a higher required exposure dose. It should also be mentioned that the higher the energy e-beam is, the greater concern of substrate damage will be.

Further on, the theoretical value of total processing time t_{total} used for EBL is given by a sum of total writing time, stage movement (for structures exceeding the size of a single write-field), and settling time $t_{settling}$. $t_{settling}$ refers to the system delay embedded in the Raith software to ensure that the beam is stable at each new location. [41]

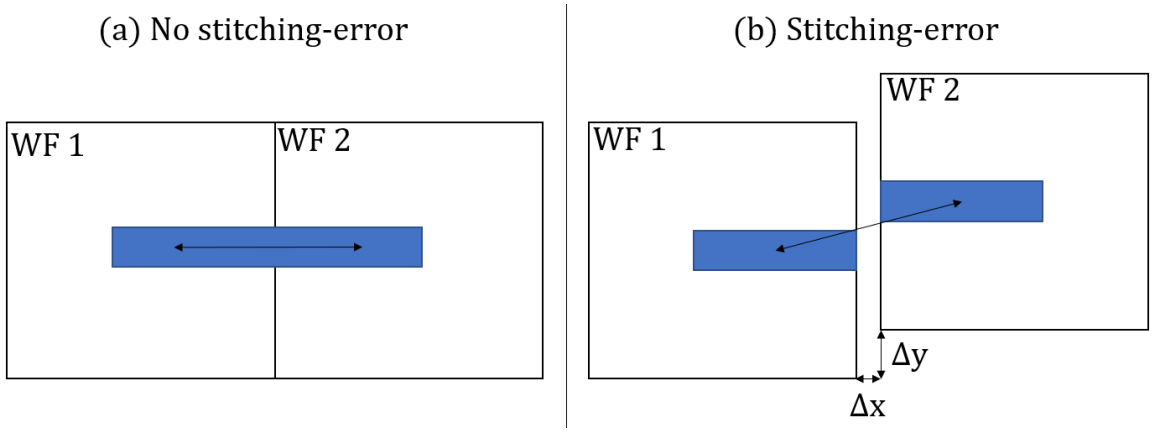

Figure 3.4: Figure demonstrates stitching-error. The large squares illustrate the write-field boundaries, while the blue structure corresponds to the exposed pattern. (a) illustrates a perfect alignment between two write-fields, while (b) is the opposite scenario where a patterning shifting in both X- and Y-directions is presented.

Moreover, the Raith e-Line operates with a maximum acceleration voltage of 30 kV. This is a relatively low amount compared to other dedicated EBL-systems (often $>$ 100 kV) [24]. The main disadvantage of using low acceleration voltage is the broadening of the e-beam spot because of forward-scattering. Consequently, lower resolution and higher line edge roughness. Hence, the ability to penetrate the resist evenly is lower, resulting in a degradation of the sidewall definition. However, the forward-scattering

issue can generally be improved by using thinner resist [43]. The definition of the side-wall can also be improved by development conditions and resist material optimization [44].

The Raith e-Line uses a pattern generator to control the e-beam position. The system converts the electronic pattern image (e.g., CAD-file) into a corresponding signal that controls the beam movement and the beam blanker. How fast the beam moves depends on the clock rate of the system. The Raith e-Line system can operate with a clock rate of 20 MHz. However, in practice, this value is significantly lower due to the recommended beam speed for this system being 10 mm/s [38]. Using a higher beam speed is possible, but it will also increase the risk of artifacts.

An important consideration when performing electron beam lithography is the pattern size. The system cannot be patterning without moving the substrate for a large design that extends over more than a single write-field. One of the most common techniques is to divide the pattern into several write-fields, which then will be stitched together via controlled stage movement. The stage movement at extremely high precision is required for an optimized result. Here is where the importance of the laser interferometer and the sample stage with piezo-table comes to play. With these components, the stitching-error can be reduced, and the obtained precision of the stage movement can be up to 2 nm [24]. In addition, the e-beam deflection of the system must be adjusted to match the stage movement, often referred to as *write-field alignment*. An alternative method for patterning a large pattern is *fixed-beam-moving-stage* (FBMS) which is a technique that writes a pattern continuously by moving the stage while the beam remains approximately constant. More information about FBMS, see chapter 14 in [38].

Lastly, the Raith e-Line system uses a Gemini column with a Schottky thermal field emitter to produce the electron beam. The advantage of the Gemini column is that it produces a remarkably small e-beam spot, enabling the lithography process at a high-resolution. As mentioned, the Raith e-Line is equipped with a Schottky thermal field emission source consisting of a tungsten tip. Usually, the tip is coated with a layer of zirconium oxide (ZrO). It is heated at an elevated temperature ($\sim$ 1800 K) in order to melt the ZrO and wet the tip (with ZrO). Consequently, the potential barrier (i.e., work function at approximately 2.7 eV) is decreased, making it simpler to extract electrons, which increases the efficiency of the electron emission process and allows the system to obtain a smaller beam crossover. Additionally, the tungsten tip is less sensitive to environmental gases and can achieve stable operation for months. As a result, it features a minimal virtual source size and moderate energy spread [45]. Alternative electron emission source is cold field emission type and the lanthanum

hexaboride (LaB_6)-tipped filaments. The latter has the lowest brightness, while the cold field emission type scores best on the brightness. However, the Schottky thermal field emitter is more beneficial to lithography applications because of its high emission current stability. [46]

3.2 Electron-beam evaporator: Temescal FC-2000

Electron beam evaporation is one of the modern electron beam physical vapor deposition (EBE) techniques. This technique is often used for thin-film deposition processes. Briefly, the target material which is to be deposited onto a sample surface is heated up by a controlled electron beam. It sublimates, and the vapor of sublimated material condenses onto the sample surface with a given deposition rate. The expected result is a uniformly coated sample.

The system used in this thesis is Temescal FC-2000. Available deposited materials are gold, SiO_2, chromium, titanium, aluminum, and nickel [14]. A schematic representation of the system is shown in fig. (3.5). An electron beam is generated by applying 10 kV voltage across a filament. As illustrated in fig. (3.5), a magnetic field is applied to control the electron beam propagation path such that the beam is circulated towards the target material. The beam is swept across the target material, forming an even exposure. Evenly exposure is important, especially for materials with low thermal conductivity. This is because the heat will not spread, and most likely, only the middle region of the crucible will be evaporated.

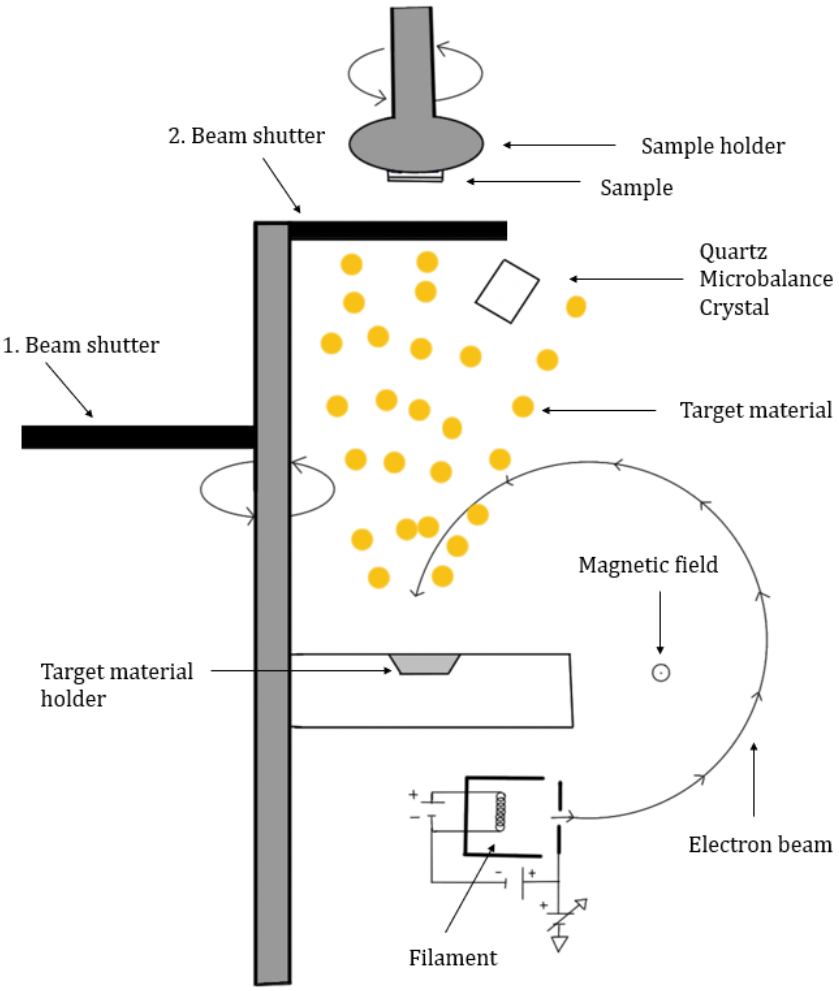

Figure 3.5: Schematic representation of a typical EBE-system.

The Temescal FC-2000 system has two shutters, which are essential to the system deposition rate. The first shutter covers both the detector and the sample. This shutter opens up after the deposition material is preheated, enabling the vapor to expose the *Quartz Crystal Microbalance* (QCM), which allows the system to regulate the deposition rate. The QCM measures correlating frequency changes when the mass has been deposited. The mass to frequency correlation is determined by Sauerbrey's equation: [14, 47]

$$\Delta f = -\frac{2f_0^2}{A\sqrt{\rho_q \mu_q} \cdot \Delta m} \tag{3.6}$$

where Δf is the change in frequency, f_0 is the value of QCM's resonance frequency. ρ_q, μ_q, and A are crystal quartz's density, the shear modulus of crystal quartz, and the piezoelectrically active crystal area, respectively. The mass difference of the crystal quartz due to the deposited material is Δm.

After the deposition rate reaches a specified value, the second shutter opens, exposing the sample to the vapor. As the density of the target material ρ_d is known, the thickness of the deposited layer Δx can be determined using eq. (3.7) as following:

$$\Delta x = \frac{\Delta m}{\rho_d A} = -\frac{\sqrt{\rho_q \mu_q}}{2 f_0^2 \rho_d} \cdot \Delta f \tag{3.7}$$

In addition to other components, the system has two holders, one at the bottom for the target materials aligned with the second one on top, which is for the sample to be coated. Just as importantly, all of the components are in a vacuum chamber. When the material is heated up by electrons, what happens on the atomic scale is that the electrons transfer their kinetic energy onto the target material as thermal energy. Hence putting the system in a vacuum will result in a lower evaporation temperature of the material than under normal atmospheric pressure.

3.3 Reactive-ion etcher: Plasmatherm 790+

Reactive-ion etching (RIE) is a type of plasma etch technology that combines dry-etching and chemical-etching [48]. In contrast to chemical wet-etching, RIE provides a high level of anisotropic etching, enabling the possibility of precisely removing desired sample parts.

A typical schematic of an RIE is shown in fig. (3.6). The system has two electrodes; the top one (upper electrode) is connected to the ground, while the lower electrode is connected to a so-called *RF-power supply*. An RF-power supply alternates the direction of the oscillating electric field $13.56 \cdot 10^6$ times every second, corresponding to radiofrequency (RF) [48]. Noteworthy that the lower electrode on which a sample is placed is also connected to a blocking capacitor, providing a direct current (DC) isolation. As a result, the lower electrode is gradually biased to a negative potential resulting in low electron density around the electrode (they are being pushed away). This region is referred to as *ion sheath*.

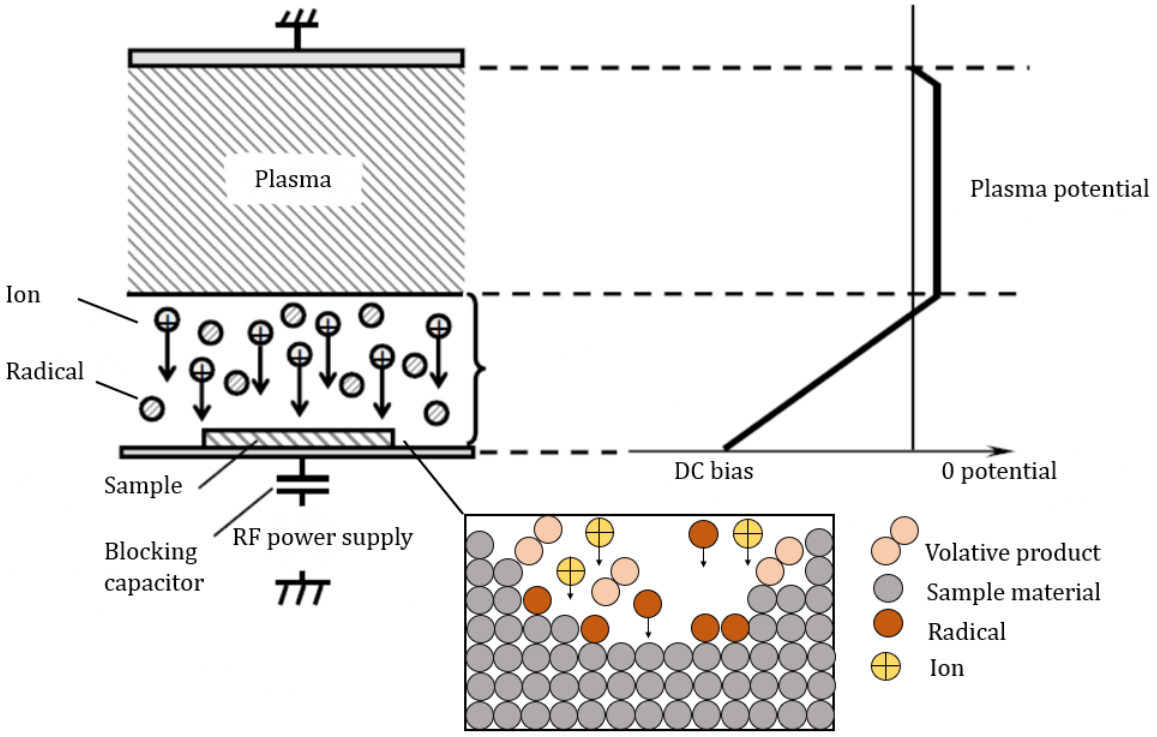

Figure 3.6: Figure shows a typical RIE system. The magnified image shows the surface reaction of the sample. The figure is taken and modified from [48].

The main principle of a typical RIE-system is to use an RF-power supply to generate an oscillating electromagnetic field between the two electrodes. The electrons in the electromagnetic field accelerate with high energy and collide with atoms and molecules in the gas that flows through the chamber. Many different collision processes can occur with these electrons [48]:

i. **An elastic collision with gas atoms.** The kinetic energy is changed, and a portion of the electron's energy is transferred into the kinetic energy of the gas atom. However, the internal energy remains unchanged.

ii. A **collision between electrons and gas atoms, referring to as a *excitation*-process.** The bound electron in the atom jumps into a higher energy level due to the energy transfer from the collision. Within a short period of time, the excited electron returns to the ground state, and the energy in the form of photon is emitted during this transition.

iii. **A collision between electrons and gas atoms, referring to as an *ionization*-process.** The outermost shell electrons of the molecule or atom are expelled (this occurs when the electrons have greater energy than the ionization

energy). As a result, the gas atom is turned into a positive ion in addition to the expelled electron.

iv. **A collision between electrons and gas molecules, referring to as a *dissociation*-process.** The gas molecule is dissociated into a so-called *radical*, byproduct particles in the activated state, which are chemically more reactive than the original molecule. This process can occur if the accelerated electron has higher energy than the atom's binding energy.

v. **A collision between electrons and gas atoms, referring to as an *electron attachment*-process.** The accelerated electron attaches to the atom, resulting in the atom turning into a negative ion.

The collision processes mentioned above result in a gas consisting mostly of free charged particles (e.g., electrons and protons), neutral atoms, molecules that coexist, and a low amount of ions. This is referred to as *weakly ionized plasma* as the degree of ionization is low (order of $10^{-6} - 10^{-4}$) [48].

The electrons in the plasma accelerate up and down in the chamber along with RF electric field. On the other hand, the more massive ions respond much slower, so the ions' movement are decided by Brownian motion. However, when electrons hit the powered electrode, the charge accumulation occurs due to the DC isolation. A negative DC-bias is created on the electrode, while the plasma is positively charged due to a higher concentration of positive ions. The voltage difference between plasma and electrode will accelerate ions toward the sample resulting in a surface bombardment. The etching process is driven mainly by these ions. As they propagate perpendicularly onto the sample surface, the ions etch the sample through the chemical reaction between ions and surface material and also by applying their momentum and sputter off some of the sample material. An anisotropic profile (with a possible small dimensional shift from the etch mask) can be obtained. Fig. (3.7) shows an example of RIE etching reaction steps when a Si substrate is etched with CF_4 . [48]

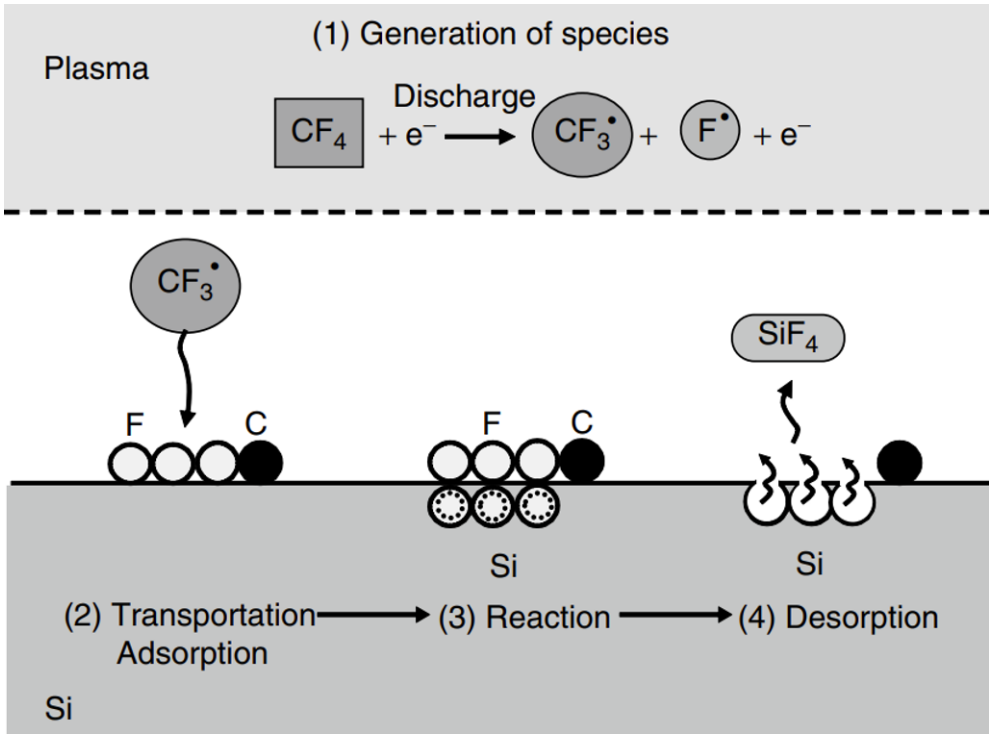

Figure 3.7: Reaction steps of RIE when a Si substrate is etched with CF_4. (1) Neutral radicals and ions are generated in the plasma. (2) Ions and radicals hit the sample and get adsorb. (3) Chemical reaction between ions, radicals, and surface materials creating byproducts. (4) The byproducts are desorbed and transported away from the chamber. The image is taken from [49].

In practice, the performance of the RIE process can be affected by several parameters, such as the chamber pressure, temperature, etch duration, gas flow rate, RF-power. The etch rate, sidewall profile angle, and structure damage are limited by the mentioned factors. A high etch rate and vertical sidewall profile are often a high priority since it can save time, enhance the possibility of mass production, and improve the quality of the fabricated structure. In order to get satisfying requirements associated with anisotropy, etch rate, and selectivity at the same time, the following should be optimized and determined carefully:

- **Mean free path and system pressure:** An important factor that affects the anisotropy of the dry-etching process is the ratio between mean free path (MFP) (an average distance that a particle can travel without collision) and ion sheath thickness. The ion sheath thickness mainly depends on the ion mass and plasma potential. The MFP is inversely proportional to pressure since fewer molecules exist when the gas pressure is low. When the ratio between MFP and ion sheath is large, the probability that ions can direct onto the sample without any scattering is higher. This directionality of ions plays a great role in etching rate as illustrated in fig. (3.8). For the scenario with high-pressure, fewer ions

enter the small area, resulting in a lower etch rate than in the opposite scenario. However, an adequate number of ions can still enter a large pattern. In other words, the etch rate becomes pattern dependent on the high-pressure system. It is also worth noting that the ions coming in at an angle will increase the risk of sidewall etching, which affects the anisotropy [48].

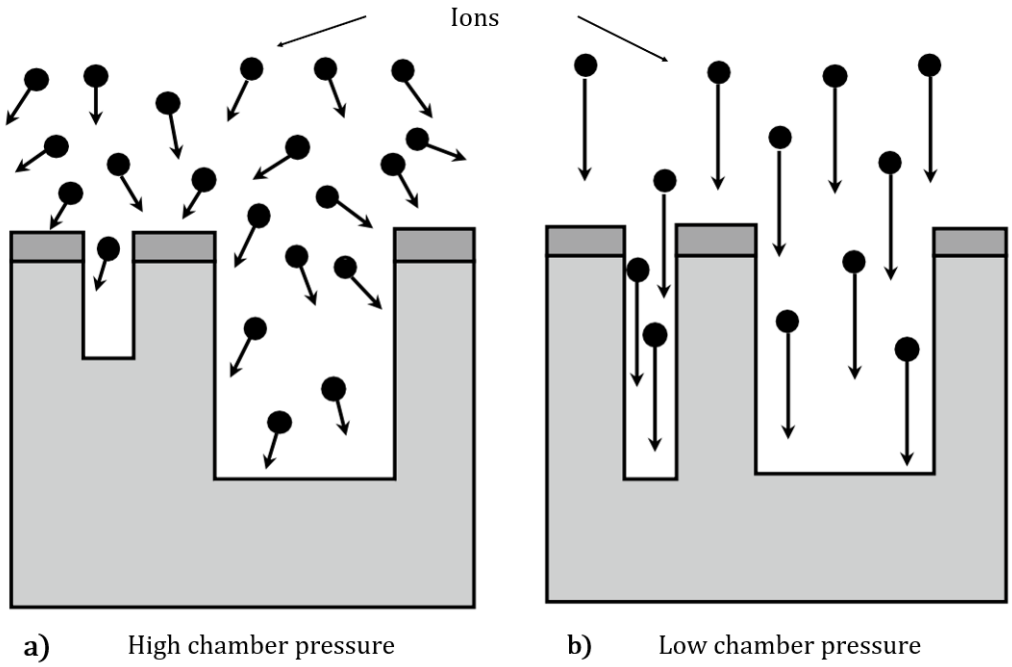

Figure 3.8: Figure shows the effect of the chamber pressure. a) is the scenario with high chamber pressure and small MFP. As a result, ions travel in different directions due to a higher probability of scattering. In the a) scenario, the etch rate becomes dependent on the pattern, opposite of b), where the chamber pressure is lower. The image is taken and modified from [49].

- **Radical and ion-assisted reaction:** When radicals mainly drive a dry-etch, the etching does not only proceeds vertically but also in the horizontal direction. This is due to the fact that radicals are massive and do not respond quickly enough to the RF electromagnetic field. As a result, their movement is randomly and decided mainly by Brownian motion, limiting the anisotropy of the etching process. One of the approaches to the implementation of anisotropic etching is *ion-assisted* reactions. Ion-assisted reaction is referred to incoming ions colliding with radicals and enhancing the surface reactions. As a result, etch rate is higher where an ion-assisted reaction occurs compared to etch rate by radicals alone [48]. When ions come in vertically relative to the surface, the etch rate in the vertical direction will be greater than etch rate in the horizontal direction (by radicals), hence, an anisotropic etch is obtained. However, ion-assisted reactions are dependent on the target materials and the etch gas composition [48].

- **DC-bias:** DC-bias is one of the essential parameters to obtain desirable etching characteristics. RF-power mainly limits the magnitude of the DC-bias as it contributes to a proportional increase of the DC-bias. That being said, DC-bias also depend on other parameters, including chamber pressure [50] and the gas composition [51]. The importance of DC-bias is because of the ion energy dependency of the RIE physical sputtering. RIE with high energy will etch more vertically and with a higher rate [48]. However, the major downside of high ion energy is lower selectivity due to high ion bombardment. It means the process etches different materials at approximately the same rate. Lastly, some RIE processes are more a physical-type reaction, meaning the processes are primarily dependent on ion energy rather than the gas composition [52].

- **Gas composition:** The gas composition is important for surface reaction, and the desorption of the etch byproducts [48]. The choice of the gas composition is often based on whether the ions/radicals can form volatile products to be removed from the sample. For example, think of a scenario with silicon- (Si) based materials. Fluorides of Si and tungsten (W) have higher vapor pressures than, for instance, chlorides. This means the etch byproduct is more volatile (desorb more efficiently), hence, the etch rate is increased [48]. Due to that reason, the F-based gasses are more preferred than Cl-based gas for etching Si- and W-based materials.

- **Sidewall protection:** Another factor promoting the anisotropic etching is the sidewall protection process. Sidewall protection refers to a protective thin film that can be formed by several methods, e.g., organic polymers formed from carbon in the gas mixture (e.g., CHF_3). As a result, the sample surface is covered with a protective thin film. Since more ions come in perpendicularly to the surface, the protective thin film on the horizontal surface will be removed faster than the sidewall area. Hence, the sidewall remains protected during the etching process, and anisotropic etching is realized.

3.4 Filmetrics F10-RT

Thickness control of the deposited layers was an essential process to achieve the best possible results for the zone plate fabrication in this thesis. It was especially important for the electron-sensitive resist, as the resist thickness greatly affected the lift-off process and the achievable resolution. Additionally, the etching mask thickness played a significant role in the characteristics of the results in dry-etch processes. An

accurate thin film thickness can be obtained using a thin film analyzer (Filmetrics F10-RT).

The main principle behind the Filmetrics F10-RT is to illuminate a thin film sample with lights and then capture the fraction of incident light transmitted and reflected by the sample, referred to as transmittance and reflectance, respectively. Further, the instrument's software uses the obtained spectra and pre-selected material optical properties (e.g., refractive index, cauchy, etc.) to calculate the thin film thickness. Practically, the software estimates the thickness based on curve fitting for the thickness closet resembling the measured reflectance spectrum. The agreement between the calculated and the measured reflectance spectra is defined by a parameter in the software called "goodness of fit". An example of a thin film thickness measurement using the thin film analyzer is shown in fig. (3.9).

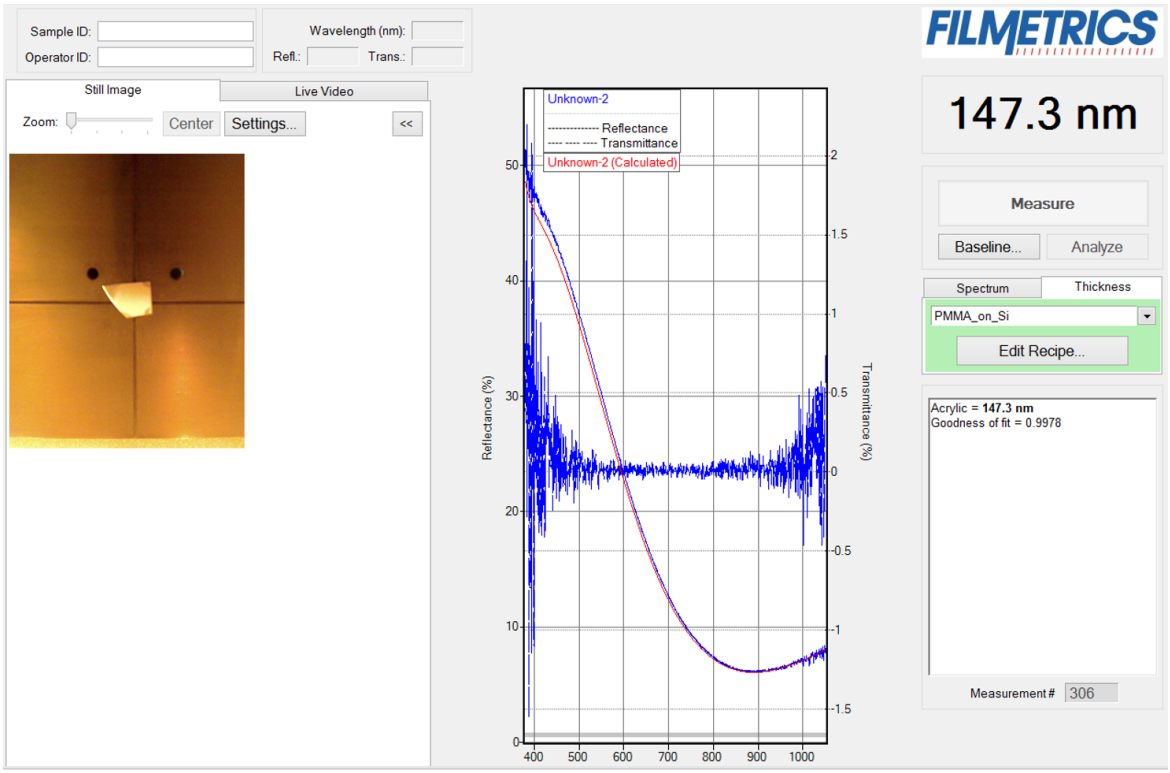

Figure 3.9: An example of a result from thin film thickness measurement in the software. The blue and red curves show the measured and the estimated curve of the sample reflectance spectrum, respectively. The white box on the right side shows the thickness value of the parameter goodness of fit (referring to how well the estimated curve fits with the curve of the measured reflectance spectrum).

Chapter 4

Characterization and investigation

Characterizing and analyzing the results from EBL, material deposition, and RIE processes were an essential part of the works in this thesis. The following chapter presents the scanning electron microscope (SEM), sample inspection using SEM, and the two thin film analysis methods used in this thesis.

4.1 Sample characterization using SEM

4.1.1 scanning electron microscopy

A scanning electron microscope (SEM) is an extensively used instrument in this thesis, mainly to inspect and characterize the sample. The reason is that SEM can provide exceptionally high-resolution surface imaging with a decent depth of field (DOF). DOF describes the axial depth of the space on both sides of the object plane (in this case, the plane of the focused electron beam) within which the object can be moved without detectable loss of sharpness in the image. Hence, a decent DOF means the posibility to obtain three-dimensional appearance of the images. In addition, SEM is relatively easily operated, maintained, and less time-consuming for sample preparation than other high-resolution images such as transmission electron microscope (TEM). [53]

As mentioned in section (3.1), the SEM used in this thesis is Raith e-Line, situated in BNSL. A brief explanation of how SEM works is scanning a focus electron beam (e-beam) over a sample and detecting the electron interactions at each point. As a result, an image where each pixel corresponds to the detected information from each scanning point is obtained. The interaction of electrons and the atoms in the sample produces various signals that contain information about the sample's surface topography and composition. In the case of the Raith e-Line system, the two most important electron interactions are as follows: First, elastic scattering at a large angle from the incident

direction and typically retains $60-80\%$ of the incident electron energy, this is referred to as *back-scattered electron* (BSE) [53]. On the other hand, an inelastic scattering, relatively at a small angle, shows much lower energy than the incident electron, referred to as *secondary electron* (SE). Further on, SE can be characterized into SE1, SE2, and SE3. The first mentioned is secondary electrons generated by the primary e-beam. SE2 and SE3 are generated by BSE and the collision of BSE in the chamber, respectively. Noteworthy that the secondary electron generation is the main reaction mechanism that causes resist exposure during lithography.

A typical SEM consists of a system where a column situates in a vacuum chamber. At the same time, a sample is located at the bottom. Electrons are emitted from an electron gun within the column (see section (3.1) for more detail about the column and electron gun in the Raith e-Line system). The e-beam path goes through several sets of electromagnetic lenses, including condenser and objective lenses. The condenser lenses reduce the crossover diameter of the e-beam before passing through an adjustable collimating aperture. An objective lens limits the amount of electrons, shapes the beam, and secures a nano diameter scale of the e-beam probe. Finally, SEM-system is of several deflection coils as they ensure the beam movement with the XY-plane and facilitate scanning across the sample.

The Raith e-Line is equipped with two different detectors for electron signal detection, an InLens-detector and an Everhart-Thornley (E-T) detector for SE. The InLens detector is located inside the column, directly above the sample. In contrast, the E-T detector is located in the chamber at an angle relative to the sample. The SEs are pulled to the detector with a strong positive electrically bias.

For the comparison, the InLens-detector detects mainly SE1 and the low energy SE2, giving rise to a higher signal-to-noise (S/N). This is because the InLens-detector collects less noise signal that SE3 defines. Additionally, the InLens-detector is more sensitive to lower energy SEs than the E-T detector. As a result, the InLens images often contain more surface detail, while images with E-T detector contain more information about the material in the sample. However, since the InLens is positioned above the sample, the result is an even image without shadowing. In contrast, the E-T detector is positioned at an angle, giving rise to extra topographical information and shadowing.

4.1.2 Inspection methods

Important considerations and preparation

To obtain a good/desirable imaging with SEM for the sample investigation, the following considerations were necessary:

i. **The system acceleration voltage (AV) and collimating aperture:** The system acceleration voltage during the investigation process in this thesis often varied from a range between 5 kV - 10 kV. The system collimating aperture was often selected to be 15 μm , 20 μm , or 30 μm . Choosing the value of acceleration voltage and collimating aperture need to be done wisely, as these parameters affect the e-beam probe current and size. Thus, it is often desirable to minimize probe size and maximize probe current to obtain high resolution. Other factors that affect the determination of acceleration voltage and collimating aperture are, for instance, the sample type, the influence of charge accumulation (known as the charging effect), the concern of sample damage, and the desired resolution and DOF.

ii. **Working distance (WD):** Working distance refers to the distance between the bottom of the column and the sample. A minimum diameter of focused e-beam is typically obtained at a specific and optimized WD. Small WD results in high resolution but smaller DOF, and vice versa for large WD. The optimization can be done by iteratively varying WD until the best focus or the desirable effect is achieved. A working distance in a range of 10.4 - 10.7 mm was used in this thesis work.

iii. **Brightness and contrast:** Image brightness refers to the effect of making the image lighter or darker, while the term contrast describes the difference between the lightest and darkest regions in the image. The optimization of these two parameters strongly depends on the sample conditions (such as the presence of dust or contamination), and often needs to be adjusted during imaging.

iv. **Aperture alignment**: The aperture and e-beam in the system should be aligned to improve the image's quality. The allignment can be done by adjusting the value of aperture alignment in X- and Y-direction to minimize any image's lateral movement when the focus is varied in and out.

v. **Astigmatism**: Astigmatism is an aberration caused due to imperfections in the lens system, resulting from the power differences of a lens in its lens plane perpendicular to the optical path. Astigmatism results in the beam not being perfectly circular. Features in the image become elongated when the focus is varied in and out. One method for astigmatism correction is by iteratively adjusting two knobs, X and Y, of the stigmator (a component that adjusts the

electromagnetic field of the objective lens in two perpendicular directions [53]) so that the stretching of the image in both directions is minimized.

vi. **Charging effect**: Surface charging was one of the substantial challenges during the inspections of the works in this thesis. This effect occurs when excessive electrons accumulate on the sample surface where it is impinged by the e-beam. Consequently, the electrical charges can cause unusual phenomena such as abnormal contrast and image deformation in SEM images. The charging effect is especially concerned for nonconducting sample surfaces. Since the works in this thesis were involved working with nonconducting material such as free-standing membrane of Si_3N_4 and a thick layer of etching mask consisting of anti reflective coating polymer (ARC), SiO_2 and PMMA, the difficulty in imaging and the effect of charging was an issue.

   One way to approach the issue of the charging effect is to reduce the probe current by lowering acceleration voltage and minimizing the collimating aperture. Another approach is to coat the sample with conducting material to increase the sample conductivity. In this thesis both methods was applied. Usually, a 4-5 nm chromium was deposited using EBE prior the electron beam exposure. For SEM imaging a thin layer of gold palladium (AuPd) was sputter coated onto the sample. The sputtering method was generally preferred due to the less undemanding procedure and the lower risk of radiant thermal damage to the sample [54]. That being said, a thin layer of conducting material can improve image quality, contrast and resolution. The main reasons are that the coating material can increase the signal-to-noise ratio (due to the ability of the deposited material to emit more electrons) and that an omnidirectional coating is achieved in the sputtering coating process, giving an arise to a greater contrast. However, the drawback of coating conductive material upon the sample is that the sample surface lost the original information, and therefore the original atomic number contrast is lost. Also important to mention that a too thick layer of conducting material can result in granular and cracked, which may distort the original topographic feature.

Method

As mentioned, after each fabrication process (i.e., EBL, etching, and thin film deposition), the usual procedure was to inspect the results using SEM. The ambition was to obtain information about the dimension of the exposed or etched area, as well as to characterize defects, stains and residues of the sample surface. The inspection was normally done by imaging the sample with the InLens detector due to a high detailed

image of the sample surface and sufficient signal-to-noise ratio. The dimension of the exposed or etched structures was measured using the scale-bar and the built-in measurement tools in the e-Line software. Fig. (4.1) shows an example of a result inspection. A tilt sample holder was used to inspect the etching profile and thickness measurement of layers. More information about thickness measurement is provided in the next section.

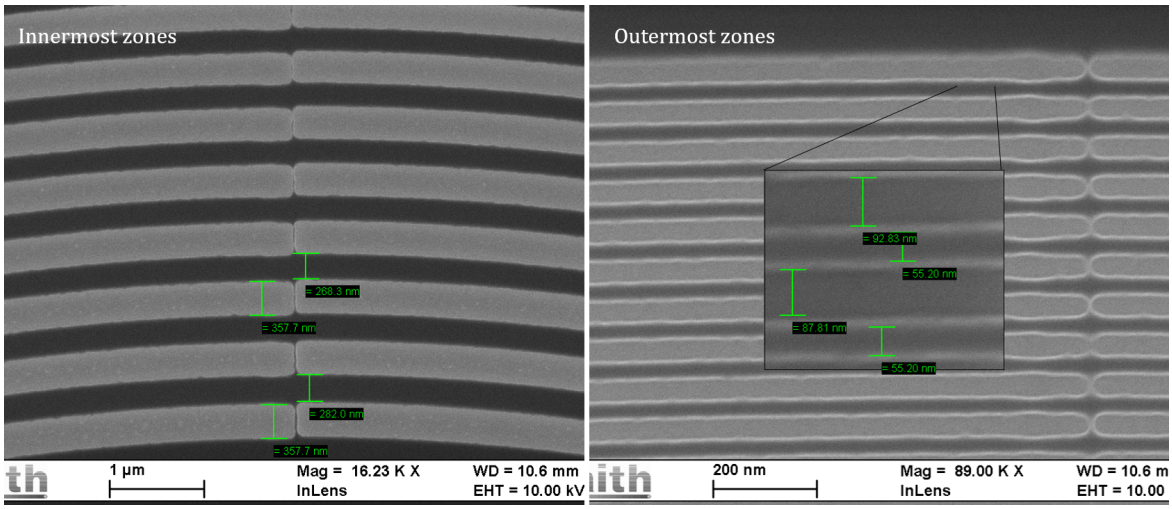

Figure 4.1: SEM images of the zone plate pattern in PMMA layer (not etched). The left image shows the area around the innermost zones, while the right image shows the outermost zones. The images were used for zone width and dose inspection. The distance measurements were done using a built-in function together with the scale-bar at the lower-left corner of the images.

4.2 Thickness measurements

Two different methods for the thickness measurement were applied in this thesis. The first method was by using a thin film analyzer. It should be mentioned that due to the size of the chip, thickness measurement using thin film analyzer could not be done directly on the membrane chip. Instead, the thicknesses were measured by depositing material of interest on a large silicon wafer. At least ten measurements were done with an appropriate setting of material optical properties. The sample was positioned differently for each measurement, and only the measurements with the goodness of fit above 90% were recorded.

The second method was to investigate the sample cross-section at 45° and 90° using the SEM. The coated sample was cleaved and mounted on a tilting holder with conductive carbon adhesive tabs. The thickness was measured using the scale-bar and the built-in measurement tools in the e-Line software. It is worth mentioning that the

thickness measured at 45° is not corresponding to the actual film thickness. The measurement must be multiplied with the factor of $\sqrt{2}$ (derived from Pythagoras theorem) is necessary due to the 45° tilt.

Chapter 5

Fabrication process

This chapter gives a detailed description of the fabrication procedure of the free-standing Fresnel zone plate used in this thesis. Start with a brief overview of the fabrication process, followed by pattern designing, selecting and optimizing the layers, and the preparation of the membrane chip. The investigation methods of different working parameters will are provided as well as a detailed description of the final fabrication procedures.

5.1 Fabrication Overview

An overview of the fabrication steps of the free-standing Fresnel zone plate is illustrated in fig. (5.1). However, many additional processes were necessary to achieve the best possible results of the zone plates. This includes designing the structures suitable with the NEMI parameters (see [13] for more detail about NEMI) and the fabrication methods. Selecting and optimizing the working parameters such as the thickness of the layers, exposure, and etching parameters were also essential. The optimization processes will be explained more fully in the next sections.

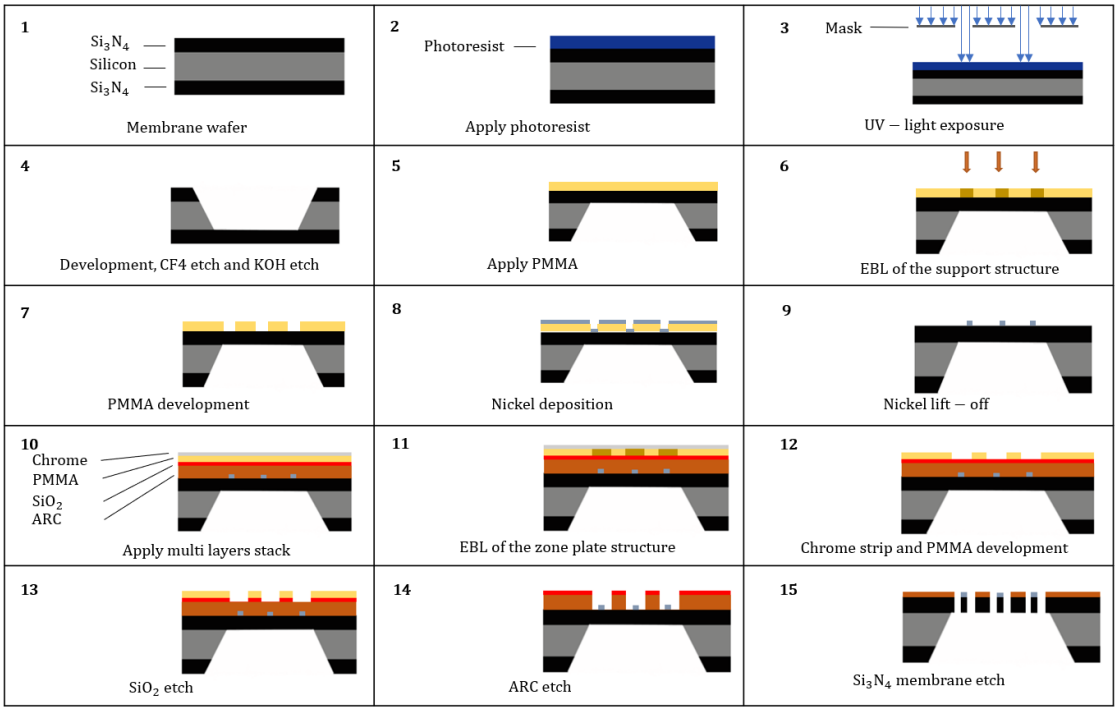

Figure 5.1: The figure shows fabrication steps of the free-standing Fresnel zone plate in this thesis. Steps 1 - 4 illustrate the Si_3N_4 membrane chip preparation steps, while steps 5 - 9 illustrate the exposure and the creation of the hard-mask of the support bar structure. Step 10 shows the multilayer stack, followed by the zone plate structure exposure in step 11. Steps 12 - 15 illustrate the development and pattern transferring of the structures to the Si_3N_4 membrane.

5.2 Design of the structures

The zone plate structures used in this thesis could be designed using different methods in principle. Raith has software for this purpose. It generates a circle element (i.e., area element) pattern with a specific dimension and a width corresponding to the m^{th} width of the zone. Based on the previous work in [24], the final dose and the width of the patterning result for the area element can be challenging to predict. The second method is by using MATLAB script, written for the original zone plate work done by Thomas Reisinger (see [24]) to generate Raith-specific syntax to construct zone plate structure by defining the patterns as zero-width polygon elements (i.e., line element) that are uniformly distributed over the circular zone. As a result, circular zones can be formed. The latter method was preferred since the MATLAB script made it possible to control more parameters such as dose-addition (explained in more detail later) and for the fact that it should be easier for the EBL-system to expose straight lines instead of curved area element. The second method was also applied to construct the support bar structure.

The scripts were originally written by Tymon Barwicz at MIT in 2003, adapted by Thomas Reisinger later, and lastly by the author of this thesis. The latest modified version used in this thesis can be founded in Appendix (A). The MATLAB script takes different input parameters (e.g., focal length and zone plate diameter) and generates the pattern as an ASCII text file. The ASCII code is written in Raith-specific syntax, converted to a GDSII (a file format representing planar geometric shapes and other information about the layout in hierarchical form), and reproduces the pattern when imported to the e-Line software. An example of the ASCII code in Raith-specific syntax forming a line element is shown in fig. (5.2).

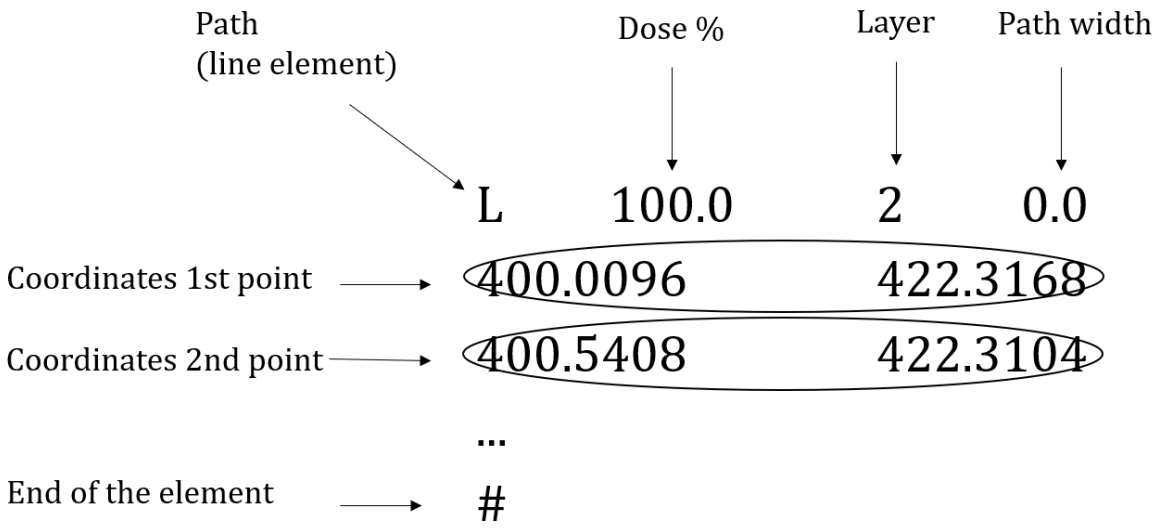

Figure 5.2: Figure shows an ASCII code defining a path structure written in Raith-specific syntax. The figure inspired from [38].

It is important to mention that the output coordinates have to be rounded to be multiples of parameter m_{step} in the MATLAB script. The parameter m_{step} corresponds to the step size of the e-Line system. The smallest possible step size value for 100 µm × 100 µm write-field is approximately 2 nm, determined by the 16-bit pattern generator. Without rounding the coordinates, the patterning results could be very unpredictable [24].

Another critical parameter in the MATLAB script is r_{step}, defined as the distance between the zero-width polygon elements that form the zones. This parameter was chosen to be three times larger than m_{step} based on the works from Thomas Reisinger in [24]. The smaller value of r_{step} is, the more polygon elements it is to form the zones (i.e., higher pattern density). Consequently, the exposure dose needed to be controlled carefully to avoid overexposure of the pattern due to the proximity effect.

Lastly, the parameter *working-area* is related to the size of the total exposure area. This parameter is set to 1000, corresponding to 1000 μm × 1000 μm working area. The value of this parameter was based on the size of the free-standing membrane window, as it is desirable that a so-called alignment mark was located just outside the membrane (more detail about alignment mark in section (5.2.3)).

5.2.1 Support bar structure

The zone plates fabricated in this thesis were made to focus the low-energy helium beam. Consequently, the transparent zones must be completely open since the neutral helium beam does not penetrate solid material. Hence, the blocking zones are hanging freely and need to be held in place by a support bar structure to prevent the zones from collapsing. The width of the support bar structure was adopted from [24, 55] chosen to be approximately 450 nm, as it should be as small as possible in order to minimize the blocking of the transparent zones (but still wide enough to support the zones). This thesis created two different designs of support structure based on NEMI parameters (see [13]) and the He-beam wavelength. However, due to time limitations, only the design for liquid nitrogen cooled He-beam was used throughout this thesis.

The construction of the support bar structure begins with two perpendicular bars (relative to each other) that are centered at the center of the zone plate structure. In order to support the structure properly, more support bars (secondary support bars) are iteratively added based on the fact that the ratio between the length and the width of the free-standing segment must be less or equal to a factor of 30. This factor was determined from the assumption that a 50 nm wide zone plate ring structure is stable if the length does not exceed 1.5 μm. This resulted from the previous works in [24, 55], see eq. (5.1). Starting from the innermost zone, the condition in eq. (5.1)) is checked, and if it is not fulfilled, several secondary support bars will be added to the structure.

$$\frac{\text{Length of the freestanding segment}}{\text{Width of the freestanding segment}} \leq \frac{1500[nm]}{50[nm]} = 30 \tag{5.1}$$

The length of the freestanding segment depends on the radius of the mth zone, r_m and the number the existing support bars, S_m. Eq. (5.1) can be rewritten as:

$$\frac{r_m \cdot 2\pi / S_m}{\Delta r_m} \leq 30 \tag{5.2}$$

where Δr_m is the width of the mth zone. Fig. (5.3) illustrates the GDSII of the support bar structure used in this thesis in the e-Line software.

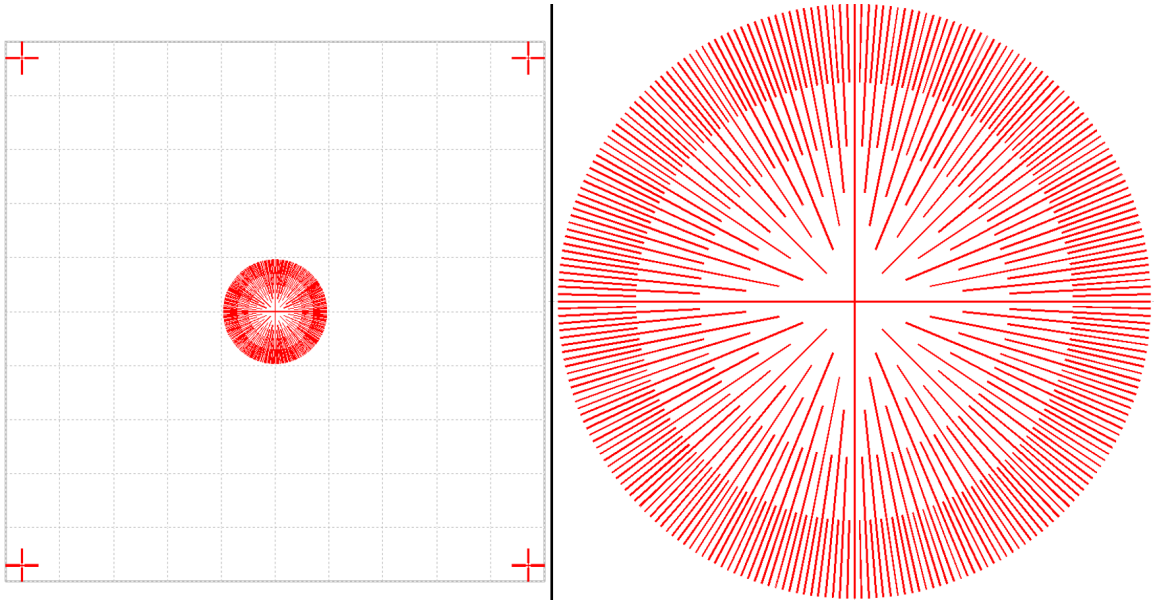

Figure 5.3: The figure shows the support bar structure used for the cold helium beam. The left image shows the whole working-area of the GDSII-file with alignment marks (crosses in each corner). The right image shows the support bar structure design.

5.2.2 Zone plate pattern

The design of the zone plate structure was based on the theory from section (2.2), whereas the structure consists of radial zones alternating between being opaque and transparent (fig. (2.5)). The constructively interfering waves can pass through transparent zones, which are odd-numbered zones. In contrast, the opaque zones block out the destructive interfering waves.

Four different designs of the zone plate structure were created in this thesis. Due to time limitations, only two of the designs were used. Both zone plate designs are for liquid nitrogen cooled He-beam, and the difference between them is the size of the central block (CB_{ZP}). The central block refers to the blocking of the innermost zones. The ambition of central blocking is to achieve a higher signal-to-noise ratio of the 1^{st} order diffraction by blocking the 0^{th} order diffraction intensity, which is the primary source of the background signal. In return, blocking a certain amount of the innermost zones will also reduce the intensity of the 1^{st} order diffraction. Consequently, focusing efficiency is reduced, and chromatic aberration is increased [56]. Two different sizes of central blocking resulted in a slight difference in the characteristic parameters, for instance, the total number of zones and the width of the innermost zone. The zone plate characteristic parameters, the parameters used for the zone plate construction

in the MATLAB script, and NEMI atom optical parameters used in this thesis are summarized in tab. (5.1)

Table 5.1: Table shows the NEMI optical parameters, parameters used in the MATLAB code and characteristic parameters for the zone plate used for the further works in this thesis. CB_{ZP} size of the central block, d_{ZP} zone plate diameter, dr_I theoretical width of the outermost zone, dr_M theoretical width of the innermost zone (with center blocking), $\#zones$ total number of zones, r_{step} distance between polygons path that forming the zones, m_{step} the step size of the e-Line system, *Working-area* the size of the total exposure area, g object distance, b image distance, f zone plate focal length and $\lambda_{He_{LN}}$ liquid nitrogen cooled He-beam de Broglie wavelength.

Zone plate 1		**Zone plate 2**	
CB_{ZP}	= 20 µm	CB_{ZP}	= 50 µm
d_{ZP}	= 192 µm	d_{ZP}	= 192 µm
dr_I	= 0.822 µm	dr_I	= 0.329 µm
dr_M	= 0.086 µm	dr_M	= 0.086 µm
$\#zones$	= 554	$\#zones$	= 522
r_{step}	= 0.012 µm	r_{step}	= 0.012 µm
m_{step}	= 0.002 µm	m_{step}	= 0.002 µm
Working-area	= 1000 µm	*Working-area*	= 1000 µm
$g = 935$ mm			
$b = 205$ mm			
$f = 168.14$ mm			
$\lambda_{He_{LN}} = 0.9782$ Å			

The number polygon elements used for forming each circular zone, $\#P$, is dependent on the ratio of the width of the mth zone, dr_m, and r_{step} and calculated as:

$$\#P = \left\lceil \frac{dr_m}{r_{step}} \right\rceil \tag{5.3}$$

The value $\#P$ had to be rounded up or down (e.g., using ceiling or floor function) since the distance between the polygon elements must be equal. As expressed in eq. (5.3), it was chosen to be the least integer greater than or equal to the ratio value. Consequently, some of the zones were slightly smaller than expected. This complication was solved by adding an additional exposure dose (referred to as dose-addition) to those zones, leading to the zones being slightly overexposed. The value of dose-addition depended on the difference between the rounded and the actual value. As a result, the width of the zones with dose-addition was slightly increased. That being said, the accurate value of zone width increment was difficult to determine, as

this was a consequence of proximity effect, which again depended on the amount of the dose-addition and pattern density. The dose-addition value was determined based on the results from the exposure dose investigations, which will be described in section (5.5.1). The concept of dose-addition is illustrated in fig. (5.4). As seen from the different colors of the zones in the design, some of the zones have different exposure dose values. On the very left side of the color spectrum in the figure, the color (the darkest blue) corresponds to 100 % of the reference dose, and $\#P$ of those zones have not been rounded down. On the other hand, the zones with other colors indicate that an additional dose has been applied. For the case in the figure, the maximum additional dose is 110 % of the reference dose (the color furthest to the right side of the spectrum).

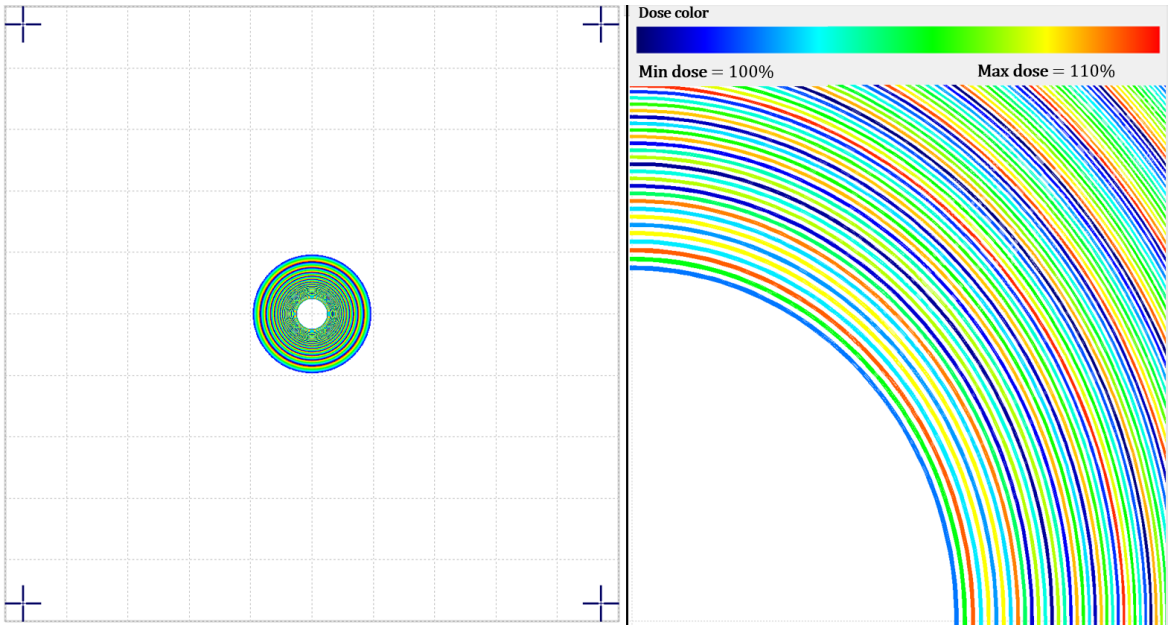

Figure 5.4: The figure shows the zone plate 2 structure design used for the cold helium beam. The left image shows the whole working-area of the GDSII-file with alignment marks (crosses in each corner). On the right is aa closer image of the innermost zones. The color difference indicates the dose variation.

5.2.3 Alignment mark

In addition to zone plate and support bar structures, alignment marks were also patterned. As shown in fig. (5.3) and (5.4), the alignment marks are located at in edges of the working-area. The alignment marks were necessary in order to accurately position the zone plate structure on top of the support structure, referred to as *overlay*, as these were exposed in two separate exposure steps. The alignment marks enable the opportunity to perform the overlay procedure with a so-called 3-points adjustment. A procedure that refers to the transformation of the coordinates in Raith software (see

chapter 2.4 in [57] for more detail about the procedure). The Si_3N_4 membrane made it difficult to detect any structure in the window with SEM. Therefore, it was desired to position these marks outside the membrane windows.

5.3 Selection and optimization of multilayer stack parameters

The thickness and other material properties of the multilayer stack (i.e., resist, etching mask, conductive layer) can affect the fabrication results to a large extent. The thickness of the resist is important for the resolution of the EBL and in order to obtain a desirable structure profile, which is essential for the lift-off process. The thickness and properties of the multilayers stack are crucial for the etch duration and etch rate estimation, and also if they are suitable with the initial etch recipes. Hence, these parameters were determined carefully and in terms of what is suitable for the fabrication method used in this thesis.

5.3.1 Electron beam resist layer

The electron beam resist used in this thesis was a poly-methyl-meth-acrylate (PMMA), 950 K PMMA (AR-P 672 series), produced by Allresist. 950 K refers to the molecular weight of the polymer chain. PMMA was used as a positive tone resist. It is possible to use it as a negative tone, but this requires a significantly higher exposure dose than what is used in this thesis work. A positive tone resist means the exposed area becomes solvable in the development process. After the resist is exposed to the e-beam, the polymer chain in the resist is scissored, resulting in the exposed area being more dissolvable than the unexposed area (fig. (5.5)). The choice of 950K PMMA was driven by the fact that PMMA is one of the most widely used positive tone resist, and mainly due to the very high resolution (achievable linewidths of dimension less than 10 nm) [58]. UiB nanophysics group also has a lot of experience with PMMA [14, 25, 28, 59] and has achieved patterning result with dimension below 50 nm with the resist [59].

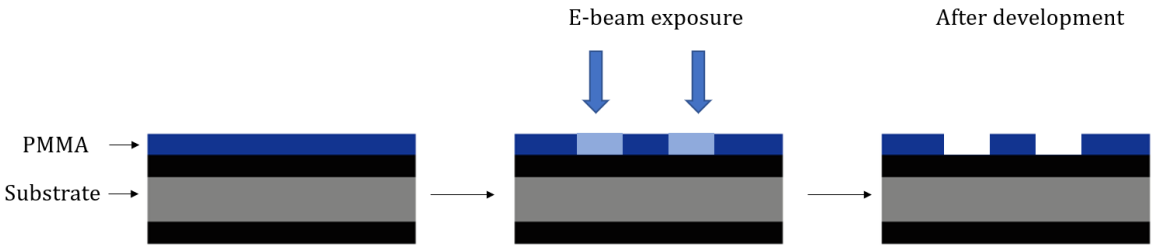

Figure 5.5: The figure illustrates the principle of using positive tone PMMA.

Resist characteristics called *contrast* and *sensitivity* are the primary characterisation factors to be taken into consideration when choosing any resist. Contrast describes the property of the resist to differentiate between exposed and unexposed areas. This is in turn coupled with sensitivity, which refers to the dose required to remove the resist after development entirely. Based on [60], the PMMA used in this thesis has a contrast of 7 and a sensitivity of approximately 300 $\mu C/cm^2$ for area element and 250 pC/cm for line element (for 30 kV e-beam). Both contrast and sensitivity of this PMMA are suitable for the high aspect patterning process, which was important for patterning the zone plate structure. High contrast and sensitivity are often desirable as high contrast can improve the side-wall profile of the resist layer, and a high aspect-ratio structure can be obtained. The main advantage of high resist sensitivity is less required exposure dose, hence minimizing the total exposure time. However, the shot noise in the electron beam is a point of concern in the case of high resist sensitivity. The consequence of the shot noise often degrades line edge roughness and negatively affects the resolution. Some of the fabricated zone plates in this thesis suffered from poor line edge roughness, as will be discussed and presented in section (6.2).

Moreover, the required thickness of the resist layer can be achieved by varying the speed of the coating-spin or the solid content of the resist (amount of the resist in the solution). A thin layer of the PMMA was desirable for the zone plate structure base on the work [24], and because the resolution of the outermost zones improves with decreasing PMMA thickness. A thin PMMA layer ($\sim$ 65 nm) for the zone plate exposure can be achieved from PMMA AR-P 672.02 at 5000 rpm for 60 seconds [60]. On the other hand, the dimension of the smallest feature in the support structure is about four times larger than in the zone plate structure, and the nickel lift-off process benefited from the undercut (more information about the lift-off process and undercut structure will be provided), it was desired to have a thicker PMMA layer for the support structure. A thicker PMMA AR-P 672.8 layer ($\sim$ 130 nm) can be achieved by spin-coating the PMMA at 4000 rpm for 60 seconds [60].

It should be noted that the resist was from 2016 and has a shelf-life of 2 years by the manufacturer. However, many papers suggest that it does not affect the PMMA quality [61, 62], and the author did not see any degrading effect. It is also important to mention that a countless number of repeatably opening the resist bottle could have resulted in some evaporation of the solvent. Consequently, the viscosity of the resist might increase, resulting in a thicker film.

5.3.2 Etching mask

As the support and zone plate structures were written separately to improve the quality of the pattern exposure, the structures needed to be overlaid. Furthermore, PMMA is known to exhibit a low etch resistance in fluorine-based RIE-process [63], and therefore needed to be taken into consideration during the Si_3N_4-etch. One approach to this challenge was to increase the PMMA thickness. However, because of a degrading patterning resolution (mainly due to the broadening of the e-beam spot and hence low ability to deposit the e-beam uniformly at different depths), it was considered not to be an optimal approach. Therefore, it was chosen to transfer the exposed structure to other layers, which then served as an etching mask during the Si_3N_4-etch. Based on the works from [24, 27, 64], it was decided to use an anti-reflective polymer layer (XHIRC-11 from Brewster Science, ARC) followed by a thin layer of SiO_2 for this purpose.

The exposed zone plate structure was transferred to the SiO_2-layer, which was chosen to be approximately 20 nm thick, and served as a hard-mask under the ARC-etch. This step was necessary because PMMA does not withstand ARC-etch and a thin layer of SiO_2 could provide a significant reduction of backscattered electrons under e-beam exposure [28]. Consequently, the proximity effect was reduced, which was an advantage, particularly for high-density structures.

The result of SiO_2-etch was a structured ARC-layer, which further was used as an etch mask under Si_3N_4-etch. With that being said, the ARC polymer has not been used for the anti-reflective purpose but for the fact that ARC polymer cross-links after baking it at 150°C, which in turn gives it a high dry etch resistance compared to other polymers (e.g., PMMA). Additionally, ARC polymer tends to etch at approximately the same rate as Si_3N_4 membrane in CF4 [28]. Hence, the ARC film thickness aspect ratio could be transferred to the Si_3N_4 membrane, and consequently, the pattern in the following anisotropic dry-etch.

The ARC-layer was chosen to be around 300-350 nm thick. Work with 150 nm ARC thick has, however, been done in [28], but the final result showed a significant rounding

effect of the structure. The rounding effect was a cause of the ARC-layer being etched prematurely. It should be mentioned that since pattern transfer to the Si_3N_4 membrane was highly dependent on the ARC-layer, the actual thickness of the ARC-layer was investigated in detail using the methods described in section (4.2).

5.3.3 Conductivity layer

Charge dissipating is generally a frequent problem for insulating substrates during exposure of electron beam resist, resulting in a significant distortion during the patterning [53]. Due to that reason, a thin layer of chrome (approximately 3-4 nm thick) was deposited on top of the PMMA layer. The choice of chrome was based on the fact that the chrome is a superior conductor compared with, for instance, germanium. Additionally, chrome etchant needed to subsequently remove the chrome film before developing the resist has proved not to affect the PMMA layer [28].

5.4 Membrane chip preparation

The membrane material used in this thesis was a 200 nm thick low-stress silicon nitride (Si_3N_4) ordered from MicroChemicals or Si-Mat Silicon Materials. The choice of the membrane material and thickness was chosen based on the works in [27] and that the membrane material properties were suitable for the work in this thesis. The stress in the Si_3N_4 membrane can be tuned by altering the stoichiometry [24]. Having a low-stress is of critical importance as it prevents the membrane from breaking during the RIE under the patterning transfer steps. The membrane thickness also has an essential role. Too thick is problematic with respect to fabrication, and too thin may reduce the stability of the final structures (based on the experience from the works at the UiB nanophysics group).

Moreover, the membrane chips for the work in this thesis were fabricated in 2018. The membrane chip refers to a silicon wafer (with a thickness of 525 $\pm$ 25 μm) that is double-sided coated with a 200 nm thick (Si_3N_4) layer. The membrane windows are opened by means of photolithography (chip patterning) followed by a series of etching steps (opens the windows). The chip fabrication procedure is established in the UiB nanophysics group, see e.g. [27, 64] and providing a detailed description of this is beyond this thesis work. The results were membrane chips with nine membrane windows, as illustrated in fig. (5.6). The multiple membrane windows on each membrane chip were to increase the efficiency and the possibility of the window being broken during fabrication processes.

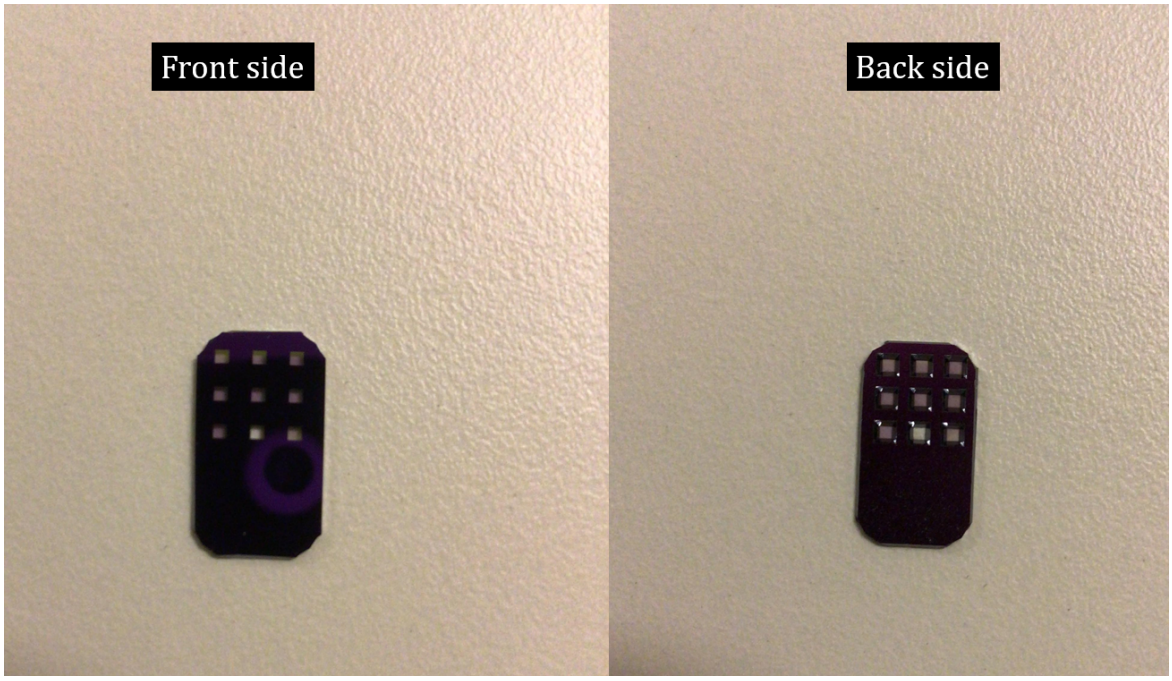

Figure 5.6: The figure illustrates a successfully fabricated free-standing membrane chip. The front (left) and the back (right) sides of the membrane chip consisting of 9 membrane windows.

In order to construct a free-standing membrane, a step of opening the backside of the underlying silicon wafer in the windows was necessary. The mentioned step was done using KOH (potassium-hydroxide) wet-etch. 30% weight percent (ratio between the weight of KOH and the total weight of the solution) of KOH dissolved in DI-water was used. The etching was done by immersing the chips in the solution on top of a hotplate at 80°C and with a glass condenser circulated with cold water to keep the etchant concentration constant. The chips were immersed for approximately 10 hours. It was important that the membrane chips were faced downward (i.e., the opened side faced up) because air bubbles produced on the backside will float up and possibly damage the membrane. KOH wet-etch parameters are summarized in tab. (5.2) and the setup is illustrated in fig. (5.7).

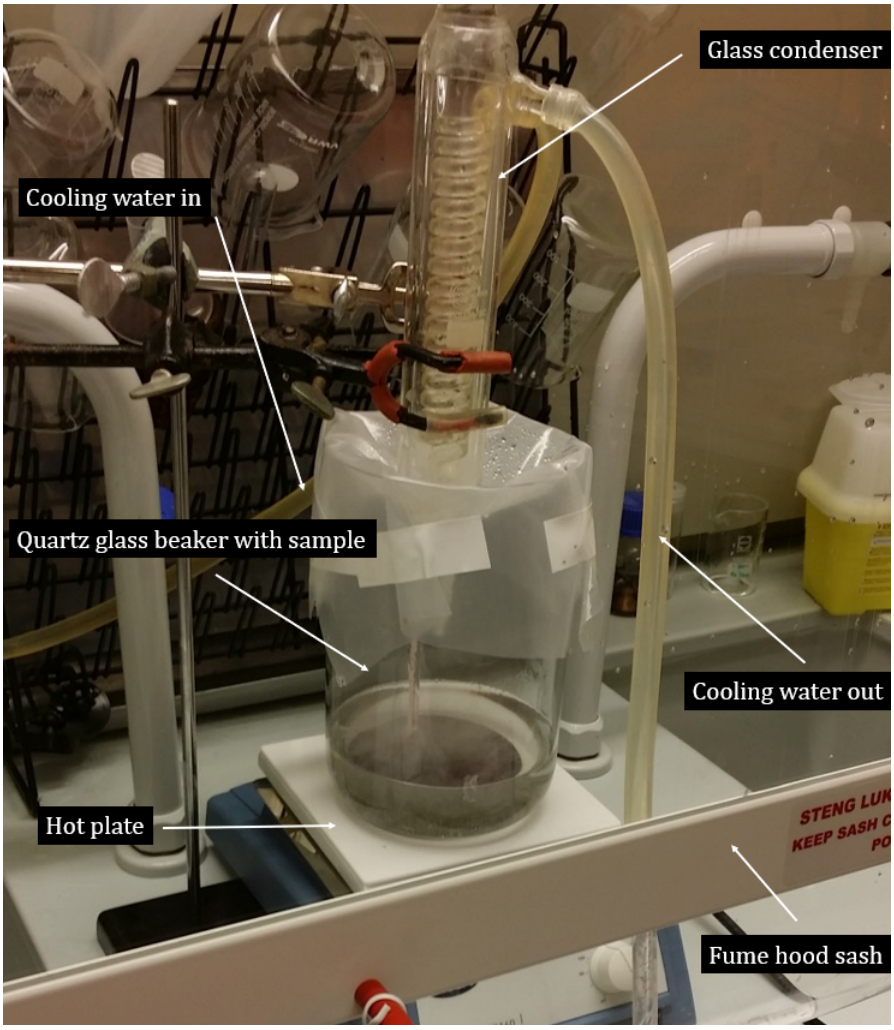

Figure 5.7: Photography of the setup used for the KOH wet-etch to construct free-standing membrane chips. The etching process is carried out in a quartz glass beaker on a hot plate. A Glass condenser and water cooling pipes are used to maintain the concentration of the etching solution. The process is performed inside a fume hood for the safeness.

The KOH wet-etch on crystalline silicon {100} resulted in a partially anisotropic profile. This was the consequence of directional dependence of the etch rate. KOH etches silicon in the direction ⟨100⟩ at a higher rate than ⟨111⟩, hence, an angle of 54.7° between the {100} and {111} silicon planes was formed [64].

After the KOH etch process, the membrane chips contained a large amount of particle contamination. Therefore, the membrane chips required proper cleaning. The cleaning step was done by RCA clean with the recipe described in appendix G in [64]. 60 ml of 28 % hydrogen peroxide (H_2O_2) diluted in 300 ml DI-water. The solution was heated on a hotplate until the temperature reached 70°C. The followed step was to remove the beaker with the solution from the hotplate and add 60 ml of 31% ammonium hydroxide (NH_4OH). The etched membrane chips were immersed in the solution for

30 minutes. Upon completion, the chips were transferred to another beaker with DI-water and left in the beaker for 5 minutes rinsing. Parameters used during the RCA cleaning are summarized in tab. (5.2). Fig. (5.8) illustrates the free-standing Si_3N_4 membrane with deposited multilayer stack.

Table 5.2: Parameters for KOH wet-etch and RCA clean. The parameters are from the works in [27, 64].

	KOH wet-etch	**RCA-clean**
Solution	30% wt. with DI-water	60 ml of 28 % H_2O_2 300 ml DI-water 60 ml of 31% NH_4OH
Duration	9 h	30 min
Temperature	80 °C	70 °C
Clean	Rising with DI-water	Immerse in a beaker with DI-water for 5 min.

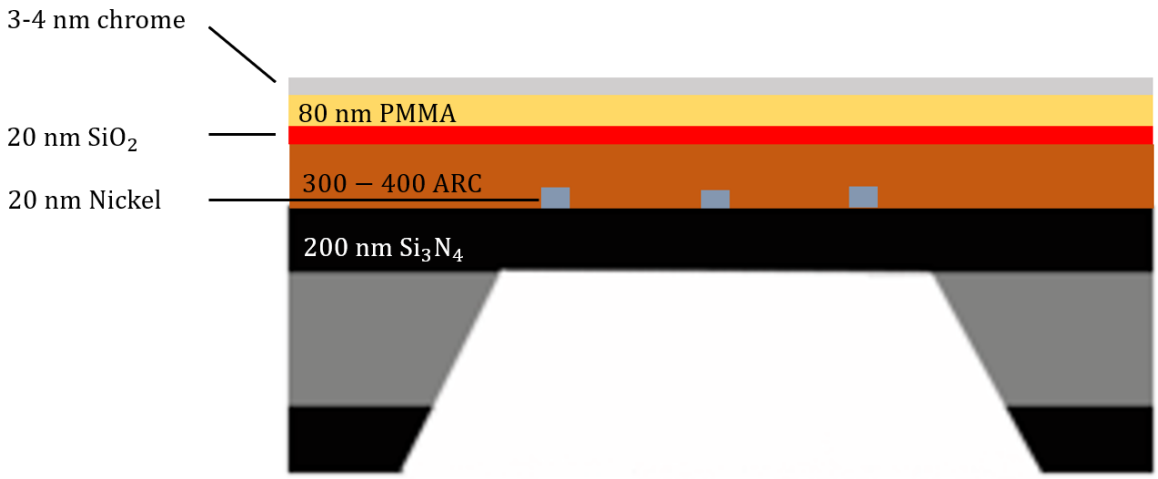

Figure 5.8: The figure illustrates the stack of layers used in this thesis for the pattern transferring of the zone plate structure. Nickel shows the support structure already patterned.

5.5 Investigating and choosing e-beam exposure parameters

In order to achieve high-quality EBL patterning results, optimization of the exposure parameters, including exposure dose, step size, acceleration voltage, and aperture size, is of critical importance. This is mainly due to the concern of proximity effect, over-or underexposure, as well as e-beam spot overlapping, as mentioned in section

(3.1). Moreover, optimizing the exposure parameters is important in order to ensure a completely dissolved structure and obtain the designed patterns.

5.5.1 Exposure dose

The exposure dose's value was considered one of the most important parameters to achieve the best patterning result, especially for dense and high-resolution structures such as the zone plate.

The optimum exposure dose for zone plate and support bar structure was determined by test patterning the structures on the actual membrane chip. Using the actual free-standing membrane chip is important as the underlying substrate can alter the exposure characteristics (e.g., the level of electron backscattering and consequently the proximity effect in the resist will be affected if the Si_3N_4 membrane is still on silicon or suspended in a vacuum). The dose was varied between 50 % to 200 % of the reference dose (set to 300 uC/cm^2 for area element, and 250 pC/cm for line element). In order to reduce total written time, only half of the structures were patterned.

The next step was to develop the sample and investigate the patterning results with SEM as described in section (4.1.1). The optimum exposure dose for the zone plate was determined based on the dose value that completely dissolved the exposed areas and gave the zone widths that agree with the theoretical values. The optimum value for the support bar structure was based on the dose that gave the best result of the nickel lift-off process (i.e., successfully lift-off process and 450 nm width of the support bars). The dose of the alignment marks was considered less important than the others because the achieved dimension of the alignment marks was not crucial. However, the alignment marks needed to be completely dissolved after the development and the lift-off processes.

5.5.2 Step size

As mentioned in section (3.1), the value of the step size should be approximately 50% of the e-beam spot size. In practice, it was not possible to estimate the value of the e-beam spot with high enough precision. For that reason, the step size value was determined using a similar method presented in section (5.5.1). Instead of varying exposure dose, the value of step size was varied. Step size value was determined based on the patterned results investigated using SEM.

5.5.3 Acceleration voltage and aperture size

The acceleration voltage and size of the EBL-system aperture had essential roles mainly due to the e-beam spot size and the e-beam current limitation. As previously explained, the patterning results of the low acceleration voltage EBL are limited by the e-beam broadening. Thus, it was desirable to perform EBL with the maximum acceleration voltage of the e-Line instrument (which is 30 kV) to achieve the highest possible e-beam spot size.

For the aperture size, the larger the aperture, the higher the e-beam current and speed. Thus, a too large aperture could result in the beam speed exceeding Raith's recommended value (10 mm/s). Excessively high beam speed can lead to pattern artifacts, and imprecisions [41]. Based on the previous work at the UiB nanophysics group, the smallest possible aperture is often the best choice when using high-sensitivity resist as it limits the beam speed and increases the probability of sufficient energy transfer of the electron. Even though the disadvantage is a longer exposure time which could e.g., affects the write-fields stitching accuracy due to a drift in e-beam position over time.

5.6 Investigating of etch parameter

Optimizing etching parameters and finding the etch rate of the different layers were important to achieve the best possible result of the pattern transfer (i.e. to obtain high anisotropic etch profile and high aspect ratio structure in the Si_3N_4 membrane). Here, the etch parameters refer to the parameters in the reactive ion etcher, Plasmatherm 790+, including gas flow, chamber pressure, RF-power, etch duration, and gas composition. The initial etch recipe of SiO_2, ARC and Si_3N_4 layers are from the works in [27, 28], and are presented in tab. [5.3].

Table 5.3: Initial etch parameters were used for the investigation. The parameters are from the works in [27, 28].

Etch	**SiO_2**	**ARC**	**Si_3N_4**
Chamber pressure [mTorr]	10	7	10
RF power [W]	100	200	100
Gas composition	CHF_3	He & O_2	CF_4
Flow [sccm]	15	10 & 5	15
Etch-duration [min]	3.5	8	9 + 15 = 24
Estimated etch rate [nm/min]	-	37	8 - 10

The membrane chip was deposited with the mask layers and PMMA (AR-P 672.02 spin coated with same settings as for the zone plate exposure. More details will be provided) for the investigation. The test structures were exposed across (in the longest direction) the membrane chip. The test structures consisted of four 10 mm long lines with different widths, 80 nm, 150 nm, 200 nm, and 450 nm. The initial attempts used the same recipe as presented in tab. (5.3). First, the SiO_2-etch was investigated following by ARC-etch, and lastly Si_3N_4-etch. In order to determine the etch rate, it was important not to etch all the way through. The results of each etch step were investigated by cleaving the chip and imaging the cross-section using 45° and 90° tilting as described in section (4.1.2). However, it is important to mention that it was difficult to obtain a cross-section image of the free-standing membrane due to the difficulty of cleaving the membrane window in half without breaking it. Instead, the cross-section of the area outside the window was investigated. Consequently, the image of etching results might not perfectly correspond to the results on the free-standing membrane itself. This is because the backside of the window is open, meaning less heat accumulation and that the membrane can, in theory, be etched from both sides.

5.7 Process details of the final free-standing Fresnel zone plate fabrication

After several series of layer thickness, exposure parameters, and etch parameters investigations, the last part of the work in this thesis was to fabricate the zone plates on free-standing Si_3N_4 membrane. As mentioned, two different zone plate structures were exposed (Zone plate 1: 20 μm in diameter central blocking. Zone plate 2: 50 μm in diameter central blocking). The works in the final fabrication process were done using the parameters from the investigations (presented in section (6.1)).

5.7.1 Sample preparation and spin-coating resist layer for support bar structure

The prior step before the coating process was to clean the samples with acetone, methanol, and isopropanol (IPA) for 10 seconds each, followed by pressurized nitrogen (N_2) drying. For the coating of the resist layer, a spin-coater was used. The samples were attached to a silicon wafer with double-sided tape. The coating process was performed on a silicon wafer because the vacuum chuck normally used to hold the sample in place during the spin-coating process would have ruptured the free-standing membranes and because the samples were too small in order to get a proper vacuum. The subsequent step was to soft-bake the samples at 175° C on a hotplate for 5 minutes

and thereafter cool at room temperature prior to further use. This subsequent step was necessary to dry and evaporate the residual solvent and solidify the layer, resulting in the resist being more resistant to the solvent in the development step. The resist spin-coating parameters for support structure are summarized in tab. (5.4)

Table 5.4: Parameters for the spin-coating and soft-baking of electron sensitive resist PMMA for support bar structure. The measured thickness is the result from the investigation.

Resist spin-coating	
Solution	950 K PMMA AR-P 672.03
Pre-spin	350 rpm for 60 sec
Main-spin	4000 rpm for 60 sec
Soft-baking	5 min at 175°C
Measured thickness	153 ± 5 nm

5.7.2 Expose and development of support structure

Exposure of the support bar structure was performed using the parameters from the investigations in section (5.5). The e-beam exposure parameters are summarized in tab. (5.5). The detailed procedure of the EBL using Raith e-Line, see [65].

Table 5.5: Optimized parameters used for the exposure of the support bar structure.

Exposure of support structure	
Acceleration voltage (AV)	30 kV
Collimating Aperture	10 um
E-beam current (I_{beam})	0.035 nA
Area dose	420 ± 10 uC/cm^2
Line dose	350 ± 10 pC/cm
Dwell time (τ)	0.009 ms (line), 0.01 ms (area)
Beam speed	1.4 mm/s (line), 0.7 mm/s (area)
Step size	12 nm
Write-field	100 um
Working distance (WD)	≈ 10.5 - 10.6 mm

The subsequent step after the e-beam exposure was development. This step refers to immersing the sample in a developer, AR 600-56 (the main component of the solution is methyl 2-methylpropyl ketonem, MIBK) at 19° for 60 seconds, followed by a rinsing step with IPA and dried using pressurized nitrogen. The parameters used for this subsequent step are presented in tab. (5.6).

Table 5.6: Parameters used for the development procedure.

Development	
Solution	AR 600-56
Duration	60 sec
Stopper	Rinsing with IPA for 30 sec
Dry	Air dry with pressurized nitrogen

5.7.3 Nickel deposition and lift off

Moreover, a hard-mask of the support structure was created on the thin membrane layer. The hard-mask was necessary in order to transfer the support structure together with the zone plate structure onto the membrane under the Si_3N_4-etch. A hard-mask was created by first depositing 20 nm of nickel on top of the sample using EBE (Termescal FC-2000). The choice of nickel was based on the fact that nickel does not etch in CF4 plasma, and nickel does not suffer from different types of stresses that are created during and after film deposition in this application [24, 66].

The next step was to perform a nickel lift-off process to remove the PMMA and residual nickel. This subsequent step was done by immersing the sample in1-Methyl-2-pyrrolidone (NMP). The NMP was heated on a hot plate at 80 °C to increase the interaction and speed up the lift-off process. The sample was left in NMP for longer than 45 minutes to ensure the lift-off was successfully done. The following step was to rinse the sample with acetone, methanol, and IPA for 30 seconds each. The immersion duration could be decreased using ultrasonic agitation. However, it was avoided here since it could potentially damage the membrane. The final result was a hard-mask in the areas where the support structure was exposed, as illustrated in fig. (5.9). The parameters used for nickel deposition and lift-off are summarized in tab. (5.7).

It is worth noting that the lift-off process can benefit from a good undercut profile that can be achieved by several methods. The term line slope (i.e., the angle between the exposed resist sidewall and the underlying substrate) is used to understand what undercut is. When the line slope is less than 90°, an undercut structure is obtained (illustrated in fig. (5.9)). A good undercut profile is desirable to obtain clean lift-off because the undercut assures the deposited layer on top of the resist is disconnected from that in contact with the substrate. As previously mentioned, an undercut profile can be achieved by using a thick resist layer, which is one of the reasons the resist layer for the support bar structure was thicker than for the zone plate structure. Other methods to obtain undercut are, for instance, low energy e-beam exposure or by using several layers resist (with the low molecular-weight form on the bottom) [67].

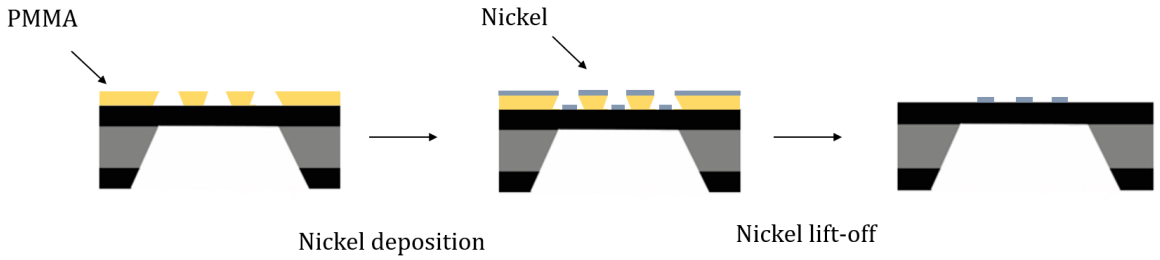

Figure 5.9: The figure illustrates an example of the lift-off process. Notice that the pattern is inverted after the lift-off. Figure also illustrates undercut structure that is suitable for the deposition and lift-off process.

Table 5.7: Parameters used for nickel deposition and the subsequent lift-off process.

Nickel deposition	
Material	Nickel
Deposition rate	0.3 nm/s
Estimated thickness	20 nm
Lift-off	
Solution	NMP
Temperature	80°C
Duration	$>$ 45 min
Stopper	Acetone, methanol and IPA for 30 sec each

5.7.4 Applying layers stack

As previously mentioned, an approximate 300-350 nm layer of anti-reflective coating (ARC) and 20 nm of SiO_2 were used as an etching mask. Lastly, a 3-4 nm thin chrome layer on top of the PMMA layer was considered for the charge dissipating layer during the e-beam exposure. It is important to mention that the ARC-layer was spin-coated in two steps, as it was not possible to achieve the desired thickness even with the lowest spin speed setting. The layers were deposited using the following procedures, and the parameters are summarized in tab. (5.8):

i. ARC (Brewster Science, XHIRC-11) was spin-coated onto the front side of the membrane chip using a spin-coating with the same procedures and pre-spin setting as PMMA coating in section (5.7.1). The main-spin was set to 4000 rpm for 60 seconds.

ii. The sample was soft-baked on a hotplate at 150° for 3 minutes.

iii. Step i. was repeated.

iv. The sample was soft-baked on a hotplate at 150° for 5 minutes.

v. 20 nm of SiO_2 was deposited at a rate of 0.3 nm/s using EBE.

vi. PMMA (950 K PMMA AR-P 672.02) was spin-coated on top of SiO_2-layer with same procedure as described in section (5.7.1). The main-spin was set to 5000 rpm for 60 seconds.

vii. The sample was soft-baked at 175° Celsius for 5 minutes

viii. Lastly, 4 nm chrome layer was deposited on top at a rate of 0.2 nm/s using EBE.

Table 5.8: Parameters for spin-coating and depositing layers stack used in this thesis. The values of the measured thickness are the results from the investigations. Estimated thicknesses of the deposited layers are based on the Termascal settings for SiO_2 and Cr. *ARC was spin-coated twice with the same spin settings but different soft-baking duration.

Spin-coating	**ARC***	**PMMA (Zone plate)**
Solution	Brewer Science XHRIC-11	950 K PMMA AR-P 672.02
Pre-spin	350 rpm for 10 sec	350 rpm for 10 sec
Main-spin	4000 rpm for 60 sec	5000 rpm for 60 sec
Soft-baking	3 min + 5 min at 150°C	5 min at 175°C
Measured thickness	330 ± 10 nm	87 ± 5 nm
Deposition	**SiO_2**	**Chromium (Cr)**
Deposition rate	0.3 nm/s	0.2 nm/s
Estimate thickness	20 nm	3 nm

5.7.5 Expose and develop zone plate structure

After the layers were deposited, the next step was to expose the zone plate structure using Raith e-Line. The exposure was done mostly with the same procedure for the support bar structure as described in section (5.7.2). An additional step, so-called three-point alignment, was introduced for the zone plate exposure. This step was necessary for the overlaying of the structures. The exposure parameters used in this process are shown in tab. (5.9).

Table 5.9: Optimized parameters used for the exposure of the zone plate structure.

Exposure of zone plate structure	
Accerelation voltage (AV)	30 kV
Collimating Aperture	7.5 um
E-beam current (I_{beam})	$\approx$ 0.014 nA
Area dose	330 $\pm$ 10 uC/cm^2
Line dose	275 $\pm$ 10 pC/cm
Dwell time (τ)	0.013 ms (line), 0.013 ms (area)
Beam speed	0.61 mm/s (line), 0.63 mm/s (area)
Step size	8 nm
Write-field	100 um
Working distance (WD)	$\approx$ 10.5 - 10.7 mm

After the zone plate structure was successfully exposed, the layer of chromium was removed using a chromium etchant (Transene Company Inc., Chromium etchant 1020). The sample was immersed in the etchant for 10 seconds at room temperature ($\approx$ 20°C). The subsequent step was to develop the exposed area, which was done using the same parameters and procedures in section (5.7.2).

5.7.6 Pattern transferring

After a successful development step, the underlying of SiO_2 was left exposed. Three steps of RIE were performed (using Plasmatherm 790+) to transfer the zone plate and the support structures to Si_3N_4 membrane. The etch parameters used in these three RIE steps were based on the results of investigations in section (5.6).

1: Pattern transfer to SiO_2 (SiO_2-etch)

The SiO_2-layer was etched using the same recipe as the works by Martin Greve in [28]. During the etch process, the layer of PMMA served as an etch mask. The SiO_2-layer was etched using CHF_3 gas, and the etch duration was 3 minutes and 30 seconds at 10 mTorr and RF power of 100 W. The choice of CHF_3 gas was to obtain relatively high selectivity etch [48].

2: Pattern transfer to ARC (ARC-etch)

The ARC-layer was etched using a gas composition of helium (He) and oxygen (O_2) for 9 minutes at 10 mTorr and 200 W. During the ARC-etch, the PMMA was removed, and the SiO_2-layer then served as a hard-mask. Note that this is an increase in etching time relative to the parameters described in [27]. It was found that the thickness of

the ARC varied across the membrane surface and from each coating process, so it was important to be sure that the ARC was completely removed. More information can be found in section (6.1.2).

3: Pattern transfer to to Si_3N_4 (Si_3N_4-etch)

For the final Si_3N_4-etch, CF_4 gas for a duration of 28 minutes at 10 mTorr and 100 W was used. It is important to mention that the total of 28 minutes of etch duration was subdivided into 14 steps of 2 minutes each, yielding 14 cycles. Each cycle consisted of 2 minutes of etching and 2 minutes N_2 flush to cool down the sample. The cyclic RIE process was used due to the fact that long continuous etch resulted in a high plasma temperature which over time would melt the ARC-layer. By letting the sample cool down, the etch rate of the ARC-layer decreases, improving the selectivity between the ARC-layer and Si_3N_4 membrane due to a thermal load [68].

The etch parameters and the estimated etch rate for the mentioned RIE steps are summarized in tab. (5.10).

Table 5.10: The etch-parameters used for patterning transfer in this thesis. *2 minutes N_2 flush in each cycle.

Etch	**SiO_2**	**ARC**	**Si_3N_4**
Chamber pressure [mTorr]	10	10	10
RF power [W]	100	200	100
Gas composition	CHF_3	He & O_2	CF_4
Flow [sccm]	15	10 & 5	15
Etch duration [min]	3.30	9	* 2 $\times$14 cycles = 28
Estimated etch rate [nm/min]	-	41 - 42	7.5 - 8 (Si_3N_4), 12 - 13 (ARC)

Chapter 6

Results and analysis

This chapter presents the results achieved during the course of this thesis. The first part will cover the results from the parameters investigation processes. In the second part, the results and analysis of the final fabrication steps of the 192 nm diameter Fresnel zone plate with 20 µm and 50 µm central blocking are presented. A discussion of the challenges of the final fabrication steps are also included. In summary, the results of the free-standing Fresnel zone plate are shown to be successful.

6.1 Results of the parameters investigations

As mentioned, the investigation of layers thicknesses, exposure parameters, and etching parameters was an essential part of the work in this thesis. Without the investigations and parameters tuning, the results of the final fabrication might not be as good. The thickness of the PMMA layers are especially of interest as the lift-off and the pattern resolution are highly dependent on PMMA thickness. The ARC thickness is essential during the Si_3N_4-etch. The exposure dose is considered one of the most critical parameters in this thesis, as it affects the quality of the exposed structure (e.g., desirable width and the pattern resolution), the results of the lift-off, and the etched structure. Finally, one of the most important parts of the works in this thesis was to ensure that the support bar and the zone plate structure were successfully transferred to the Si_3N_4 membrane. Hence, optimizing the etching parameters was crucial.

6.1.1 PMMA thickness

Tab. (6.1) and (6.2) show the results of the PMMA thickness measurements (using the thin film analyzer) for the support bar and zone plate structure, respectively. In both cases, the investigation was done on three different samples (silicon wafer coated with PMMA).

Table 6.1: The results of the PMMA AR-P 672.03 (spin-coated at 4000 rpm for 1 min) thickness measurement using the thin film analyzer from three different samples.

PMMA AR-P 672.03	**Measured thickness [nm]**		
measurement (n)	**Sample 1**	**Sample 2**	**Sample 3**
1	155.4	152.0	153.1
2	153.8	151.1	154.6
3	154.8	154.6	151.3
4	155.4	151.2	151.7
5	155.3	151.4	152.4
Mean value	154.9	152.1	152.6

Table 6.2: The results of the PMMA AR-P 672.02 (spin-coated at 5000 rpm for 1 min) thickness measurement using the thin film analyzer from three different samples.

PMMA AR-P 672.02	**Measured thickness [nm]**		
measurement (n)	**Sample 1**	**Sample 2**	**Sample 3**
1	88.1	87.1	87.7
2	87.8	87.2	86.8
3	88.4	87.1	86.2
4	87.6	86.5	86.9
5	88.6	88.3	86.4
Mean value	88.1	87.2	86.7

Based on the results above, the achieved thickness of the PMMA layer for support bar structure is estimated to be (153 $\pm$ 5) nm and (87 $\pm$ 5) nm for the zone plate structure. The PMMA layer thicknesses deviate from the expected values from the data-sheet [60]. However, the deviations are expected due to the countless times of repeatedly opening the resist bottle, which can result in some evaporation of the solvent. Nevertheless, the offset is not considered a major problem as the thicknesses are still in the desirable range. Most importantly, the resist seems to be evenly coated on the sample, and no negative effect has been observed on the patterning results.

6.1.2 ARC thickness

The thickness of the ARC-layer was investigated using the thin-film analyzer and SEM as described in section (4.2). Three set of measurements (three different samples) were done using the thin film analyzer, and the results are presented in tab. (6.3).

Table 6.3: The results of the ARC XHRIC-11 (spin-coated at 4000 rpm for 1 min twice) thickness measurement using the thin film analyzer from three different samples. The results show a clear inconsistency of the thickness from each sample to each sample.

ARC XHRIC-11	**Measured thickness [nm]**		
measurement (n)	**Sample 1**	**Sample 2**	**Sample 3**
1	361.1	379.6	370.1
2	361.1	378.5	370.7
3	361.7	377.5	369.4
4	361.3	378.8	370.0
5	361.5	380.0	369.2
Mean value	361.3	378.5	369.9

It can be seen from tab. (6.3) that the ARC thickness varies from each sample. The inconsistency can indicate a poor ARC coating procedure. The results show that the ARC thickness is more than 60 nm thicker than the expected value (based on the [27]). This is suspected to be due to incorrect settings in the thin film analyzer software during the measurement. The thickness of the ARC layer was further investigated using SEM, presented in fig. (6.1a) and (6.1b)).

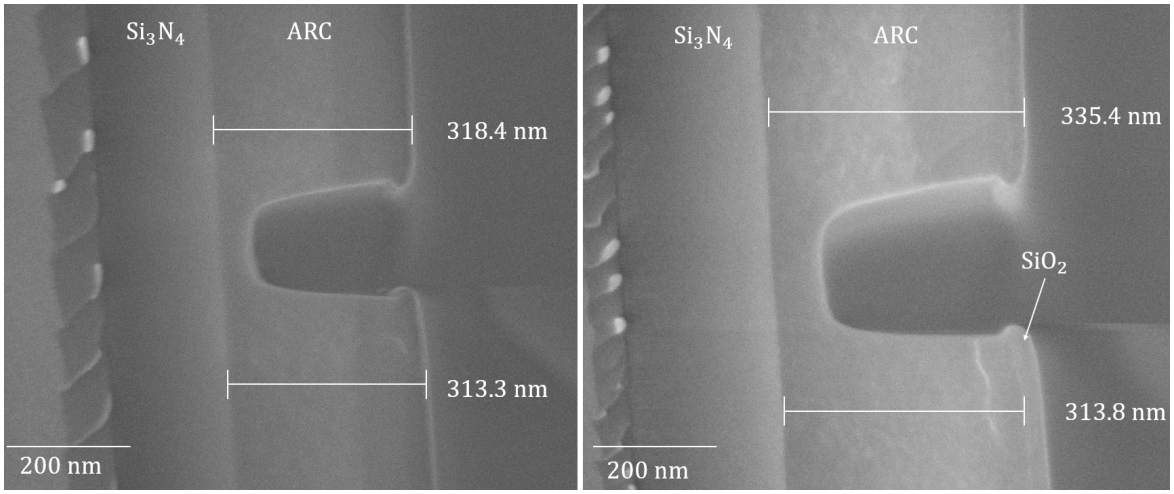

(a) Membrane chip 5 after 3.30 min SiO_2- and 6 min ARC-etch used for the thickness measurement of the ARC-layer.

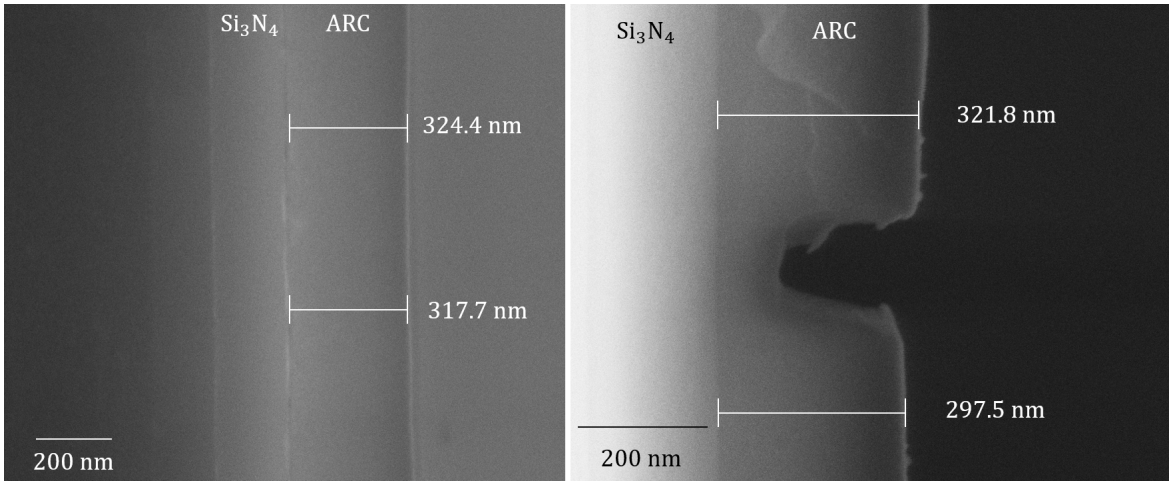

(b) Membrane chip 6 after 3.30 min SiO_2- and 6 min ARC-etch used for the thickness measurement of the ARC-layer.

Figure 6.1: Cross-section SEM images at 90° of two different chips, (a) chip 5 and (b) chip 6. The images were used for the investigation of the ARC thickness using built-in measurement tools and scale-bar.

From fig. (6.1), two different issues can be seen. The first is the inconsistency of the ARC thickness from sample to sample, while the second is the inhomogeneity of the ARC thickness. The author speculates that the latter issue could be explained by the fact that the ARC-layer was spin-coated in two sequences and the consequence of particles or gas bubbles in the applied ARC. Spin-coating on textured substrates either because of particles or ARC is not uniformly coated in the first sequence, the thickness homogeneity of the ARC film will suffer. Worthy to note that the ARC used in this thesis was opened in 2015. Hence, the probability of the ARC solution being expired and containing particles exists. However, no issues were found with the performance of the ARC during the RIE process. Hence, it was chosen to process the further work in the thesis with the same ARC. It is concluded that the two layers of ARC are approximately (330 ± 10) nm thick and that it is difficult to obtain consistent ARC thickness and a good thickness homogeneity, which need to be taken into consideration during the RIE processes.

6.1.3 Exposure dose and lift-off process

Exposure dose of the zone plate

The optimum exposure dose for the zone plate exposure is based on the results in fig. (6.2). Fig. (6.2a) shows the images of the zone plate structure exposed with 200 pC/cm line dose after development. The images show the variation in the patterning result (due to dose-addition) and that the original designed pattern is not obtained.

Some exposed areas are not successfully dissolved, indicating the exposure dose was insufficient (underexposure). In the case of fig. (6.2b) and (6.2c), the exposed areas appear to be dissolved. However, the innermost and outermost zones in fig. (6.2b) are shown to be wider than the design which can be a consequence of overexposure. Based on the results in fig. (6.2c), the optimum dose is decided to be approximately (275 ± 10) pC/cm, and the additional dose for the zone plate structure was chosen to be 10% of it. With that being said, the innermost zones appear to be more sensitive to the exposure dose, which can be explained by the fact that there are more polygon elements for the zone construction (described in section (5.2)).

Worth mentioning that the circular patterns covering the images in fig. (6.2a) are not the result of unoptimized EBL but are so-called Moiré fringes, a visual artifact that arises from the interference between the zone plate pattern and the pattern of the pixels in the SEM detector in this case [69].

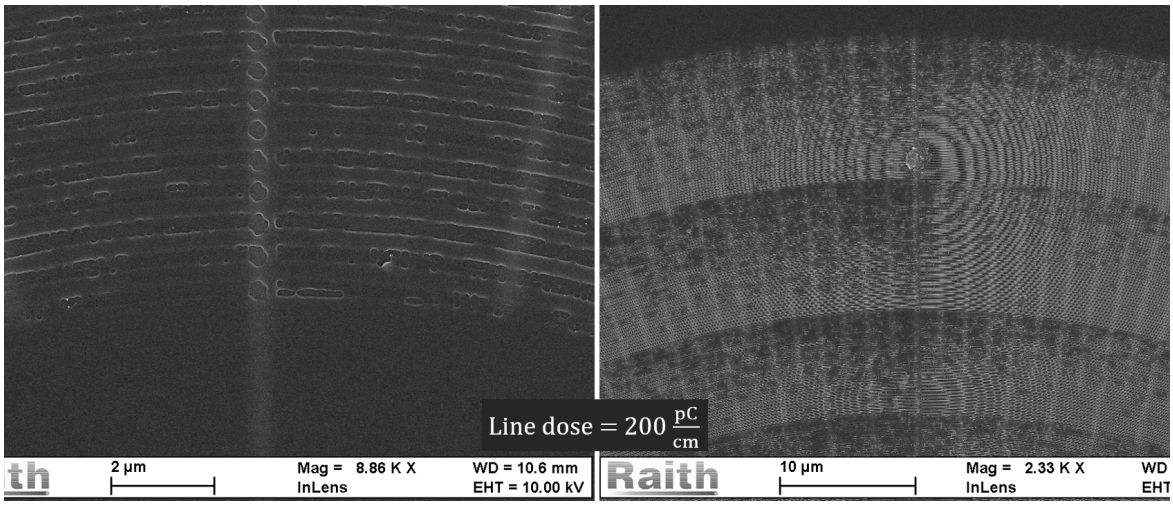

(a) Membrane chip 2 window 5. The image of the innermost zones of an underexposed zone plate structure (left) and a more distant image of the area around the outermost zones (right). Also worth noting the variation in a periodic fashion of the exposed pattern. This is due dose-addition, which results in some of the zones being less underexposed (i.e. the exposed pattern is more presented). Exposure dose = 200 pC/cm.

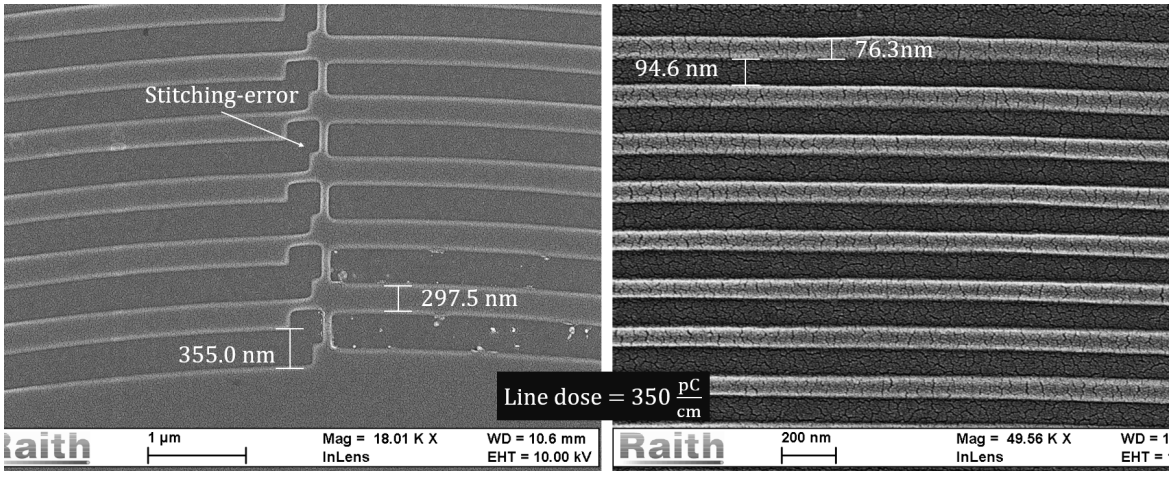

(b) Membrane chip 1 window 5. The image of the innermost zones of an overexposed zone plate structure on the left and the outermost zones on the right. Exposure dose = 350 pC/cm.

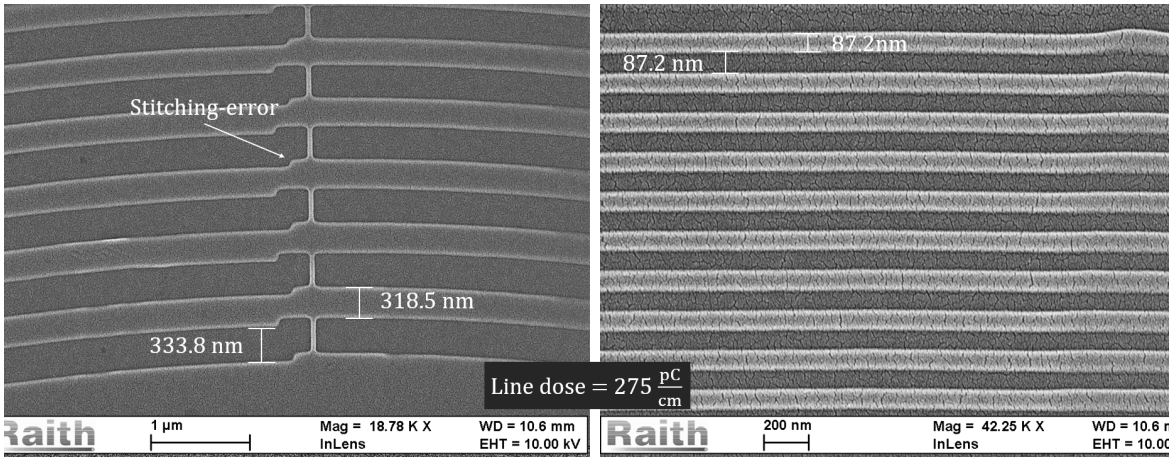

(c) Membrane chip 1 window 6. The image of the innermost zones of the zone plate structure exposed with optimum exposure dose (left), and the outermost zones on the right. Exposure dose = 275 pC/cm.

Figure 6.2: Figures show SEM images of the zone plate 2 pattern exposed with three different exposure line doses. In (a), the dark areas correspond to the unexposed areas, while the exposed areas are brighter. The opposite is for the case of (b) and (c). (a) shows the result of underexposure while (b) and (c) show overexposure and optimum dose, respectively. The membrane chip 1 is coated with AuPd to enhance contrast. Due to the too thick AuPb-layer, cracking of the surface can be seen. Also worth noting the shifting in the pattern in (b) and (c) due to stitching-error, more information will be provided in the next section.

Exposure dose of the support bar

The optimum exposure dose of the support bar structure is determined from the results of nickel lift-off process in fig. (6.3a) and (6.3b). In fig. (a), the support bar structure was exposed with two different exposure dose, 400 pC/cm in window 1, and 250 pC/cm in window 3. As can be seen, the structure in window 1 is enlarged (suspected due to overexposure). In contrast, the lift-off in window 3 is not completely successful, and the bars are narrower than the desired value ($\approx$ 450 nm). The narrower bars and

unsuccessful lift-off are likely a result of underexposure. Underexposure leads to resist residue on the developed areas. Consequently, it can cause the lift-off to fail, either because of the fact that it is more challenging for the solvent to penetrate underneath the metal and create a force for achieving lift-off or because resist residues remain on the surface leading to a complete lift-off (all of the deposited metal is removed).

As shown in fig. (6.3b), a successful lift-off and desirable support bar width is obtained. Hence, the optimum exposure dose of the support bars is approximately (350 ± 10) pC/cm and the lift-off parameters were used for the final fabrication steps.

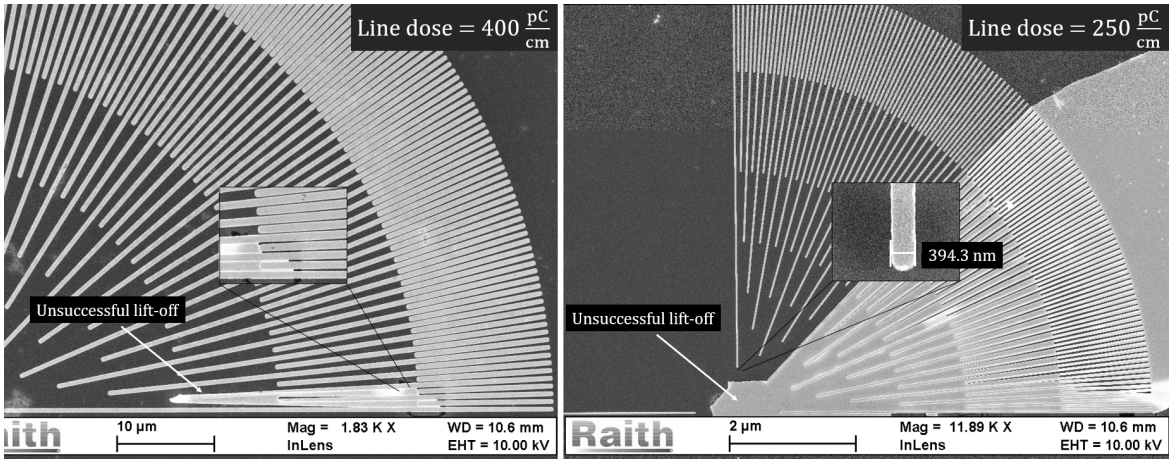

(a) Membrane chip 10 window 1 and 3 after nickel deposition and lift-off. Support bar structure exposed with 400 pC/cm (left) and 250 pC/cm (right). The (left) zoomed in image shows the oversized bars resulting in the structure to be extremely dense. Consequently, the intensity of the transmitted helium beam will be reduced. The (right) zoomed in image illustrating approximately 50 nm narrower bar compared with the design (450 nm).

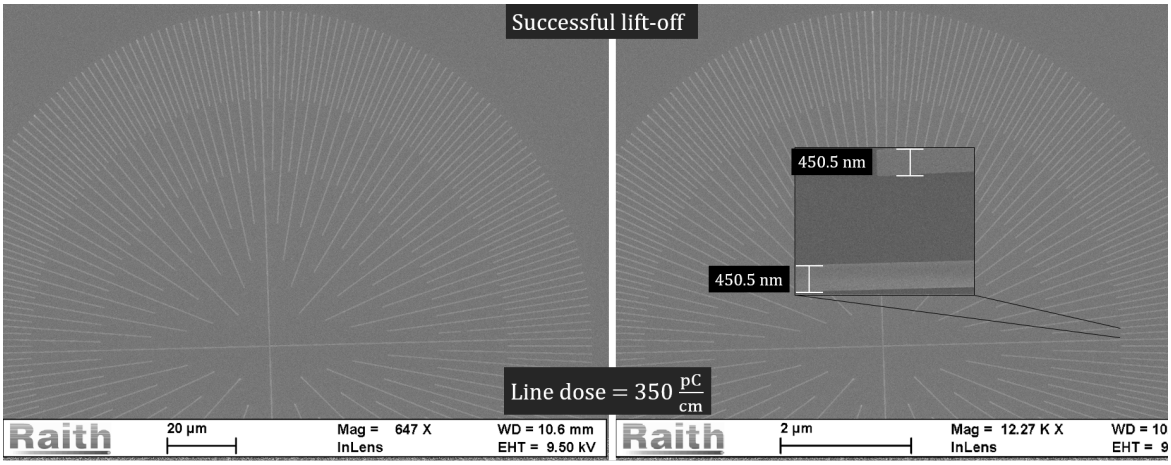

(b) Membrane chip 11 window 3 after nickel deposition and lift-off. Support bar structure exposed with 350 pC/cm. The image shows an unsuccessful lift-off process. The zoomed in image indicates that the width of the bar is narrower than the desired value.

Figure 6.3: Figures show SEM images of the membrane chips 10 and 11 after the lift-off process. (a) shows the results of overexposed structure on the left and underexposed on the right. Unsuccessful nickel lift-off is also presented. (b) shows the results of a successful nickel lift-off and optimum exposure dose.

6.1.4 Etching parameters

Etching of underexposed structure

One of the most important concerns for the etching process is ensuring that the structure is not underexposed and fully developed. This is because the resist residues will have an effect on the etched structures, as illustrated in fig. (6.4).

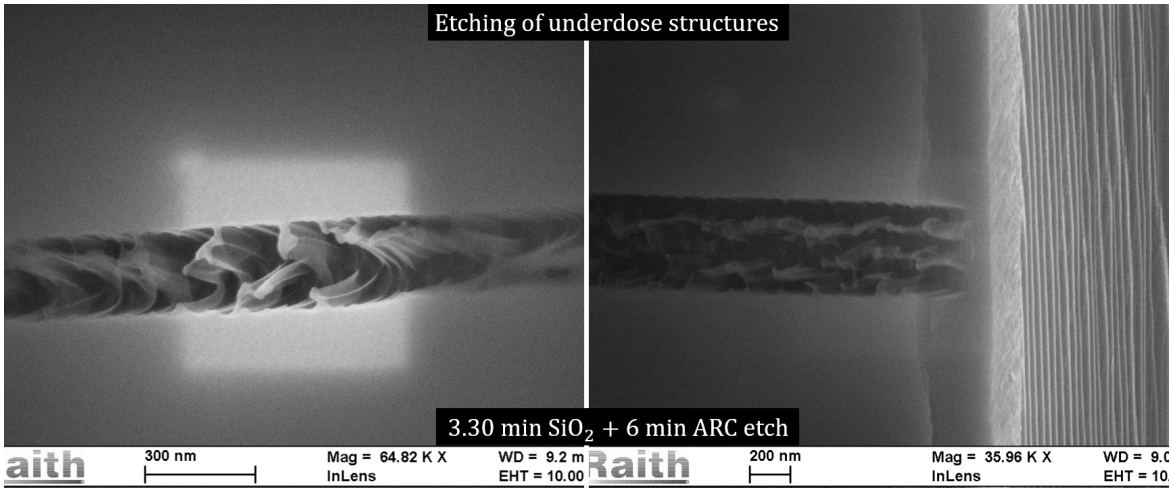

Figure 6.4: SEM images of membrane chip 1 after 3.30 min SiO_2 - and 6 min ARC-etch. Both of the images were taken taken at 45° after cleaving the sample. Left image showing the sample surface, while the right is showing the cross-section. The results show an unsuccessfully etching, suspected due to the structure being underexposed.

SiO_2- and ARC-etch

Due to SiO_2-layer thickness ($\approx$ 20 nm) and the difficulty to obtain high SEM image contrast between the SiO_2- and the ARC-layer, the etch rate of SiO_2-layer is challenging to determine. Thus, it is more convenient to investigate the results of the SiO_2-and the ARC-etch together. The results of 3.30 min SiO_2- and 6 min ARC-etch are shown in fig. (6.5a), (6.5b) and (6.5c) and are used for the further investigation.

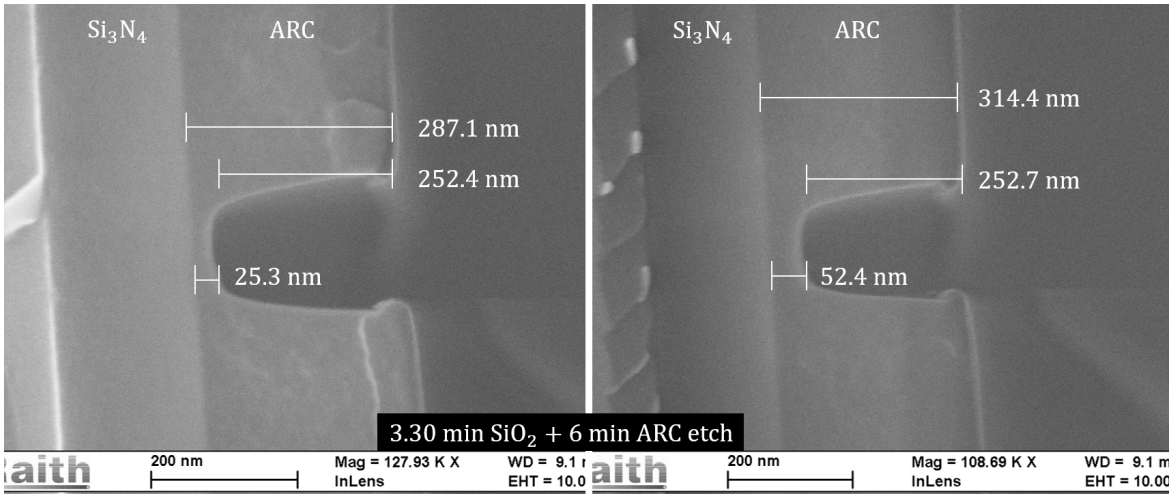

(a) Cross-section investigation at 90°.

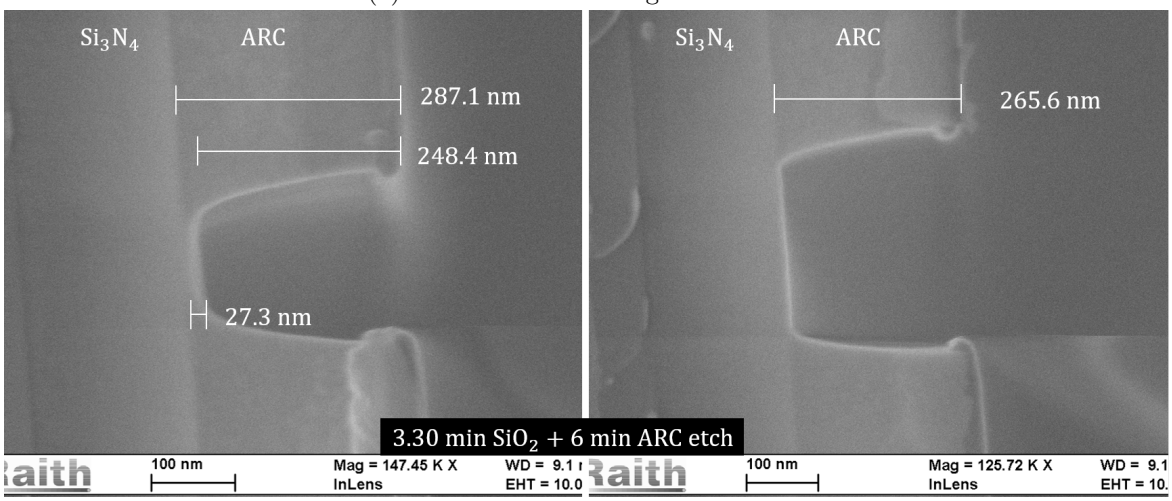

(b) Cross-section investigation at 90°.

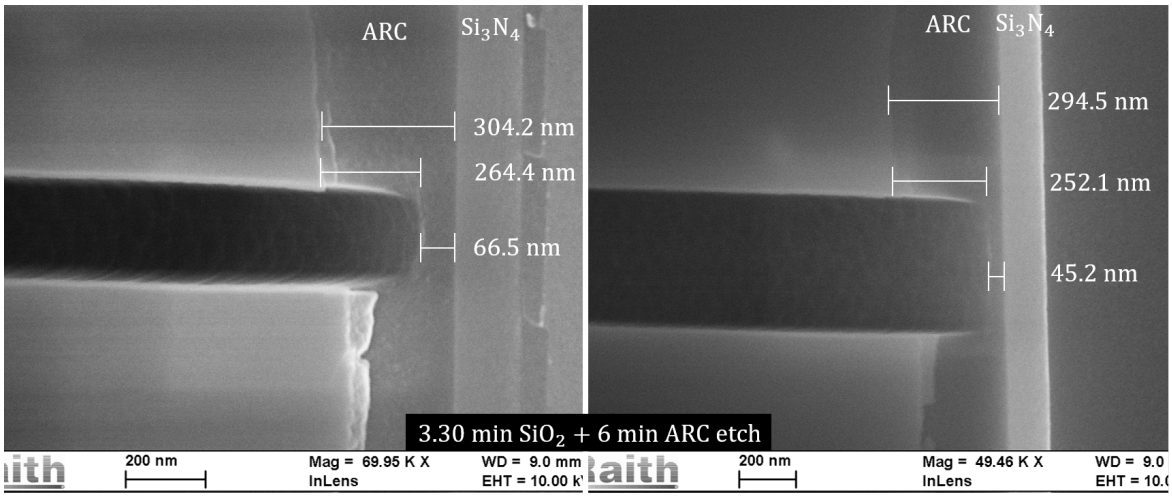

(c) Cross-section investigation at 45°.

Figure 6.5: SEM images of the cross-section after cleaving membrane chip 5 and after being exposed for 3.30 min SiO_2- and 6 min ARC-etch. (a), (b) and (c) show the results of the cross-section investigation at different tilting angles. Important to emphasize that the images were taken from the same sample. Hence, it is noticeable that the nonuniformity of the ARC-layer through the sample affects the thickness of the residual ARC.

Based on the results, the SiO_2-etch appears to be successful. The results also emphasize that the thickness of the ARC-layer is not equal throughout the sample. An etch rate of approximately 41-42 nm/min for the ARC-layer seems, however, to be consistent. An essential result presented here is the sidewall profile of the ARC-layer not being perfectly vertical. The results show the effect of undercut edge structure (see fig. (6.6) for the demonstration of under edge structure). The effect can be explained by the fact that the mask's edge is naturally in contact with a large volume of ions and radicals. Due to chemical reactions with the ions and radicals, the etching process occurs not only deeper in the etching window but also to the sides of the window (under the mask). The sidewall profile of the ARC can be either described as a positive profile or a low degree of bowing, see fig. (6.6). The author speculates that these two profile shapes can be explained mainly by the scattering in the plasma, causing the ions to move in several directions. Consequently, the upper part of the etching window will be exposed to more ions, and the bottom part of the sidewall will have lower etching activity. However, the bottom surface will still be etched by those ions coming in vertically relative to the surface.

It was also suspected that the sidewall profile of the ARC-layer might be the result of the line slope in the PMMA layer. A possible result is a SiO_2 hard-mask is subject to erosion accompanied with the faceting effect (see fig. (6.6)), which again can affect the result of the ARC-etch since the mask can give a direction to the incoming ions.

In order to address the issue of the ARC sidewall profile, a systematic investigation of the RF-power setting could have been performed. Decreasing and increasing the RF-power setting and seeing how the sidewall profile changes open the possibility of optimizing the value of the RF-power setting. In addition, the chamber pressure is also affected by the RF-power setting. Lower chamber pressure results in less ions scattering and consequently traveling more vertically. Reducing the chamber pressure below a certain point will, however, decrease the number of ions in the plasma. Hence, the etch rate will be reduced, or in the worst case, no etching will occur. Due to the concern of time, the etch parameters were not further investigated in this thesis.

It should also be pointed out that the ARC-etch result in the right image in fig. (6.5c) shows, however, a more vertical sidewall profile than the others. The difference in the results can be explained by the effect of the ions' direction during the RIE. Consequently, for the broader structure, as in the right image in fig. (6.5c), the ions can reach the bottom easier than in the case of a narrower structure [70].

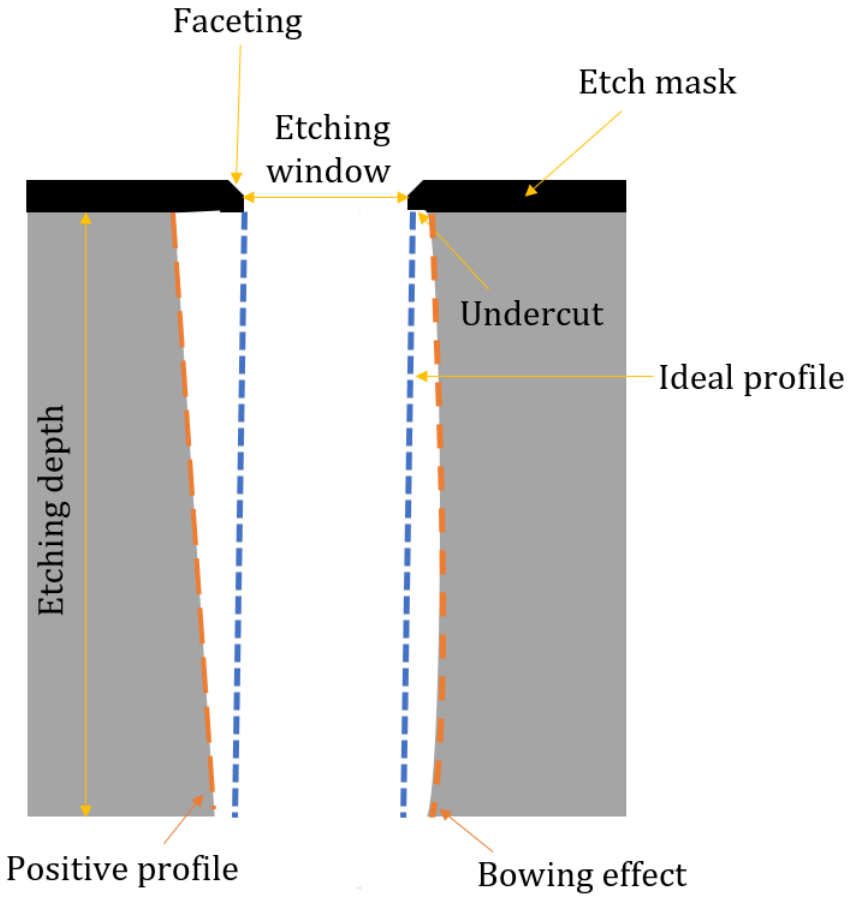

Figure 6.6: The figure demonstrates the effect of undercut, faceting, positive etch profile, and bowing effect of the etched structure.

In order to etch through the ARC-layer, the etch duration was determined to be around 8 min, based on the approximately ARC thickness of 330 nm from section (6.1.2). The result of increased ARC-etch duration to 8 min is shown in fig. (6.7).

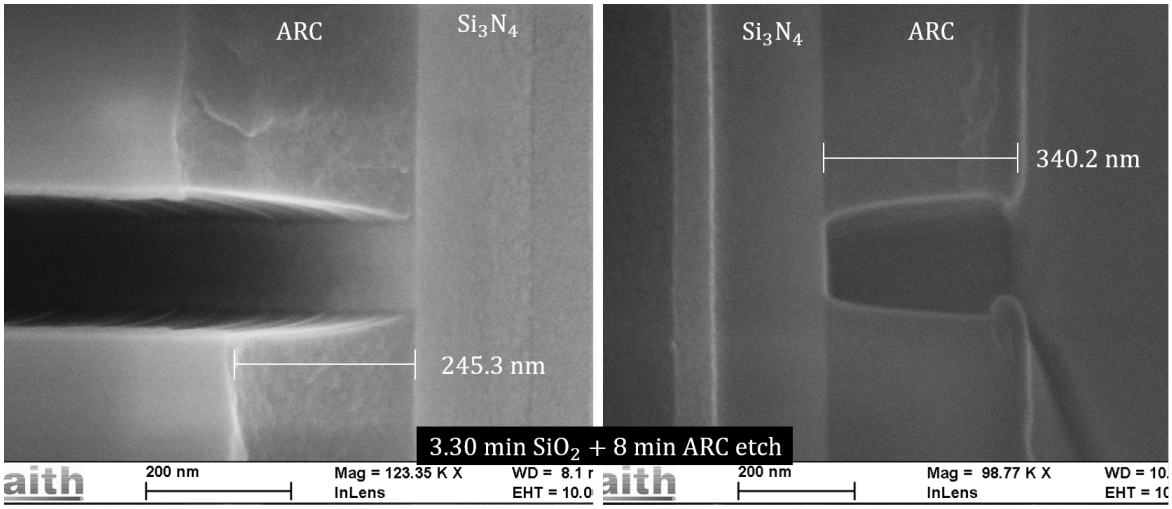

Figure 6.7: SEM images of the cleaved membrane chip 7 after 3.30 min SiO_2- and 8 min ARC-etch. Cross-section image at 45° tilt (left), and 90° (right).

The results in fig. (6.7) show a successfully pattern transfer from PMMA through SiO_2 to ARC-layer, with the parameters from [28] for SiO_2-etch and [27] for ARC-etch. With the thought of ARC thickness inhomogeneity, the author decided to increase the ARC-etch duration to 9 min to ensure that there are no ARC residues in the etching window. Hence, the underlying Si_3N_4 will be left exposed and not at risk under etching. The etch parameters found here should lead to a successful pattern transferring to the ARC-layer for the final fabrication.

Si_3N_4-etch

The results of Si_3N_4-etch of total etch duration 33 min, 48 min and 22 min are shown in fig. (6.8a), (6.8b) and (6.8c), respectively. It should be mentioned that the etch cycle in (a) is 3 min while (b) and (c) is 2 min. The author assumes this would not lead to a large difference between the processes. As can be seen, etching through the Si_3N_4 membrane is achieved in (6.8a) and (6.8b), but not in (6.8c) which is expected based on the estimated etch rate from the works in [27]. The results also indicate the inconsistency of the ARC thickness from sample to sample. For the Si_3N_4-etch, the sidewall profile of the ARC-layer appears to have an essential role. Because the edge of the ARC mask is eroded, the structure of the mask was further transferred to the Si_3N_4 membrane. As a result, the original structure has been lost in the final structure. A faceting similar effect is presented in the Si_3N_4 membrane, giving rise to the wider zone appearing when performing the surface investigation using SEM. This is illustrated in fig. (6.8b) and (6.8c). One approach to the problem is to reduce the RF-power setting for the Si_3N_4-etch, but due to time limitations, have not been realized.

Reducing the RF-power setting will decrease the ions bombarding the surface, hence, higher selectivity in the return of a lower etch rate.

The author decided to process the further works in the thesis based on the results from fig. (6.8c) and an approximately ARC-layer of 330 nm. The etch rate of Si_3N_4- and ARC-layer during the CF_4-etch is estimated to be 7.5 - 8 nm/min and 12 - 13 nm/min, respectively. That said, it was expected that the ARC etches at approximately the same rate as the Si_3N_4 during the CF_4-etch. Clearly, it is a significant difference in the etch rate of the two mentioned materials, hence, it can affect the aspect ratio (ratio between width and height of the structure) of the transferred structures. It is concluded that a 200 nm thick Si_3N_4 membrane can be successfully etched through with an etch duration of 28 min.

The determined etch rate of ARC-layer and Si_3N_4 are comparable with the work in [28] and [27]. The Si_3N_4-etch appears to be slightly lower, while the etch rate of the ARC-layer is $\sim$ 2 nm/min higher.

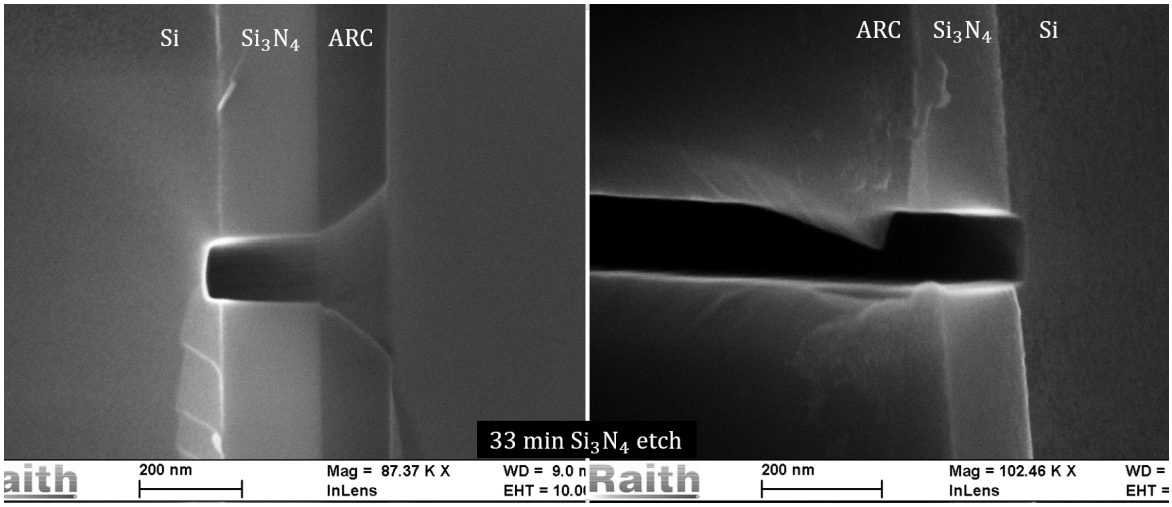

(a) Cross-section investigation at 90° (left) and 45° (right) of membrane chip 8 after 11 x 3 min Si_3N_4-etch (total time of 33 min).

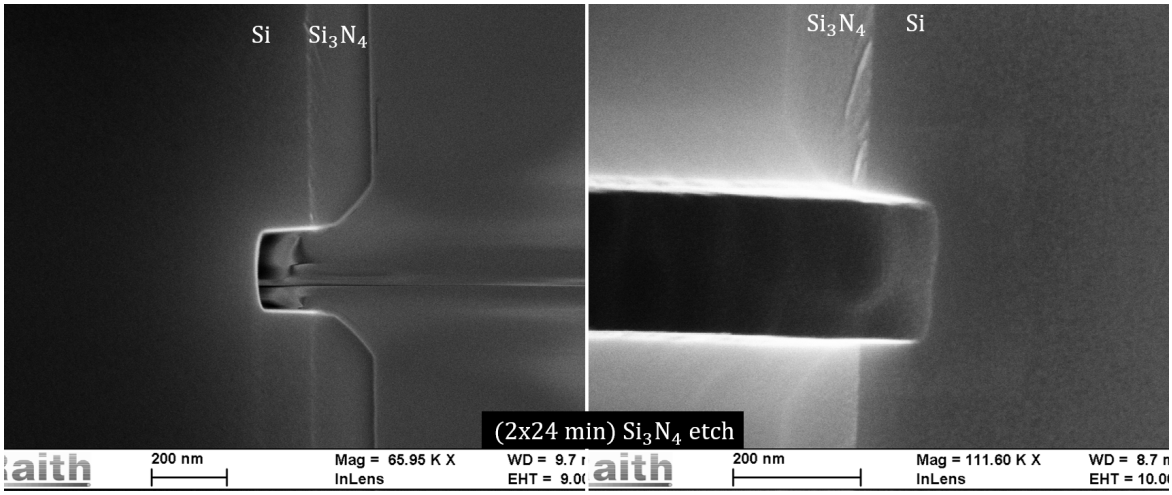

(b) Cross-section investigation at 90° (left) and 45° (right) of membrane chip 9 after 2 sequences of 12 x 2 min Si_3N_4-etch (total time of 48 min).

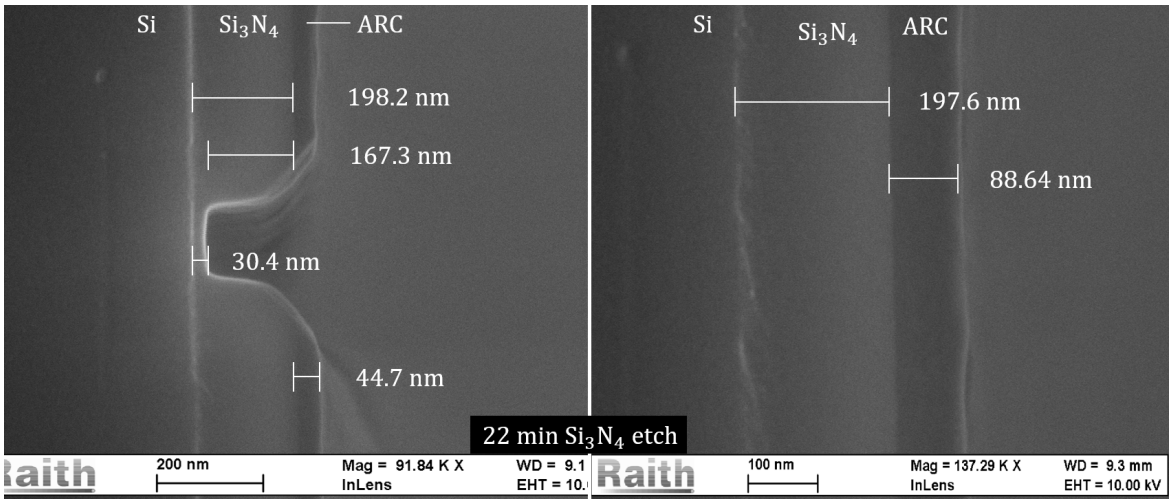

(c) Cross-section investigation at 90° of membrane chip 12 after 11 x 2 min Si_3N_4-etch (total time of 22 min).

Figure 6.8: SEM cross-section images of the cleaved membrane chip 8, 9 and 12 taken at 45° and 90° tilt. The membrane chips were etched with the sample parameters but different etch-duration, (a) 33 min, (b) 48min and (c) 22min. Note that all three samples were exposed with 3.30 min SiO_2- and 9 min ARC-etch.

6.2 Fresnel zone plate fabrication results

Fresnel zone plate

For the fabrication of the final free-standing Fresnel zone plates, the parameters presented in section (5.7) were used. The final fabrication results were examined with SEM and the results are presented in fig. (6.9) to (6.15). The fabricated zone plate with 20 μm diameter central block (zone plate 1), and 50 μm diameter central block (zone plate 2) are shown in fig. (6.9) and (6.10), respectively. The samples were coated with an approximately 3.5 nm thin layer of AuPd to enhance the contrast of the SEM imaging. Another importance of coating the sample with a thin layer of AuPd is the possibility of verifying that the transparent zones are completely etched free.

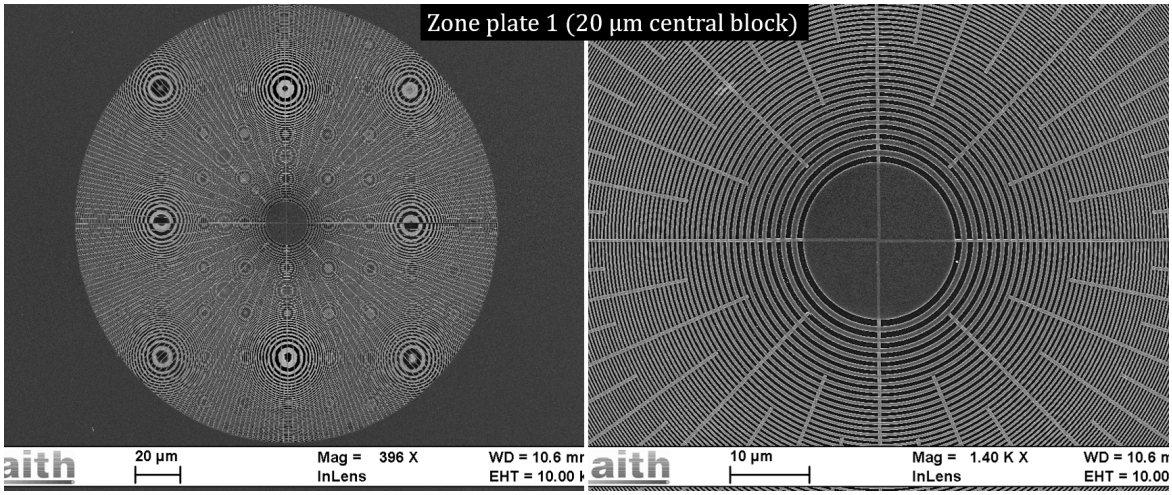

(a) Figure on the left shows the zone plate as a whole, while the right image is the closeup image around the innermost zones.

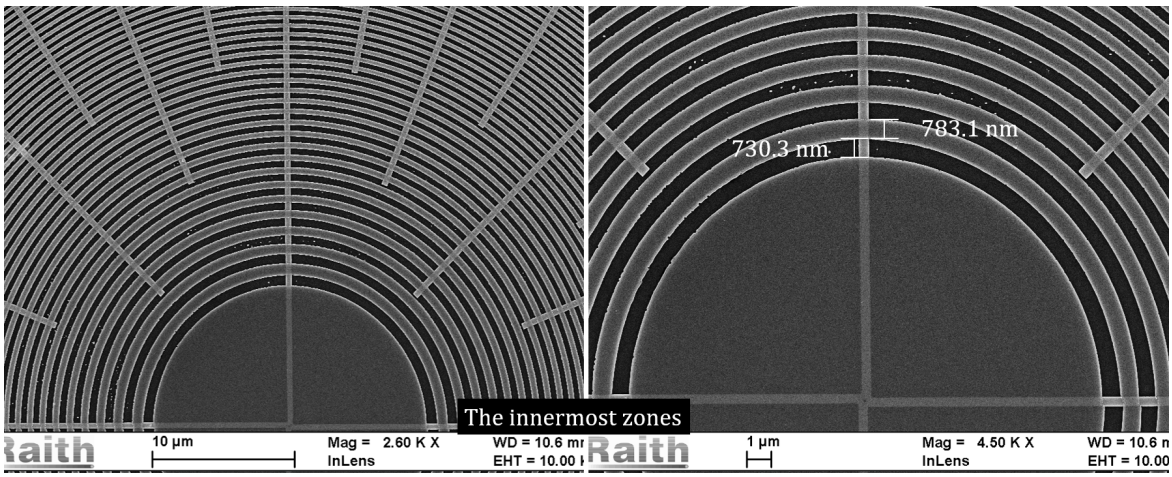

(b) Figures show the large image of the area around the innermost zones (left) and the closeup image (right) used for distance measurement.

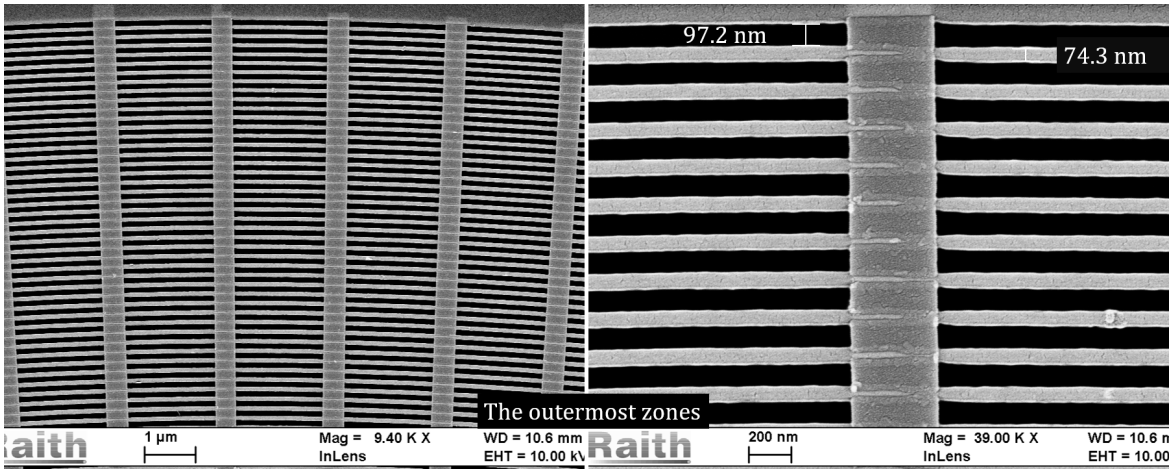

(c) Figures show the large image of the area around the innermost zones (left) and the closeup image (right) used for distance measurement.

Figure 6.9: Figures show different SEM images of the successful zone plate fabrication result (sample name: membrane chip 16 window 3). The membrane was exposed with "zone plate 1" pattern (with 20 µm central blocking). Note that the chip was coated with an approximately 3.5 nm thin layer of AuPd.

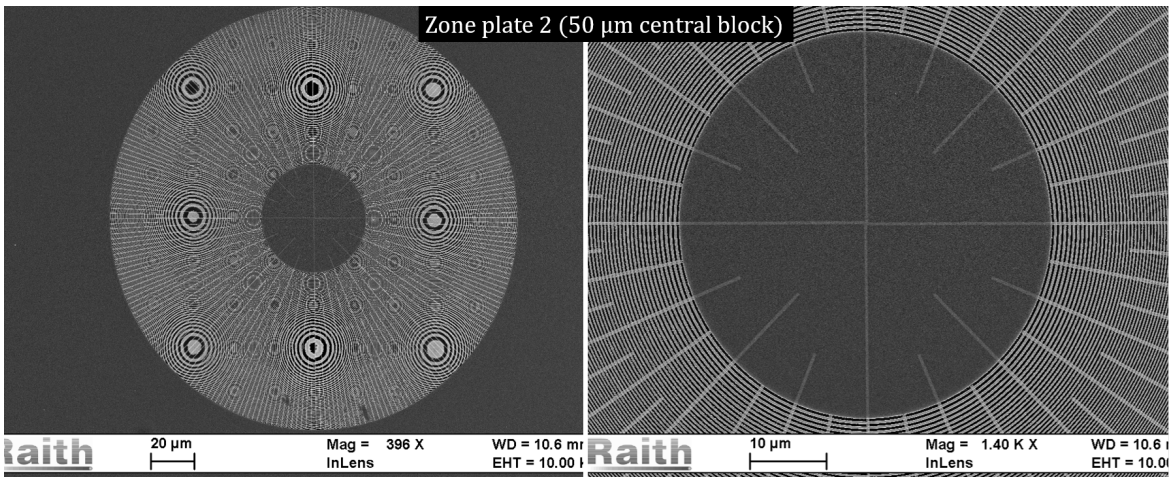

(a) Figure on the left shows the zone plate as a whole, while the right image is the closeup image around the innermost zones.

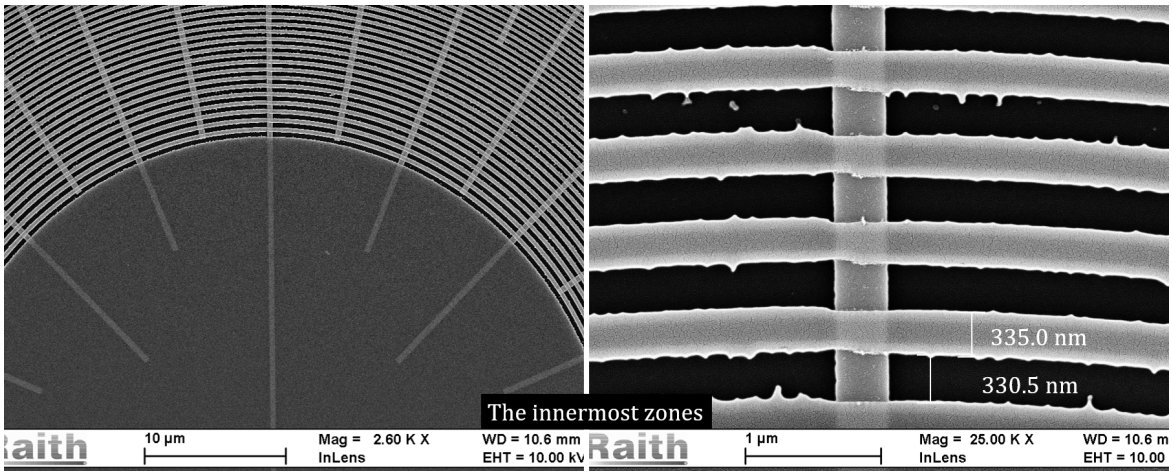

(b) Figures show the large image of the area around the innermost zones (left) and the closeup image (right) used for distance measurement.

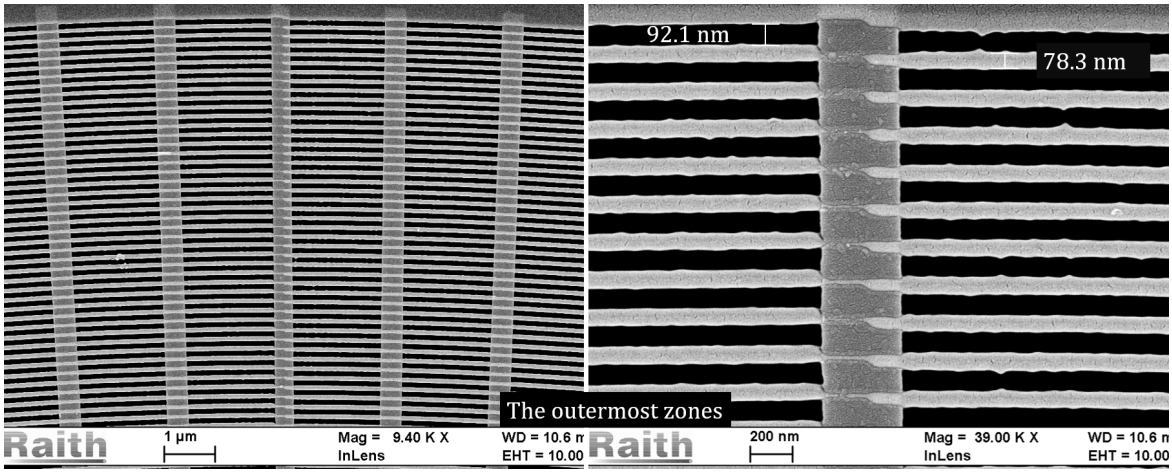

(c) Figures show the large image of the area around the innermost zones (left) and the closeup image (right) used for distance measurement.

Figure 6.10: Figures show different SEM images of the successful zone plate fabrication result (sample name: membrane chip 16 window 6). The membrane was exposed with "zone plate 2" pattern (with 50 µm central blocking). Some line edge roughness is presented in (b) and (c), which will be discussed later. Note that the chip was coated with an approximately 3.5 nm thin layer of AuPd.

As shown in fig. (6.9) and (6.10), the fabrication of the final free-standing Fresnel zone plate was successful, indicating a very promising method and fabrication recipe. Due to time limitations, it was not possible to test using the zone plates in the NEMI in order to see if the fabricated zone plates actually work. However, a detailed analysis of the entire zone plate reveals dimensions close to the designed dimensions, and it is therefore expected that the zone plates would perform as others tested in other works [15, 25].

Based on the results of the SEM images, it is found that the width of the zones is not exactly corresponding to the design specifications. In particular, the width of the outermost zones appears to be wider than expected. The author speculates that this can possibly be explained by the fact that the sidewall profile of the Si_3N_4 is not perfectly vertical, resulting in the zones appearing wider when imaging the surface using SEM, and/or due to proximity effects during the e-beam exposure. On the other hand, the innermost zones in fig. (6.9b) appear to be smaller than the theoretical value. This is suspected to be due to the value of dose-addition. The value of the dose-addition might not be the optimum value for the zone plate 1 structure since the value was based mainly on the results from the dose test of the zone plate 2 structure. Both of these effects it is possible to compensate for in later fabrication attempts.

Worth mentioning that during the fabrication process, complications can occur so that the zone plate pattern might be different for the design. An error in the ratio between the transparent and opaque zones known as open-ratio, which is designed to be 0.5, can give noticeable changes in the transmissivity and hence reduce the focusing efficiency as described in section (2.2.7). Moreover, the deviation of the zones width from the design will also worsen the zone plate performance as smaller or larger transparent zones will let fewer atoms through and, on the other hand, gives interference contribution destructively at the focus point.

Stitching-error

With that being said, several more free-standing zone plates were fabricated in this thesis. However, approximately 50% were imperfect due to stitching-error. No large stitching-error is appeared in the results in fig. (6.9) and (6.10) which are considered some of the best results obtained, but can be seen in the result in fig (6.2) and (6.11). It is difficult to give the exact reason for the stitching-error, but the author speculates that it can be explained mainly by three factors. First, due to an unoptimized write-field alignment procedure, meaning the optimum alignment between the coordinate of the stage and the beam deflection was not obtained. The achievable alignment

accuracy depends on the skill of the operator. It requires some training to achieve the best possible result. The second factor is due to the exposure time of the zone plates pattern was more than 2 hours. Hence, the probability of the beam position drift exists, which can affect the write-field alignment accuracy. Lastly, the temperature variation in the room where the e-Line is situated can cause the sample to expand or contract during the exposure. Consequently, the coordinates of the sample and the beam were misaligned.

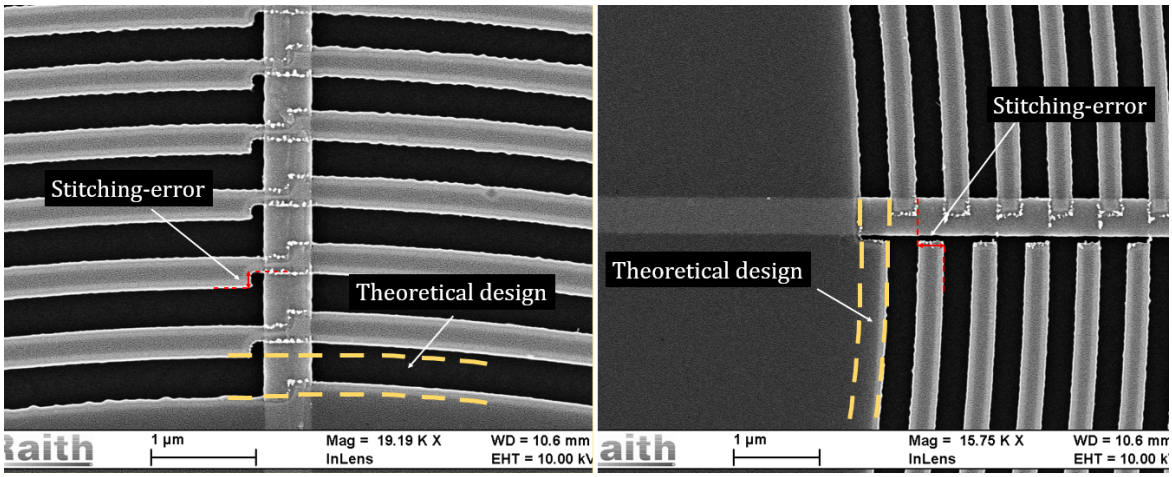

Figure 6.11: Figures show SEM images of an unsatisfactory result of the zone plate fabrication from chip 14 window 2 due to stitching-error. As shown, the stitching-error occurs along both horizontal and vertical axis. "Theoretical design" in the figure refers to the designed transparent zone.

The stitching-error was investigated further in this thesis. One way to minimize and potentially eliminate the error is to perform the EBL using 200 µm write-field setting, even though it in principle reduces the ultimate EBL resolution (increasing the minimum pixel size as mentioned in section (3.1) and defocusing of the beam as the distance from the write-field center is larger). With 200 µm write-field setting, the zone plate structure of 192 µm in diameter will fits inside a single write-field. Hence, the pattern stitching will not take place. The result from the testing with a 200 µm write-field is shown in fig. (6.12a) and (6.12b). Note that both figures illustrate 200 µm write-field zone plate from the same sample (membrane chip 16 window 7)

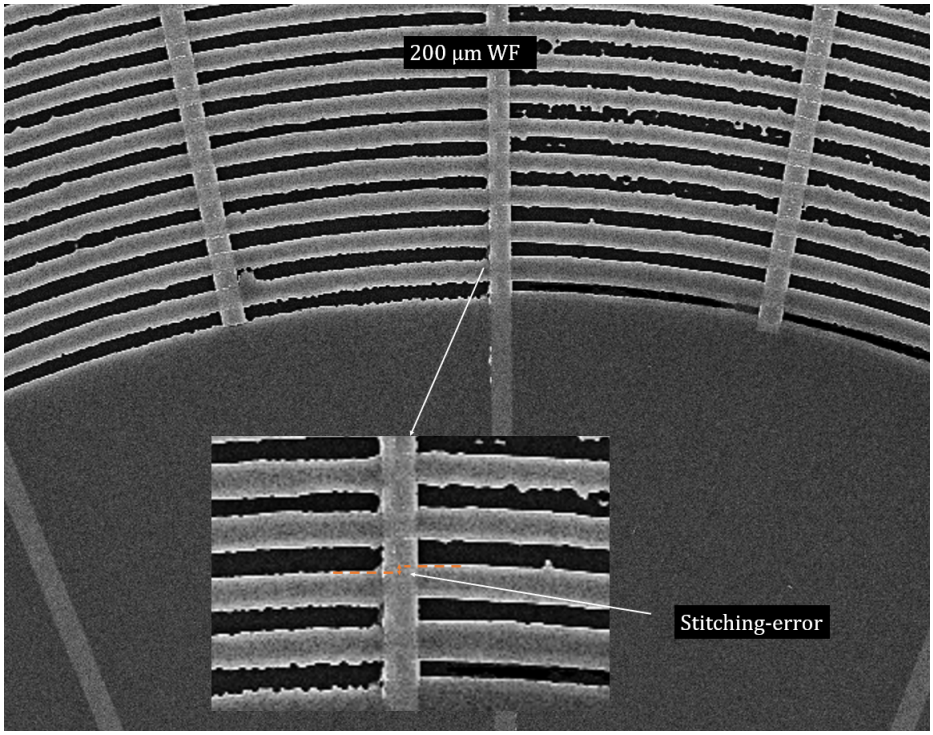

(a) Figure show closeup image of the area around the innermost zones (in the direction parallel with the vertical support bar). In the insets a closeup of the innermost zones and stitching-error are shown.

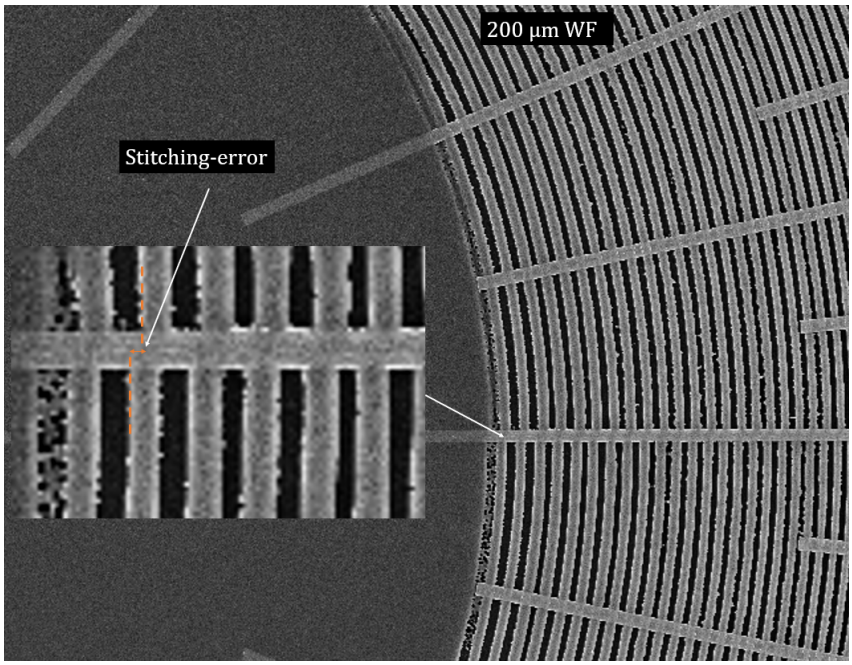

(b) Figure show closeup image of the area around the innermost zones (in the direction parallel with the horizontal support bar). In the insets a closeup of the innermost zones and stitching-error are shown.

Figure 6.12: Figures show SEM images of the zone plate fabrication result using 200 µm write-field setting. Membrane chip 16 window 7 was exposed with "zone plate 2" structure (with 50 µm central blocking) with an exposure dose of 225 pC/cm. Note that the chip was coated with an approximately 3.5 nm thin layer of AuPd to enhance the contrast in SEM.

As shown in the figures above, the stitching-error is still presented. The author speculates that this is due to an error in the pattern placement. If zone plate pattern was placed in the middle of four 200 µm x 200 µm write-fields, thus, the stitching of the pattern will still occur as demonstrate in the right image in fig. (6.13). This problem can however be adressed by simply adjust the placement such that the zone plate pattern is placed within a single 200 µm write-field as shown in the left image in fig. (6.13).

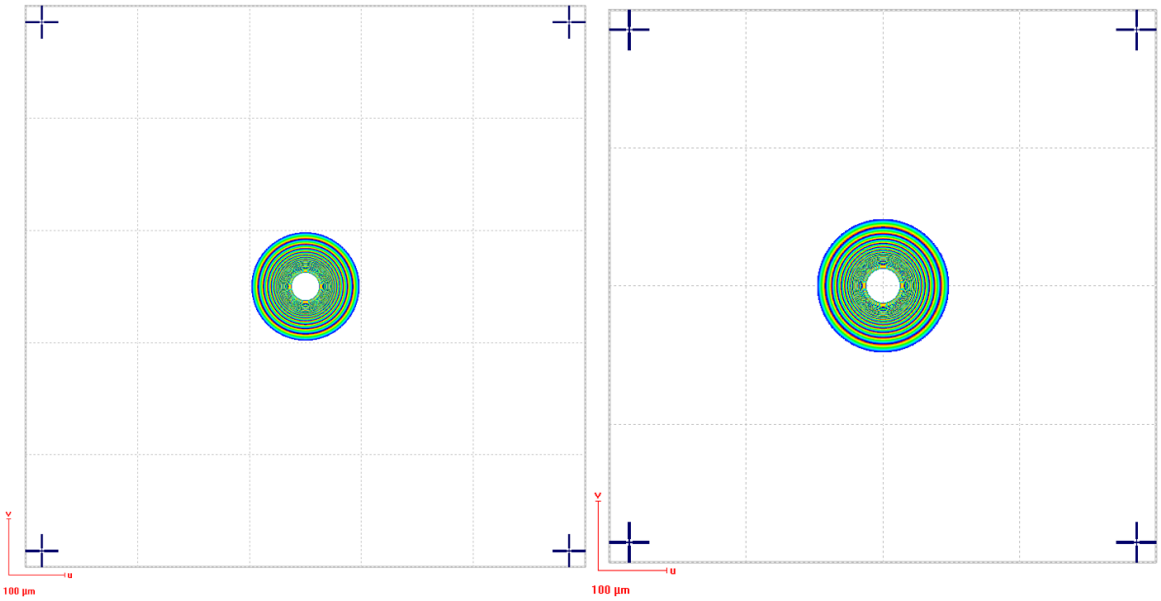

Figure 6.13: Figure demonstrates two different ways of pattern placement. A zone plate pattern is placed within a single write-field on the left side, eliminating the stitching. In contrast, the zone plate pattern is placed in the middle of four write-fields, hence the stitching of the pattern will occur. The squares in both figures correspond to 200 µm write-field.

Another imperfection that are shown in the 200 write-field setting zone plate is the line edge roughness, as will be discussed next.

Line edge roughness

In addition to the stitching-error, it is possible to see that some of the fabricated zone plates suffer from line edge roughness in some areas. This error can especially be seen from the result of dose test in fig. (6.10b) and 200 µm write-field zone plate in fig. (6.12). It is possible to explain the error with many factors, including mechanical vibration and substrate charging during the EBL, shot noise (as described in section (3.1)), contamination particles, insufficient exposure dose, and the step size value not being optimum. For the 200 µm write-field setting zone plate, the line edge roughness is likely to be due to the two latter factors (as the exposure dose might need optimization for different write-field settings) and the fact that the author did

not have much experience with working with 200 µm write-field setting, hence, some of the setting and the set up of write-field alignment might be incorrect.

In general, the value of the step size was further investigated by exposing zone plate structure with two different step sizes (with 100 µm write-field setting), and the results are shown in fig. (6.14). The result with 14 nm step size has a significantly smoother line edge. However, there is not enough data on this to verify that this is the case, and more experimenting has to be done to investigate this further.

With that being said, the contamination particles on the membrane chip should not be excluded. The membrane chips were investigated with an optical microscope after the RCA-cleaning step. It was possible to see some contamination on the membrane windows. Such contamination can result in a defect in the EBL pattern, which can be the reason for the line edge roughness of the etched structures.

Overall, the author does not consider the error as a significant problem since, most of the time, the line edge roughness amounts did not have a significant portion of the zones and will therefore not affect the focusing efficiency on a large scale. Again, more data is needed to investigate this further.

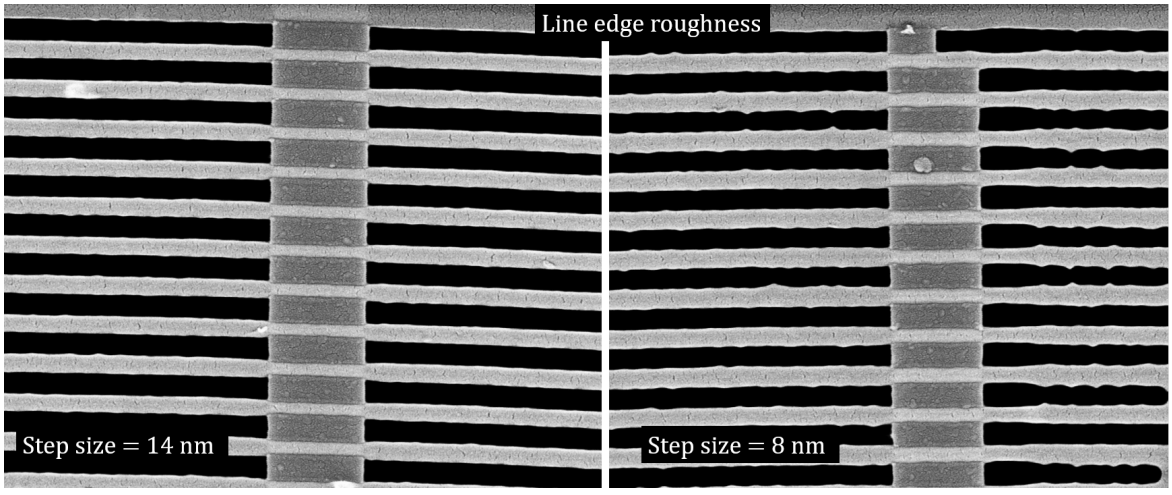

Figure 6.14: Figures show SEM images of the zone plate fabrication result two different step size settings, 14 nm on the left and 8 nm on the right. Membrane chip 15 window 2 and 3 was exposed with "zone plate 2" structure (with 50 um central blocking) with an exposure dose of 225 pC/cm and 100 µm write-field setting. Note that the chip was coated with an approximately 3.5 nm thin layer of AuPd to enhance the contrast in SEM.

Damaged membrane

Lastly, it should be pointed out that as in all experimental work, not all of them work as expected and some of the membranes broke during fabrication, as illustrated in fig. (6.15). As only some of the membranes broke, it is speculated that weaknesses or defects were introduced to the membranes from a countless number of times they are handled from the moment they are going for the first lithography step - even before being etched free of the silicon. Also worth noticing from fig. (6.15) that there are some sort of white material that resembles scratches.

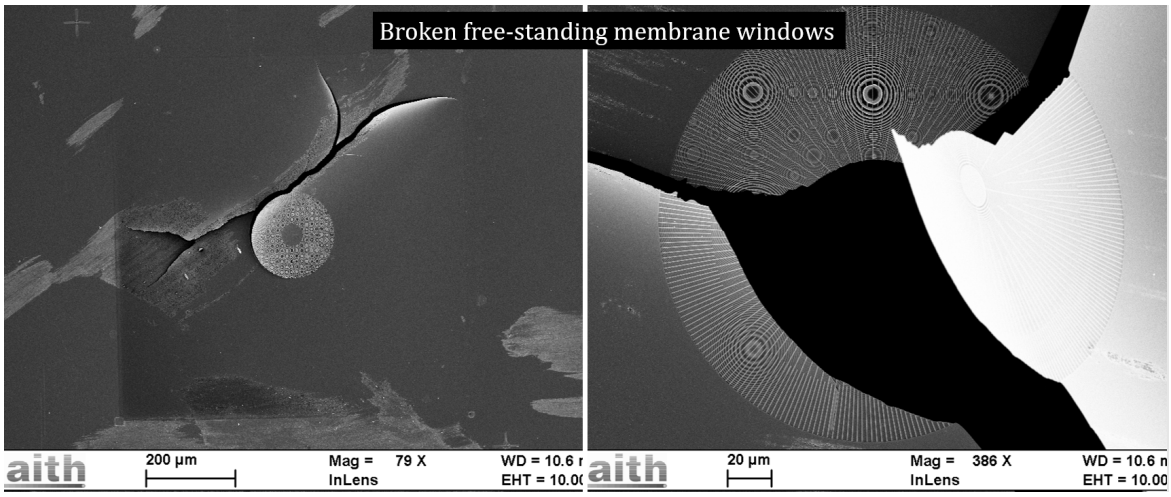

Figure 6.15: Figures show SEM images of the membrane windows from chip 14 being broken after several RIE steps as described in 5.7.6. Membrane window 1 (left), and 3 (right).

Chapter 7

Conclusion and Suggestions for Future Work

In this thesis, the objective has been to fabricate a free-standing Fresnel zone plate for neutral helium atomic microscope NEMI. Based on the experience of the UiB nanophysics group, the fabrication of dense free-standing structures can be very challenging. Thus, a lot of effort is required in the final fabrication process but also the optimization of the working parameters, including layer thicknesses, electron beam exposure, and reactive ion etching parameters. Exceeding all of the expectations, a free-standing Fresnel zone plate with 20 μm and 50 μm diameter central block for NEMI for the cold-nozzle beam was successfully fabricated with the optimized parameters. Zone plates with an outermost zone width of approximately 90 nm and an overall diameter of 192 μm were achieved. The results show completely etched through transparent zones with dimensions very close to the designed dimensions. It is therefore expected that the fabricated zone plates will perform as predicted.

The author concluded that the results in this thesis are very promising and open the door for the more routinely fabrication of a free-standing Fresnel zone plate for a neutral helium atomic beam microscope and other dense free-standing structures. However, there is still a lot of room for improvement, particularly the stitching-error and the sidewall profile of ARC-etch.

Now that the necessary fabrication process has been established, it can be extended. A free-standing Fresnel zone plate for room temperature with outermost zone width of 48 nm is of interest, which is the best of our knowledge today [25]. To reach the high-resolution with EBL-system such as Raith e-Line, both the exposure and development conditions should be considered interdependent and optimized simultaneously. For future works, other possibilities resist, such as AR-P 6200 (CSAR 62) due to higher contrast and sensitivity might be a good option [60]. A better resist contrast can also improve the resolution at the bottom of the resist layer and, in general, the resist profile

after the development, which in turn can solve the issue of the sidewall profile angle in the ARC-layer and thus the Si_3N_4 membrane. The process of cold-development should be considered, as it has been found to improve feature quality and resolution [71, 72]. Working with other resist and development process will, however, require an investigation of the exposure and development parameters in order to achieve the best possible result.

A suggestion for further studies could be to investigate the ARC sidewall profile in more detail as it significantly affects the final structure. Higher and lower RF-power setting in the RIE process should be tested to address how it affects the sidewall profile. In addition, decreasing chamber pressure can in principle improve the etch anisotropy. Another way around is to have a thicker layer of ARC and increase the Si_3N_4-etch duration from 28 min to 33 min to obtain the results as in fig. (6.8a). It should also be considered to use another ARC to prevent two steps of the ARC-coating which can improve the thickness homogeneity and coating consistency. As a result, it will be easier to determine the etch rate and etch duration.

For the issue of the zone width deviating from the theoretical value, the issue of the zone oversizing might be solved with a better sidewall profile of the ARC-layer, and hence the Si_3N_4-layer. In general, more detailed investigations of the exposure dose should be carried out since it can limit the proximity effect, and more precise control of the exposed structure dimensions can be achieved. Another approach is to modify the zone plate design such that the exposure dose increases with decreasing zone width. Consequently, it will reduce the chance of the large zones being oversize due to the proximity effect. In addition, the smaller zones will have a higher exposure dose reducing the concern of shot noise. However, this requires advanced MATLAB code modification for the structure design.

Lastly, working with 200 µm write-field size is recommended as this will eliminate the issue stitching-error, thus, improving the performance of the zone plates. With that being said, the limitation of the addressable resolution in the EBL and defocusing of the e-beam when the distance from the write-field center need to be further investigated. Additionally, an exposure parameter tuning might be necessary based on the result from 200 µm working in this thesis.

Bibliography

[1] L. De Broglie. *Recherches sur la th´eorie des quanta.* PhD thesis, Migration-universite en cours d'affectation, 1924.

[2] M. Arndt, P. Szriftgiser, J. Dalibard, and A. M Steane. Atom optics in the time domain. *Phys. Rev. A*, 53:3369–3378, May 1996.

[3] K. Wohlfart, F. Grätz, F. Filsinger, H. Haak, G. Meijer, and J. Küpper. Alternating-gradient focusing and deceleration of large molecules. *Phys. Rev. A*, 77:031404, Mar 2008.

[4] A. Libson, M. Riedel, G. Bronshtein, E. Narevicius, U. Even, and M. G Raizen. Towards coherent control of supersonic beams: a new approach to atom optics. *New Journal of Physics*, 8(5):77–77, May 2006.

[5] O. Steuernagel. Wide optical lenses for atomic beams. In *CLEO/Europe and EQEC 2009 Conference Digest*. Optica Publishing Group, 2009.

[6] M. T Postek, A. Vladár, C. Archie, and B. Ming. Review of current progress in nanometrology with the helium ion microscope. *Measurement Science and Technology*, 22(2):024004, Dec 2010.

[7] L. Xiao and E. S Yeung. Optical imaging of individual plasmonic nanoparticles in biological samples. *Annual Review of Analytical Chemistry*, 7(1):89–111, 2014. PMID: 24818812.

[8] B. M Barnes, M. Y Sohn, F. Goasmat, H. Zhou, E. V András, R. M Silver, and A. Arceo. Three-dimensional deep sub-wavelength defect detection using $\lambda = 193$ nm optical microscopy. *Opt. Express*, 21(22):26219–26226, Nov 2013.

[9] R. Zhou, C. Edwards, A. Arbabi, G. Popescu, and L. L Goddard. Detecting 20 nm wide defects in large area nanopatterns using optical interferometric microscopy. *Nano Letters*, 13(8):3716–3721, 2013. PMID: 23899129.

[10] L. Scipioni, L.A Stern, J. N, S. Sijbrandij, and B. Griffin. Helium ion microscope. *Advanced Materials Processes*, 166(6):27–30, 2008.

[11] S. D Eder, T. Reisinger, M. M Greve, G. Bracco, and B. Holst. Focusing of a neutral helium beam below one micron. *New Journal of Physics*, 14(7):073014, Jul 2012.

[12] S. D Eder, X.D Guo, T. Kaltenbacher, M. M Greve, M. Kalläne, L. Kipp, and B. Holst. Focusing of a neutral helium beam with a photon-sieve structure. *Physical Review A*, 91, May 2015.

[13] S. D Eder. *A neutral matter wave micro scope (NEMI): design and setup*. PhD thesis, University of Bergen, UoB, December 2011.

[14] E. Selfors. Fabrication of large free-standing nanostructured zone plates for focusing a bose-einstein condensate. Master's thesis, University of Bergen, UoB, 2010.

[15] M. M Greve. Testing nano-structured fresnel zoneplates for neutral helium microscopy on a molecular-beam ultra-high-vacuum apparatus. Master's thesis, University of Bergen, UoB, 2017.

[16] R. B Doak, R. E Grisenti, S. Rehbein, G. Schmahl, J. P Toennies, and Ch. Wöll. Towards realization of an atomic de broglie microscope: Helium atom focusing using fresnel zone plates. *Phys. Rev. Lett.*, 83:4229–4232, Nov 1999.

[17] J. C Weaver and J. G. King. The molecule microscope: A new instrument for biological and biomedical research. *Proceedings of the National Academy of Sciences*, 70(10):2781–2784, 1973.

[18] B. Holst and W. Allison. An atom-focusing mirror. *Nature*, 390:244–244, Nov 1997.

[19] A. E Ross, D. A MacLaren, and W. Allison. Finite element analysis of adaptive atom-optical mirrors. *Journal of Physics D: Applied Physics*, 44(18):185501, Apr 2011.

[20] K. Fladischer, H. Reingruber, T. Reisinger, V. Mayrhofer, W. E Ernst, A. E Ross, D. A MacLaren, W. Allison, D. Litwin, J. Galas, S. Sitarek, P. Nieto, D. Barredo, D. Farías, R. Miranda, B. Surma, A. Miros, B. Piatkowski, E. Søndergård, and B. Holst. An ellipsoidal mirror for focusing neutral atomic and molecular beams. *New Journal of Physics*, 12(3):033018, Mar 2010.

[21] H. C Schewe, B. S Zhao, G. Meijer, and W. Schöllkopf. Focusing a helium atom beam using a quantum-reflection mirror. *New Journal of Physics*, 11(11):113030, Nov 2009.

[22] D. R Miller. *Atomic and Molecular Beam Methods*, volume 1, chapter 2. G Scoles (Oxford: Oxford University Press), 1998.

[23] T. Reisinger and B. Holst. Neutral atom and molecule focusing using a fresnel zone plate. *Journal of Vacuum Science Technology B - J VAC SCI TECHNOL B*, 26, Nov 2008.

[24] T. Reisinger. *Free-standing, axially-symmetric diffraction gratings for neutral matter-waves: experiments and fabrication.* PhD thesis, University of Bergen, UoB, August 2011.

[25] T. Reisinger, S. D Eder, M M. Greve, I Smith H, and B. Holst. Free-standing silicon-nitride zoneplates for neutral-helium microscopy. *Microelectronic Engineering*, 87(5):1011–1014, 2010. The 35th International Conference on Micro- and Nano-Engineering (MNE).

[26] A. A Yanik, M. Huang, O. Kamohara, A. Artar, T. W. Geisbert, J. H Connor, and H. Altug. An optofluidic nanoplasmonic biosensor for direct detection of live viruses from biological media. *Nano Letters*, 10(12):4962–4969, 2010. PMID: 21053965.

[27] R. Flatabø. *Charged Particle Lithography for the Fabrication of Nanostructured Optical Elements.* PhD thesis, University of Bergen, UoB, June 2018.

[28] J. Grepstad, M. M Greve, T. Reisinger, and B. Holst. Nanostructuring of free-standing, dielectric membranes using electron-beam lithography. *Journal of Vacuum Science Technology B: Microelectronics and Nanometer Structures*, 31:06F402–06F402, Nov 2013.

[29] European Union's Horizon 2020 research and innovation program. New nano patterning technique offers hope for making large scale patterns with individual molecules, 2020. url: `https://www.nanolace.eu/about/`, urldate: 2022-11-5.

[30] M. Born and E. Wolf. *Principles of Optics. Electromagnetic Theory of Propagation, Interference and Diffraction of Light.* Pergamon Pr, 6th edition, 1980.

[31] E. Hecht. *Optics*, chapter 10. Addison-Wesley, Reading, Mass, 2002.

[32] S. Wu, Y.g Hwu, and G. Margaritondo. Hard-x-ray zone plates: Recent progress. *Materials*, 5(10):1752–1773, 2012.

[33] A. G Michette. *Optical systems for soft X-rays.* Plenum Press, 1986.

[34] W. Watanabe, D. Kuroda, K.i Itoh, and J. Nishii. Fabrication of fresnel zone plate embedded in silica glass by femtosecond laser pulses. *Opt. Express*, 10(19):978–983, Sep 2002.

[35] H. E White and F. A Jenkins. *Fundamentals of optics*, chapter 4,13. McGraw-Hill Primis Custom Publishing, 4 edition, December 2001.

[36] A. Lipson, S.G Lipson, and H. Lipson. *Optical Physics*. Cambridge University Press, 2011.

[37] E. Di Fabrizio, F. Romanato, M. Gentili, S. Cabrini, B. Kaulich, J. Susini, and R. Barrett. High-efficiency multilevel zone plates for kev x-rays. *Nature*, 401:895–898, Oct 1999.

[38] NanoSuite. *Software Reference Manual*. Raith GmbH, Konrad-Adenauer Allee 8, 44263 Dortmund , Germany, 3 edition, June 2010. Document number2-07-1.0.

[39] N. Chiromawa and K. Ibrahim. Applications of electron beam lithography (ebl) in optoelectronics device fabrication. Jan 2018.

[40] O. Şahin. Optimazation of electron beam lithography and lift-off process for nanofabrication of sub-50 nm gold nanostructures. Master's thesis, Sabancı University, 2019.

[41] M. M Greve and B. Holst. Optimization of an electron beam lithography instrument for fast, large area writing at 10kv acceleration voltage. *Journal of Vacuum Science & Technology B*, 31(4):043202, 2013.

[42] M. Krogt. High-dose exposure of silicon in electron beam lithography. *Journal of Micro/Nanolithography, MEMS, and MOEMS*, 7:013005, Jan 2008.

[43] N. Yahya. *Carbon and Oxide Nanostructures*. Springer Berlin Heidelberg, 1st ed. edition, 2011.

[44] Y. Ishii, J. Taniguchi, K. Ishikawa, Y. Sakamoto, I. Sato, and I. Miyamoto. Electron beam lithography using inorganic resist at low acceleration voltage. pages 110–111, 2005.

[45] P. Rai-Choudhury. *Handbook of Microlithography, Micromachining and Microfabrication: Handbook of Microlithography, Micromachining and Microfabrication*. Press Monographs. SPIE Press, Bellingham, WA, October 1999.

[46] J. Orloff. *Handbook of charged particle optics*. CRC Press/Taylor & Francis, Boca Raton, 2009.

[47] B. D Vogt, E. K Lin, W.I Wu, and C. C White. Effect of film thickness on the validity of the sauerbrey equation for hydrated polyelectrolyte films. *The Journal of Physical Chemistry B*, 108(34):12685–12690, 2004.

[48] K. Nojiri. *Dry Etching Technology for Semiconductors*. Springer International Publishing, Cham, 2015.

[49] H. Horiike. Proc. 19th semiconductor technology seminar, 1981.

[50] M. J Kushner. Monte-carlo simulation of electron properties in rf parallel plate capacitively coupled discharges. 54, Sep 1983.

[51] J. Upadhyay, Do Im, S. Popović, A.M Valente-Feliciano, L. Phillips, and L. Vušković. Self-bias dependence on process parameters in asymmetric cylindrical coaxial capacitively coupled plasma. 14,6 1432, Mar 2015.

[52] A. Efremov and et al. On relationships between gas-phase chemistry and reactive ion etching kinetics for silicon-based thin films (sic, SiO_2 and Si_xN_y) in multicomponent fluorocarbon gas mixtures. 2015.

[53] Y. Leng. *Materials Characterization: Introduction to Microscopic and Spectroscopic Methods*. Wiley, Hoboken, 2nd ed. edition, 2013.

[54] A. Ul-Hamid. *A Beginners Guide to Scanning Electron Microscopy*. Cham Springer International Publishing, Hoboken, 1st ed. edition, 2018.

[55] S. Rehbein. *Entwicklung von freitragenden nanostrukturierten Zonenplatten zur Fokussierung und Monochromatisierung thermischer Helium-Atomstrahlen*. Cuvillier Verlag Göttingen, Göttingen, 2001.

[56] L. Koechlin, D. Serre, and P. Duchon. High resolution imaging with fresnel interferometric arrays: suitability for exoplanet detection. *Astronomy & Astrophysics*, 443(2):709–720, November 2005.

[57] K. P Ghosh. Process optimization on raith-150 two e-beam lithography tool for sub-100nm cmos device fabrication. Master's thesis, Indian Institute of Technology, Bombay, 2009.

[58] C. Vieu, F. Carcenac, A. Pépin, Y. Chen, M. Mejias, A. Lebib, L. Manin-Ferlazzo, L. Couraud, and H. Launois. Electron beam lithography: resolution limits and applications. *Applied Surface Science*, 164(1):111–117, 2000. Surface Science in Micro Nanotechnology.

[59] R. Flatabø, M. M Greve, S. D Eder, M. Kalläne, A. S Palau, K. K Berggren, and B. Holst. Atom sieve for nanometer resolution neutral helium microscopy. *Journal of Vacuum Science & Technology B*, 35(6):06G502, 2017.

[60] M. Schirmer and B. Schirmer. *Product information E-BEAM RESIST*. ALLRESIST GmbH, January 2017.

[61] S. Ma, C. Con, M. Yavuz, and B. Cui. Polystyrene negative resist for high-resolution electron beam lithography. *Nanoscale research letters*, 6:446, 07 2011.

[62] J. Shen, F. Aydinoglu, M. Soltani, and B Cui. E-beam lithography using dry powder resist of hydrogen silsesquioxane having long shelf life. *Journal of Vacuum Science Technology B*, 37:021601, 03 2019.

[63] R. Wüest, P. Strasser, F. Robin, D. Erni, and H. Jaeckel. Fabrication of a hard mask for inp based photonic crystals: Increasing the plasma-etch selectivity of poly(methyl methacrylate) versus SiO_2 andSiN_x. *Journal of vacuum science technology. B, Microelectronics and nanometer structures: processing, measurement, and phenomena: an official journal of the American Vacuum Society*, 26:3197–3201, Nov 2005.

[64] M. M Greve. *Nanostructuring for the manipulation of electromagnetice waves.* PhD thesis, University of Bergen, UoB, June 2013.

[65] D. Barth. *Raith eLiNE Standard Operating Procedure*. The Princeton Institute for the Science and Technology of Materials (PRISM), 70 Prospect Ave, Princeton, NJ 08540, USA, 4 edition, March 2019.

[66] A. M Engwall, Z. Rao, and E. Chason. Origins of residual stress in thin films: Interaction between microstructure and growth kinetics. *Materials Design*, 110:616–623, 2016.

[67] S. Zheng, R. K. Dey, A. Ferhat., and B. Cui. Mixture of zep and pmma with varying ratios for tunable sensitivity as a lift-off resist with controllable undercut. *Journal of Vacuum Science Technology B*, 34, Nov 2016.

[68] R. Wüest, P. Strasser, F. Robin, D. Erni, and H. Jaeckel. Fabrication of a hard mask for inp based photonic crystals: Increasing the plasma-etch selectivity of poly(methyl methacrylate) versus si o2 and si nx. *Journal of vacuum science technology. B, Microelectronics and nanometer structures: processing, measurement, and phenomena: an official journal of the American Vacuum Society*, 26:3197–3201, Nov 2005.

[69] V. Yurgens, F. Koch, M. Scheel, T. Weitkamp, and C. David. Measurement and compensation of misalignment in double-sided hard x-ray fresnel zone plates. *Journal of Synchrotron Radiation*, 27, 05 2020.

[70] T. Xu, Z. Tao, H. Li, X. Tan, and H. Li. Effects of deep reactive ion etching parameters on etching rate and surface morphology in extremely deep silicon etch process with high aspect ratio. *Advances in Mechanical Engineering*, 9(12):1687814017738152, 2017.

[71] W. Hu, K. Sarveswaran, M. Lieberman, and G. Bernstein. Sub-10 nm electron beam lithography using cold development of poly (methylmethacrylate). *Journal of Vacuum Science Technology B Microelectronics and Nanometer Structures*, 22:1711–1716, 07 2004.

[72] Bryan M.C, Jodie L.L, and Karl K.B. Optimal temperature for development of poly(methylmethacrylate). *Journal of Vacuum Science & Technology B*, 25:2013–2016, 2007.

Appendix A

MATLAB code

A.1 Support bars structure design

Main code:

```
clear;
%% writes support bar pattern into filename
% Use:
%- write_pixel_path_1
%- writepath_1

%%size of write field in microns (should be a multiple of 10)

%% settings

writefield = 100.0; % writefield size not important here,
% since it is not reflected in pattern (paths cross writefield ...
    borders)
% splitting of paths between writefields is performed by Raith ...
    software
filename = ['2zpsupp_nemiLN_d196_7Mar_Final'];

zpradius = 96; % zoneplate radius in microns
supportbarwidth = 0.430; % 450nm supportbars - rehbein
centeroffield = [500 500]; % coordinates of center of zoneplate in ...
    microns,
% => offset to make sure that support cross does not lie on ...
    writefield borders


%% Zoneplate parameters, wavelength=lambda, g = distance source to ...
    zp, b = distance zp to detector

```

```
24 %% magie cold
25 %lambda = 9.78e-11;
26 %g=1.5;
27 %b=0.7;
28
29 %% nemi RT
30 % lambda = 0.547e-10;
31 % g=0.935;
32 % b=0.205;
33
34 %% nemi cold
35 lambda = 9.78e-11;
36 g=0.935;
37 b=0.205;
38
39 %% set to 1 to output cif (not sure if this still works!!)
40 cifflag = 0;
41 if (cifflag)
42     extension = '.cif';
43 else
44     extension = '.asc';
45 end
46
47 %% open output file
48 fid=fopen([filename extension],'wt');
49
50 %% file header for cif file
51 if (cifflag)
52     fprintf(fid,'L L1;\n');
53 end
54
55 % compute writefield minimal step, to avoid rounding with pattern ...
       generator
56 % (can lead to errors)
57 %machine_step = ceil(writefield*1000 / 2^16) / 1000;
58
59 %machine_step = 0.0032;
60 machine_step = 0.004;
61 %machine_step = ceil(writefield*1000 / 2^16) / 1000;
62 %%%%%%%%%%%%%%%%%%%%%%%%%%%%%%%%%%%%%%%%%%%%%%%%%%%%%%%%%%%%%%%%
63 %% write grid marks into layer 1
64
65 % size of gridmarks and period
66 gridconstant = 1000; % 1.2mm => placement of gridmarks outside of ...
       membrane!
67 gridmarklength = 30;
```

```
68 gridmarklength2 = 5;
69 gridmarkwidth = 3.0;
70 gridmarkwidth2 = 0.5;
71
72 gridmarkdose = 100.0;
73 gridsize = 1;
74 vertices = 1000;
75 rotation = 0;
76
77 % coordinates of bottom left writefield corner
78 bottomleft = [0 0];
79
80 markoffset = gridconstant/2 - gridmarklength;
81
82 layer = 1;
83
84 for i = 1:gridsize
85    for j = 1:gridsize
86        Mark_dose = gridmarkdose - 0;
87        thiscenter = bottomleft + [(i-0.5)*gridconstant, ...
              (j-0.5)*gridconstant];
88
89        thismarkpos = thiscenter + [-markoffset,-markoffset];
90
91        path(1).coord(:,1) = thismarkpos + [-gridmarklength,0];
92        path(1).coord(:,2) = thismarkpos + [-gridmarklength2,0];
93        path(2).coord(:,1) = thismarkpos + [gridmarklength2,0];
94        path(2).coord(:,2) = thismarkpos + [gridmarklength,0];
95        path(3).coord(:,1) = thismarkpos + [0,-gridmarklength];
96        path(3).coord(:,2) = thismarkpos + [0,-gridmarklength2];
97        path(4).coord(:,1) = thismarkpos + [0,gridmarklength2];
98        path(4).coord(:,2) = thismarkpos + [0,gridmarklength];
99        writepath_1(1:4,path,gridmarkwidth,Mark_dose,layer..
100       ,cifflag,fid);
101       path(1).coord(:,1) = thismarkpos + [-gridmarklength2,0];
102       path(1).coord(:,2) = thismarkpos + [0,0];
103       path(2).coord(:,1) = thismarkpos + [0,0];
104       path(2).coord(:,2) = thismarkpos + [gridmarklength2,0];
105       path(3).coord(:,1) = thismarkpos + [0,-gridmarklength2];
106       path(3).coord(:,2) = thismarkpos + [0,0];
107       path(4).coord(:,1) = thismarkpos + [0,0];
108       path(4).coord(:,2) = thismarkpos + [0,gridmarklength2];
109       writepath_1(1:4,path,gridmarkwidth2,Mark_dose,layer..
110       ,cifflag,fid);
111
112       thismarkpos = thiscenter + [markoffset,-markoffset];
```

```
113
114         path(1).coord(:,1) = thismarkpos + [-gridmarklength,0];
115         path(1).coord(:,2) = thismarkpos + [-gridmarklength2,0];
116         path(2).coord(:,1) = thismarkpos + [gridmarklength2,0];
117         path(2).coord(:,2) = thismarkpos + [gridmarklength,0];
118         path(3).coord(:,1) = thismarkpos + [0,-gridmarklength];
119         path(3).coord(:,2) = thismarkpos + [0,-gridmarklength2];
120         path(4).coord(:,1) = thismarkpos + [0,gridmarklength2];
121         path(4).coord(:,2) = thismarkpos + [0,gridmarklength];
122         writepath_1(1:4,path,gridmarkwidth,Mark_dose,layer..
123         ,cifflag,fid);
124         path(1).coord(:,1) = thismarkpos + [-gridmarklength2,0];
125         path(1).coord(:,2) = thismarkpos + [0,0];
126         path(2).coord(:,1) = thismarkpos + [0,0];
127         path(2).coord(:,2) = thismarkpos + [gridmarklength2,0];
128         path(3).coord(:,1) = thismarkpos + [0,-gridmarklength2];
129         path(3).coord(:,2) = thismarkpos + [0,0];
130         path(4).coord(:,1) = thismarkpos + [0,0];
131         path(4).coord(:,2) = thismarkpos + [0,gridmarklength2];
132         writepath_1(1:4,path,gridmarkwidth2,Mark_dose,layer..
133         ,cifflag,fid);
134
135         thismarkpos = thiscenter + [markoffset,markoffset];
136
137         path(1).coord(:,1) = thismarkpos + [-gridmarklength,0];
138         path(1).coord(:,2) = thismarkpos + [-gridmarklength2,0];
139         path(2).coord(:,1) = thismarkpos + [gridmarklength2,0];
140         path(2).coord(:,2) = thismarkpos + [gridmarklength,0];
141         path(3).coord(:,1) = thismarkpos + [0,-gridmarklength];
142         path(3).coord(:,2) = thismarkpos + [0,-gridmarklength2];
143         path(4).coord(:,1) = thismarkpos + [0,gridmarklength2];
144         path(4).coord(:,2) = thismarkpos + [0,gridmarklength];
145         writepath_1(1:4,path,gridmarkwidth,Mark_dose,layer,cifflag,fid);
146         path(1).coord(:,1) = thismarkpos + [-gridmarklength2,0];
147         path(1).coord(:,2) = thismarkpos + [0,0];
148         path(2).coord(:,1) = thismarkpos + [0,0];
149         path(2).coord(:,2) = thismarkpos + [gridmarklength2,0];
150         path(3).coord(:,1) = thismarkpos + [0,-gridmarklength2];
151         path(3).coord(:,2) = thismarkpos + [0,0];
152         path(4).coord(:,1) = thismarkpos + [0,0];
153         path(4).coord(:,2) = thismarkpos + [0,gridmarklength2];
154         writepath_1(1:4,path,gridmarkwidth2,Mark_dose,layer..
155         ,cifflag,fid);
156
157         thismarkpos = thiscenter + [-markoffset,markoffset];
158
```

```
159         path(1).coord(:,1) = thismarkpos + [-gridmarklength,0];
160         path(1).coord(:,2) = thismarkpos + [-gridmarklength2,0];
161         path(2).coord(:,1) = thismarkpos + [gridmarklength2,0];
162         path(2).coord(:,2) = thismarkpos + [gridmarklength,0];
163         path(3).coord(:,1) = thismarkpos + [0,-gridmarklength];
164         path(3).coord(:,2) = thismarkpos + [0,-gridmarklength2];
165         path(4).coord(:,1) = thismarkpos + [0,gridmarklength2];
166         path(4).coord(:,2) = thismarkpos + [0,gridmarklength];
167         writepath_1(1:4,path,gridmarkwidth,Mark_dose,layer..
168         ,cifflag,fid);
169         path(1).coord(:,1) = thismarkpos + [-gridmarklength2,0];
170         path(1).coord(:,2) = thismarkpos + [0,0];
171         path(2).coord(:,1) = thismarkpos + [0,0];
172         path(2).coord(:,2) = thismarkpos + [gridmarklength2,0];
173         path(3).coord(:,1) = thismarkpos + [0,-gridmarklength2];
174         path(3).coord(:,2) = thismarkpos + [0,0];
175         path(4).coord(:,1) = thismarkpos + [0,0];
176         path(4).coord(:,2) = thismarkpos + [0,gridmarklength2];
177         writepath_1(1:4,path,gridmarkwidth2,Mark_dose,layer..
178         ,cifflag,fid);
179     end
180 end
181
182 %%%%%%%%%%%%%%%%%%%%%%%%%%%%%%%%%%%%%%%%%%%%%%%%%%%%%%%%
183 %% generate zoneplate support pattern in layer 2
184
185 factor = lambda *g *b /(g+b) *1e6 * 1e6;
186
187 noofzones = ceil(zpradius^2 / factor);
188 if (mod(noofzones,2) == 0) noofzones = noofzones +1; end % ...
        noofzones should be odd integer
189
190 lastdose = 100.0;
191 %generate zoneplate zone data structure
192
193 % precompute zone parameters
194 pathsum =0;
195 for i = 1:2:noofzones
196
197         thiscenter = [0 0];
198
199         rmin = sqrt((i-1)*factor);
200         rmax = sqrt((i)*factor);
201
202         zonemin((i+1)/2) = rmin;
203         zonemax((i+1)/2) = rmax;
```

```
204         zoneradius((i+1)/2) = (rmax+rmin)/2;
205         zonewidth((i+1)/2) = (rmax-rmin);
206         zonecircum((i+1)/2) = 2*rmax*pi;
207 
208 end
209 
210 % real outer support radius
211 outersupportradius = zonemax((noofzones+1)/2);
212 
213 layer = 2;
214 % draw horizontal support bar
215 
216 
217          path2(1).coord(:,1) = centeroffield + [0 0];
218          path2(1).coord(:,2) = centeroffield + [outersupportradius 0];
219          path2(2).coord(:,1) = centeroffield + [0 0];
220          path2(2).coord(:,2) = centeroffield + [-outersupportradius 0];
221 
222 write_pixel_path_1(1:2,path2,supportbarwidth,100,layer,cifflag,fid,1);
223 
224 
225 %add write supports until condition is satisfied for all zones
226 for i = 1:1000
227 
228     i;
229     if (i==1)
230         innersupportradius = 0 ;
231 
232     else
233         noofslices = 2^i;
234         % compute support bar inner most ring
235 
236         %condition = (((zonecircum./noofslices)- supportbarwidth)
237         %./(zonewidth)) > 30;    % CONDITION WITH THE WIDTH. Got ...
               kind of the
238         %same pattern but cleary affects the distance between the ...
               outmost
239         %zones. "Innermost" radius for outermost bars are larger ...
               -> shorter
240         %support bars length.
241 
242         condition = ((zonecircum./noofslices) ./(zonewidth)) > 30;
243         indices = find(condition);
244         if(isempty(indices)) break; end
245         %if (i ==2) innersupportradius = 0 ;
246         innersupportradius = zonemin(indices(1));
```

```
247
248     end
249
250     noofbarstodraw = 2^(i+1);
251
252     for j = 1:2:noofbarstodraw-1
253
254         x1 = innersupportradius * cos(2*pi/noofbarstodraw*j);
255         y1 = innersupportradius * sin(2*pi/noofbarstodraw*j);
256         x2 = outersupportradius * cos(2*pi/noofbarstodraw*j);
257         y2 = outersupportradius * sin(2*pi/noofbarstodraw*j);
258
259         path1((j+1)/2).coord(:,1) = centeroffield + [x1 y1];
260         path1((j+1)/2).coord(:,2) = centeroffield + [x2 y2];
261
262     end
263     noofparpaths = write_pixel_path_1..
264     (1:noofbarstodraw/2,path1,supportbarwidth,100,..
265     layer,cifflag,fid,1);
266     %supportbarwidth = 0.400 ;  % TO REDUCE WIDTH (SHOULD BE AFTER ...
          NEXT LINE if wanted to iteratively reduce)
267           if (i==1)
268           layer = 3;
269           end
270 end
271 noofparpaths
272 fclose(fid);
```

A.2 Zone plate structure design

Main code:

```
1  clear;
2  %% writes support bar pattern into filename
3  % Use:
4  %- pixringasc_thr_quarter_1dose
5  %- writepath_1
6
7  layer = 0;
8  %%size of write field in microns (should be a multiple of 10)
9  writefield = 100.0; % IN MICRO M
10 % Set file type:
11 cifflag = 0;
12 if (cifflag)
```

```
13      extension = '.cif';
14  else
15      extension = '.asc';
16  end
17  g=0.935;  % KANTHEE: DISTANCE BETWEEN ZP and FOCAL POINT (in meter)
18  b=0.205;  % KANTHEE: DISTANCE BETWEEN SOURCE AND ZP
19
20
21  % KANTHEE: SET FILE NAME.
22  filename = ['1zp_nemiLN_d192_stop50_7Feb_1_full'];
23
24  % ZP CHARECTERISTIC VARIABLES?
25  %stopradius = 10;
26  stopradius = 25;
27
28  %lambda = 5.47e-11;  %RT
29  lambda = 9.78e-11;  %  %LN
30  zpradius = 96;
31  % Open the file, write mode:
32  fid=fopen([filename extension],'wt');
33
34  if (cifflag)
35      fprintf(fid,'L L1;\n');
36  end
37  %machine_step = ceil(writefield*1000 / 2^16) / 1000;
38  %machine_step = 0.004;   %Lastly
39  machine_step = 0.002;
40
41  %% write grid marks into layer 0
42  gridconstant = 1000.0;
43  gridmarklength = 29;
44  gridmarklength2 = 5;
45  gridmarkwidth = 3.0;
46  gridmarkwidth2 = 0.5;
47  griddose = 100.0;
48  gridsize = 1;
49  vertices = 1000;
50  rotation = 0;
51  bottomleft = [0 0];
52  markoffset = gridconstant/2 - gridmarklength;
53  layer = 1;
54  for i = 1:gridsize
55     for j = 1:gridsize
56         thiscenter = bottomleft + [(i-0.5)*gridconstant, ...
               (j-0.5)*gridconstant];
57
```

```
58          %layer = (i-1)*gridsize + j;
59
60          % (:,1) is x,y coords for long structures, (:,2) is for small.
61          thismarkpos = thiscenter + [-markoffset,-markoffset];
62          path(1).coord(:,1) = thismarkpos + [-gridmarklength,0];
63          path(1).coord(:,2) = thismarkpos + [-gridmarklength2,0];
64          path(2).coord(:,1) = thismarkpos + [gridmarklength2,0];
65          path(2).coord(:,2) = thismarkpos + [gridmarklength,0];
66          path(3).coord(:,1) = thismarkpos + [0,-gridmarklength];
67          path(3).coord(:,2) = thismarkpos + [0,-gridmarklength2];
68          path(4).coord(:,1) = thismarkpos + [0,gridmarklength2];
69          path(4).coord(:,2) = thismarkpos + [0,gridmarklength];
70          % USE FUNC writepath TO WRITE ASC-FILE.
71          writepath(1:4,path,gridmarkwidth,griddose,layer,cifflag,fid);
72          % Repeat for the end points. BASCIALLY point 2.
73          path(1).coord(:,1) = thismarkpos + [-gridmarklength2,0];
74          path(1).coord(:,2) = thismarkpos + [0,0];
75          path(2).coord(:,1) = thismarkpos + [0,0];
76          path(2).coord(:,2) = thismarkpos + [gridmarklength2,0];
77          path(3).coord(:,1) = thismarkpos + [0,-gridmarklength2];
78          path(3).coord(:,2) = thismarkpos + [0,0];
79          path(4).coord(:,1) = thismarkpos + [0,0];
80          path(4).coord(:,2) = thismarkpos + [0,gridmarklength2];
81          writepath(1:4,path,gridmarkwidth2,griddose,layer,cifflag,fid);
82
83
84          thismarkpos = thiscenter + [markoffset,-markoffset];
85          path(1).coord(:,1) = thismarkpos + [-gridmarklength,0];
86          path(1).coord(:,2) = thismarkpos + [-gridmarklength2,0];
87          path(2).coord(:,1) = thismarkpos + [gridmarklength2,0];
88          path(2).coord(:,2) = thismarkpos + [gridmarklength,0];
89          path(3).coord(:,1) = thismarkpos + [0,-gridmarklength];
90          path(3).coord(:,2) = thismarkpos + [0,-gridmarklength2];
91          path(4).coord(:,1) = thismarkpos + [0,gridmarklength2];
92          path(4).coord(:,2) = thismarkpos + [0,gridmarklength];
93          writepath(1:4,path,gridmarkwidth,griddose,layer,cifflag,fid);
94          path(1).coord(:,1) = thismarkpos + [-gridmarklength2,0];
95          path(1).coord(:,2) = thismarkpos + [0,0];
96          path(2).coord(:,1) = thismarkpos + [0,0];
97          path(2).coord(:,2) = thismarkpos + [gridmarklength2,0];
98          path(3).coord(:,1) = thismarkpos + [0,-gridmarklength2];
99          path(3).coord(:,2) = thismarkpos + [0,0];
100         path(4).coord(:,1) = thismarkpos + [0,0];
101         path(4).coord(:,2) = thismarkpos + [0,gridmarklength2];
102         writepath(1:4,path,gridmarkwidth2,griddose,layer,cifflag,fid);
103
```

```
104         thismarkpos = thiscenter + [markoffset,markoffset];
105         path(1).coord(:,1) = thismarkpos + [-gridmarklength,0];
106         path(1).coord(:,2) = thismarkpos + [-gridmarklength2,0];
107         path(2).coord(:,1) = thismarkpos + [gridmarklength2,0];
108         path(2).coord(:,2) = thismarkpos + [gridmarklength,0];
109         path(3).coord(:,1) = thismarkpos + [0,-gridmarklength];
110         path(3).coord(:,2) = thismarkpos + [0,-gridmarklength2];
111         path(4).coord(:,1) = thismarkpos + [0,gridmarklength2];
112         path(4).coord(:,2) = thismarkpos + [0,gridmarklength];
113         writepath(1:4,path,gridmarkwidth,griddose,layer,cifflag,fid);
114         path(1).coord(:,1) = thismarkpos + [-gridmarklength2,0];
115         path(1).coord(:,2) = thismarkpos + [0,0];
116         path(2).coord(:,1) = thismarkpos + [0,0];
117         path(2).coord(:,2) = thismarkpos + [gridmarklength2,0];
118         path(3).coord(:,1) = thismarkpos + [0,-gridmarklength2];
119         path(3).coord(:,2) = thismarkpos + [0,0];
120         path(4).coord(:,1) = thismarkpos + [0,0];
121         path(4).coord(:,2) = thismarkpos + [0,gridmarklength2];
122         writepath(1:4,path,gridmarkwidth2,griddose,layer,cifflag,fid);
123 
124         thismarkpos = thiscenter + [-markoffset,markoffset];
125         path(1).coord(:,1) = thismarkpos + [-gridmarklength,0];
126         path(1).coord(:,2) = thismarkpos + [-gridmarklength2,0];
127         path(2).coord(:,1) = thismarkpos + [gridmarklength2,0];
128         path(2).coord(:,2) = thismarkpos + [gridmarklength,0];
129         path(3).coord(:,1) = thismarkpos + [0,-gridmarklength];
130         path(3).coord(:,2) = thismarkpos + [0,-gridmarklength2];
131         path(4).coord(:,1) = thismarkpos + [0,gridmarklength2];
132         path(4).coord(:,2) = thismarkpos + [0,gridmarklength];
133         writepath(1:4,path,gridmarkwidth,griddose,layer,cifflag,fid);
134         path(1).coord(:,1) = thismarkpos + [-gridmarklength2,0];
135         path(1).coord(:,2) = thismarkpos + [0,0];
136         path(2).coord(:,1) = thismarkpos + [0,0];
137         path(2).coord(:,2) = thismarkpos + [gridmarklength2,0];
138         path(3).coord(:,1) = thismarkpos + [0,-gridmarklength2];
139         path(3).coord(:,2) = thismarkpos + [0,0];
140         path(4).coord(:,1) = thismarkpos + [0,0];
141         path(4).coord(:,2) = thismarkpos + [0,gridmarklength2];
142         writepath(1:4,path,gridmarkwidth2,griddose,layer,cifflag,fid);
143 
144 
145     end
146 end
147 
148 %% write 192*2?? micron diameter zoneplate with 20 micron central stop
149 
```

```
150 centeroffield = [500 500];
151 %centeroffield = [400.3 400.3];
152
153 %%% this is accurate to better than 1nm even for 1mm diameter ...
       zoneplate
154 factor = lambda *g *b /(g+b) *1e6 * 1e6;
155
156 firstzone = floor(stopradius^2 / factor);
157 noofzones = ceil(zpradius^2 / factor);
158
159 lastdose = 100.0;
160
161 layer = 2;
162 pathsum =0;
163
164 thiscenter = centeroffield;
165
166 dstitch = 0.01;
167
168 for i = firstzone:2:noofzones
169         % rmin and rmax for each zone:
170         rmin = sqrt((i)*factor);
171         rmax = sqrt((i+1)*factor);
172         dtheta = atan(dstitch / rmin);
173         % CALCULATE POINTS COORDINATE FOR EACH (i) ODD ZONE.
174         [arcwidth, ...
              number_paths,path,thisdose]=pixringasc_thr_quarter_1dose..
175         (rmin,rmax,thiscenter(1),thiscenter(2),machine_step,..
176         dtheta,2*pi /(pi/2 - 2*dtheta));
177         % WRITE ASC-FILE FOR EACH (i) ODD ZONE:
178         writepath(1:number_paths,path,0,thisdose,layer,cifflag,fid);
179         pathsum = pathsum + number_paths;
180         mywidth(i,:) = [ rmax-rmin, arcwidth, rmin, rmax, thisdose];
181 end
182 disp('first quarter done.');
183
184 for i = firstzone:2:noofzones
185
186         rmin = sqrt((i)*factor);
187         rmax = sqrt((i+1)*factor);
188
189         dtheta = atan(dstitch / rmin);
190         [arcwidth, ...
              number_paths,path,thisdose]=pixringasc_thr_quarter_1dose..
191         (rmin,rmax,thiscenter(1),thiscenter(2),machine_step,..
192         pi/2+dtheta,2*pi /(pi/2 - 2*dtheta));
```

```
193         writepath(1:number_paths,path,0,thisdose,layer,cifflag,fid);
194
195         pathsum = pathsum + number_paths;
196
197 end
198
199 disp('second quarter done.');
200
201 for i = firstzone:2:noofzones
202
203         rmin = sqrt((i)*factor);
204         rmax = sqrt((i+1)*factor);
205
206         dtheta = atan(dstitch / rmin);
207
208         [arcwidth, ...
               number_paths,path,thisdose]=pixringasc_thr_quarter_1dose..
209         (rmin,rmax,thiscenter(1),thiscenter(2),machine_step,..
210         pi+dtheta,2*pi /(pi/2 - 2*dtheta));
211         writepath(1:number_paths,path,0,thisdose,layer,cifflag,fid);
212
213         pathsum = pathsum + number_paths;
214
215 end
216 disp('third quarter done.');
217
218 for i = firstzone:2:noofzones
219
220         rmin = sqrt((i)*factor);
221         rmax = sqrt((i+1)*factor);
222
223         dtheta = atan(dstitch / rmin);
224
225         [arcwidth, ...
               number_paths,path,thisdose]=pixringasc_thr_quarter_1dose..
226         (rmin,rmax,thiscenter(1),thiscenter(2),machine_step,..
227         3*pi/2+dtheta,2*pi /(pi/2 - 2*dtheta));
228         writepath(1:number_paths,path,0,thisdose,layer,cifflag,fid);
229
230         pathsum = pathsum + number_paths;
231 end
232 disp('all done.');
233 pathsum
234 fclose(fid);
```

A.3 Additional functions

Function:write_pixel_path_1:

```
function success = write_pixel_path_1(range,path,width,dose,layer..
,cifflag,fid,adaptlayer)
r_step=0.012;
numberofparallelpaths = floor(width/r_step)+1;

if (cifflag)

    for ir = range
        for iwidth = 1:numberofparallelpaths

            %% calculate transformation of path coordinates
            %% only consider two point paths for now

            %{
            pt1 = path(ir).coord(:,1);
            pt2 = path(ir).coord(:,2);

            normalvector = [pt2(2)-pt1(2); pt2(1)-pt1(1)];
            normalunitvector = normalvector ./ ...
                sqrt(sum(normalvector.*normalvector));

            thiscoordarray(:,1) = pt1 - normalunitvector .* ...
                width./2 + (iwidth-1).*r_step.*normalunitvector;
            thiscoordarray(:,2) = pt2 - normalunitvector .* ...
                width./2 + (iwidth-1).*r_step.*normalunitvector;

            %}

            shortfactor = 0; %(abs((numberofparallelpaths / 2 - ...
                iwidth) / numberofparallelpaths)*2)^2;   % TIP OF ...
                THE BARS
                pt1 = path(ir).coord(:,1);
                pt2 = path(ir).coord(:,2);

            normalvector = [pt2(2)-pt1(2); -(pt2(1)-pt1(1))];
            pathvector = [ (pt2(1)-pt1(1));pt2(2)-pt1(2)];
            normalunitvector = normalvector ./ ...
                sqrt(sum(normalvector.*normalvector));
            pathunitvector = pathvector ./ ...
                sqrt(sum(pathvector.*pathvector));

```

```
35              if (mod(iwidth,2) == 1)
36                  thiscoordarray(:,1) = pt1 - normalunitvector .* ...
                        width./2 + ...
                        (iwidth-1).*r_step.*normalunitvector + ...
                        shortfactor*width/2 .* pathunitvector;
37                  thiscoordarray(:,2) = pt2 - normalunitvector .* ...
                        width./2 + ...
                        (iwidth-1).*r_step.*normalunitvector - ...
                        shortfactor*width/2 .* pathunitvector;
38              else
39                  thiscoordarray(:,2) = pt1 - normalunitvector .* ...
                        width./2 + ...
                        (iwidth-1).*r_step.*normalunitvector + ...
                        shortfactor*width/2 .* pathunitvector;
40                  thiscoordarray(:,1) = pt2 - normalunitvector .* ...
                        width./2 + ...
                        (iwidth-1).*r_step.*normalunitvector - ...
                        shortfactor*width/2 .* pathunitvector;
41              end
42
43
44              fprintf(fid,'W %d\n',1);
45              fprintf(fid,'%d %d\n',round(thiscoordarray .* 100));
46              fprintf(fid,';\n');
47
48          end
49
50      end
51
52  else
53
54      for ir = range
55
56          pt1 = path(ir).coord(:,1);
57          pt2 = path(ir).coord(:,2);
58
59          thislayer = layer;
60          if (adaptlayer)
61
62              patterncenter = 600.3;
63              if (pt1(1)-patterncenter > 0 && pt1(2)-patterncenter > 0)
64                  thislayer = layer + 2;
65              elseif (pt1(1)-patterncenter < 0 && ...
                    pt1(2)-patterncenter > 0)
66                  thislayer = layer + 3;
```

```
67              elseif (pt1(1)-patterncenter < 0 && ...
                   pt1(2)-patterncenter < 0)
68                  thislayer = layer;
69              elseif (pt1(1)-patterncenter > 0 && ...
                   pt1(2)-patterncenter < 0)
70                  thislayer = layer + 1;
71              end
72
73          end
74          for iwidth = 1:numberofparallelpaths
75
76              %% calculate transformation of path coordinates
77              %% only consider two point paths for now
78
79              shortfactor = 0;  % (abs((numberofparallelpaths / 2 - ...
                   iwidth) / numberofparallelpaths)*2)^2;
80              normalvector = [pt2(2)-pt1(2); -(pt2(1)-pt1(1))];
81              pathvector = [ (pt2(1)-pt1(1));pt2(2)-pt1(2)];
82              normalunitvector = normalvector ./ ...
                   sqrt(sum(normalvector.*normalvector));
83              pathunitvector = pathvector ./ ...
                   sqrt(sum(pathvector.*pathvector));
84
85              if (mod(iwidth,2) == 1)
86                  thiscoordarray(:,1) = pt1 - normalunitvector .* ...
                       width./2 + ...
                       (iwidth-1).*r_step.*normalunitvector + ...
                       shortfactor*width/2 .* pathunitvector;
87                  thiscoordarray(:,2) = pt2 - normalunitvector .* ...
                       width./2 + ...
                       (iwidth-1).*r_step.*normalunitvector - ...
                       shortfactor*width/2 .* pathunitvector;
88              else
89                  thiscoordarray(:,2) = pt1 - normalunitvector .* ...
                       width./2 + ...
                       (iwidth-1).*r_step.*normalunitvector + ...
                       shortfactor*width/2 .* pathunitvector;
90                  thiscoordarray(:,1) = pt2 - normalunitvector .* ...
                       width./2 + ...
                       (iwidth-1).*r_step.*normalunitvector - ...
                       shortfactor*width/2 .* pathunitvector;
91              end
92
93              fprintf(fid,'L %5.1f %d %5.3f\n',dose,thislayer,0);
94              fprintf(fid,'%7.3f %7.3f\n',thiscoordarray);
95              fprintf(fid,'#\n');
```

```
96          end
97
98      end
99
100 end
101
102 success = numberofparallelpaths;
```

Function:pixringasc_thr_quarter_1dose

```
1  function [arcwidth,num_total_arcs, ...
       path,dose]=pixringasc_thr_quarter_1dose(rmin,rmax,xcenter,ycenter..
2  ,machine_step,theta_start,circfrac)
3  % [number_paths, paths]=pixringasc(rmin,rmax,xcenter,ycenter)
4  % ------------------------------------------------------------------
5  % Generates paths representing a ring fromed by concentric single
6  % pixel lines.
7  % - rmin is the inner radius
8  % - rmax is the outer radius
9  % - xcenter and ycenter are the center of ring
10 % - circfrac
11 % - theta_start
12 % - machine_step
13 %
14 % The function returns an array of points (x,y) describing the
15 % paths .
16 %
17 % - number_paths is the number of single pixel line used
18 % - paths(path_number,1 for x and 2 for y, coordinate number HERE!!)
19 %
20 % The output units are the same as the input units.
21 % However, the stepsize between the single pixel lines is assumed to
22 % be 12 nm and is expressed in the file as 0.012. (r_step in code)
23 %
24 % Moreover, a 6nm global stepsize is already taken into account
25 % to minimize surprises after exposure. (machine_step in code)
26 %
27 % MICRONS should hence be used as input and output parameters
28 % ------------------------------------------------------------------
29 % Saving into an .asc file can be done with the following code
30 %
31 % [number_paths,path]=pixringasc(rmin,rmax,xcenter,ycenter);
32 % for ir=1:number_paths
33 %     fprintf(fid,'L 100 %d 0\n',layer);
34 %     fprintf(fid,'%7.4f %7.4f\n',path(ir).coord);
```

```
35 %     fprintf(fid,'#\n');
36 % end
37 % ------------------------------------------------------------------
38 % November 2003
39 % Tymon Barwicz, NSL, MIT
40
41 % write circles of uniform points per unit length
42 % dividing each circle into arcs as required
43 %
44
45 % 1000 points per arc single pixel line (as default)
46 numpoints_default=1000;
47
48 % the stepsize in r is 12 nm
49 % vary how far paths are written apart in the radial direction
50 %r_step=0.010;
51 % the machine step size is
52 % machine_step=0.002; now an input
53
54 %{
55 % the number of required circles is
56 w=rmax-rmin;
57 % assume linewidth that single path will create
58 linewidth = 0.0096;
59
60 number_paths=floor(w/linewidth);
61
62 r_step = w/number_paths;
63
64 dose = r_step / linewidth * 100;
65
66 %r_step = 0.0096;
67 arcwidth = number_paths;
68
69 %}
70
71 r_step = 0.012;
72 %r_step = 0.010;     %(CHOOSE TO BE 3x bigger than Machine step)
73 %r_step = 0.0096
74 % the number of required circles is
75 w=rmax-rmin;
76
77 number_paths=floor(w/r_step)-1;
78 %r_step = round(w/number_paths *1000)/1000
79 arcwidth = number_paths;
80 %doseaddition = (w/r_step - (number_paths + 1)) * 75.0;
```

```
doseaddition = (w/r_step - (number_paths + 1)) * 10.0;
dose = 100.0 + doseaddition;
%dose = 100.0;
% maximal distance between points such that deviation from arc is less
% than half the focuswidth(r_step)
point_distance = sqrt(4*rmin*machine_step-machine_step^2);
%circfrac = 1;
num_points_per_circle = 2*rmax*pi/circfrac / point_distance;
num_arcs = ceil(2*rmax*pi/circfrac/ point_distance ...
    /numpoints_default);
num_points_per_arc = ceil(num_points_per_circle / num_arcs);

num_total_arcs = num_arcs * (number_paths);

% Try to reduce the pixelization error by choosing the middle ring
% radius within a 6 nm global stepsize and counting single pixel ...
    lines from
% there with 12 nm steps in "r".
% WARNING: there might be an additional pixelization error if ...
    r_step is not
% a multiple of machine_step
rmid=round((rmax+rmin)/2/machine_step)*machine_step;

% Start by writing the inner egde and go to the outer edge
% dont write innermost and outermost circle
%theta_start= 0;
for ir=1:number_paths
    r=rmid-(r_step*(number_paths-1)/2)+r_step*(ir-1);
    % less than 1000 points if small circle
    % (steps smaller than machine_step are useless)
    %circonference_points=round(r*2*pi/machine_step);
    %numpoints=min([numpoints_default,circonference_points]);

    % may want to improve on theta_start distribution later
     %(ir-1)*(2*pi/4/num_arcs/number_paths);
    for iarc = 1:num_arcs
        if (iarc >1) disp('Error. unexpected number of arcs'); end

        if (mod(ir,2)==0)
            theta_arc_start = theta_start;  %Theta start is input.
            circdirection = 1;
        else
            theta_arc_start = theta_start + 2*pi / circfrac;
            circdirection = -1;
        end
        for it=1:num_points_per_arc
```

```
124             theta= theta_arc_start + circdirection * ...
                    2*pi/circfrac/num_arcs*(it-1)/(num_points_per_arc-1);
125             %path(1,2,3,.....nr_path?)
126             path((ir-1)*num_arcs+iarc).coord(1,it)=round((xcenter ...
                    + r*cos(theta))./machine_step).*machine_step; %x ...
                    coordinate
127             path((ir-1)*num_arcs+iarc).coord(2,it)=round((ycenter ...
                    + r*sin(theta))./machine_step).*machine_step; %y ...
                    coordinate
128         end
129
130     end
131
132 end
```

writepath_1

```
1  function success = ...
       writepath_1(range,path,width,dose,layer,cifflag,fid)
2
3  if (cifflag)
4
5      for ir = range
6          fprintf(fid,'W %d\n',width*100);
7          fprintf(fid,'%d %d\n',round(path(ir).coord .* 100));
8          fprintf(fid,';\n');
9      end
10 else
11
12     for ir = range
13         fprintf(fid,'L %5.1f %d %5.3f\n',dose,layer,width);
14         fprintf(fid,'%7.3f %7.3f\n',path(ir).coord);
15         fprintf(fid,'#\n');
16     end
17 end
18 success = 1;
```